HWR No. 93-030

THE ESTIMATION AND SCALING OF LAND-SURFACE FLUXES OF LATENT AND SENSIBLE-HEAT WITH REMOTELY SENSED DATA OVER A GRASSLAND SITE

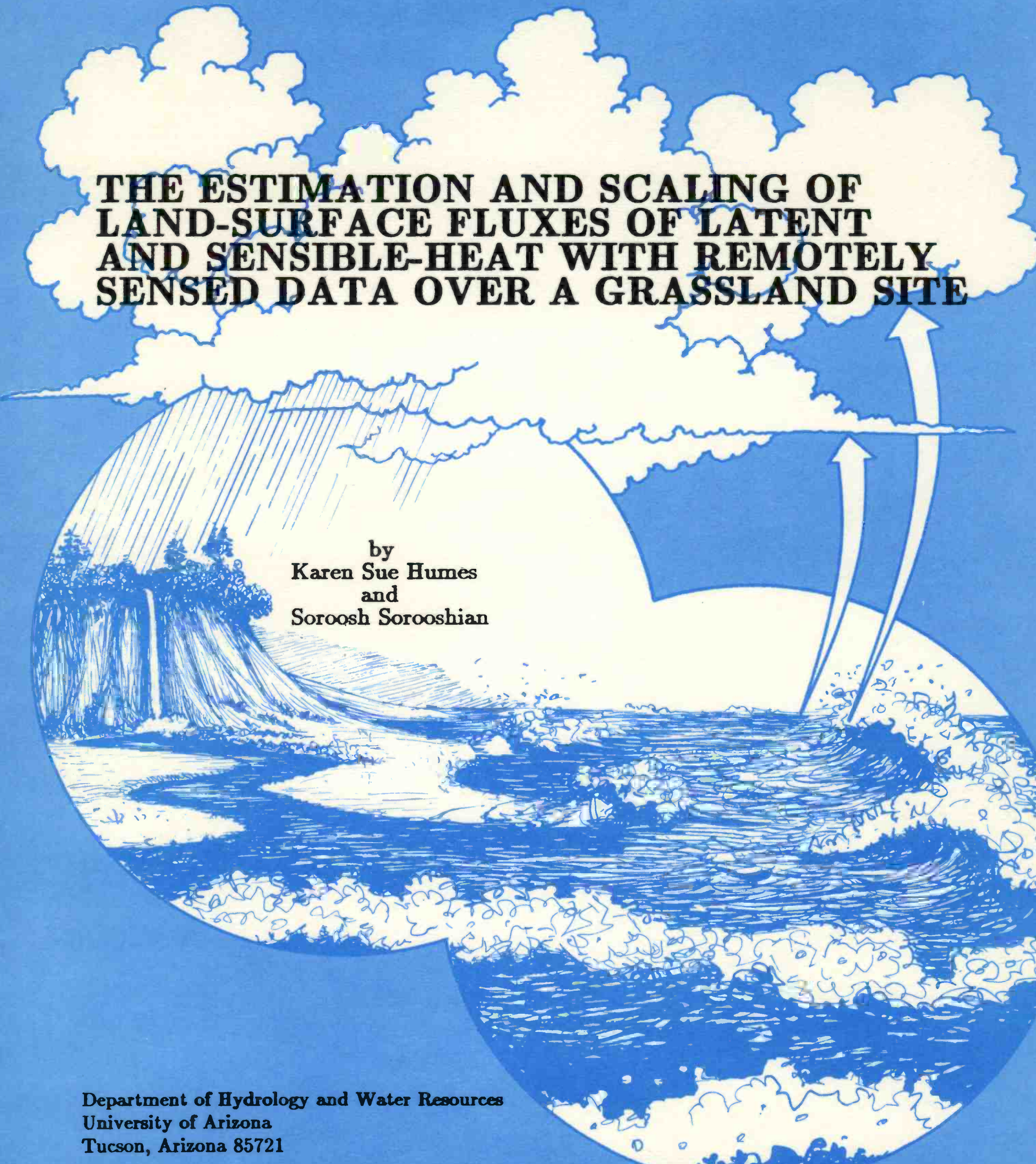

by
Karen Sue Humes
and
Soroosh Sorooshian

Department of Hydrology and Water Resources
University of Arizona
Tucson, Arizona 85721

HWR No. 93-030

THE ESTIMATION AND SCALING OF LAND-SURFACE FLUXES OF LATENT AND SENSIBLE-HEAT WITH REMOTELY SENSED DATA OVER A GRASSLAND SITE

by
Karen Sue Humes
and
Soroosh Sorooshian

Department of Hydrology and Water Resources
University of Arizona
Tucson, Arizona 85721

PREFACE

This report is part of an ongoing series of publications issued by the Department of Hydrology and Water Resources of The University of Arizona, located in Tucson. The purpose of this series is to disseminate detailed research findings to a broad audience of persons interested in natural resources.

The content of this report is based on the dissertation by Humes (1992). Brief quotations from this report are allowed without special permission, provided that accurate acknowledgment of source is made. Requests for permission for extended quotation from or reproduction of this manuscript in whole or in part may be granted by the author.

STATEMENT BY AUTHOR

This dissertation has been submitted in partial fulfillment of requirements for an advanced degree at The University of Arizona and is deposited in the University Library to be made available to borrowers under rules of the Library.

Brief quotations from this dissertation are allowable without special permission, provided that accurate acknowledgment of source is made. Requests for permission for extended quotation from or reproduction of this manuscript in whole or in part may be granted by the head of the major department or the Dean of the Graduate College when in his or her judgment the proposed use of the material is in the interests of scholarship. In all other instances, however, permission must be obtained from the author.

SIGNED: Karen Sue Humes

ACKNOWLEDGEMENTS

I am indebted to my committee members for the encouragement and support they have provided me in the course of my graduate studies. In particular, very special thanks are due to my major advisor, Soroosh Sorooshian, who has provided me with unwavering support, much good advice, and many special opportunities throughout my graduate studies. I am also particularly grateful to Ray Jackson. Ray has been known to be a source of wise counsel to many on a wide variety of subjects, but the single most important advice he has given me in the many years I have known him was imparted to me during our first conversation. In planning my graduate studies, he cautioned me to strive to be first and foremost a disciplinary scientist (or interdisciplinary, as the problem may warrant) and to acquire knowledge in remote sensing techniques as a tool to use in serving that discipline. It is advice that I hope to follow for a long time to come. Alfredo Huete has served on both my M.S. and Ph.D. committees and has always been a source of insightful perspectives on key issues in remote sensing. I am also grateful to Dave Woolhiser and Mike Sully, who have expanded my knowledge of some very important principles of surface water hydrology and soil physics, respectively.

It would not have been possible for me to pursue this area of research without a fellowship from the NASA Graduate Student Research Program and a grant from the NASA Earth Observing System Program (NAG2425). I am particularly indebted to Robert Gurney for his encouragement and technical guidance during my early years in the GSRP program. I owe Ghassem Asrar very special thanks for both his role at NASA Headquarters and his role in the implementation of the FIFE experiment. I am also very grateful for the support provided by the John and Margaret Harshbarger Fellowship.

I am also deeply indebted to the many people who played key roles in the planning and implementation of the FIFE experiment, notably Forrest Hall, Piers Sellers, and Bob Murphy. My experiences in other field experiments provide me with a deep sense of gratitude to those many, many people who labored for hours to plan, acquire, and analyze the many different data types used in this dissertation. It would not have been possible to utilize data acquired at the FIFE experiment without the superb guidance and support of the staff of the FIFE Information System, led by Don Strebel. In addition to providing superb technical products and support, Don and the FIS staff, notably Diana van Elberg-Obler, Fred Heummerich, Scott Goetz, and Jeff Newcomer, provided a welcome environment for me during many visits to GSFC.

In my time at The University of Arizona, I have been influenced by many of my fellow students and cooperating investigators. In particular, I would like to thank Dave Goodrich, Jené Michaud, Jim Washburne, Susan Moran, Ghani Chehbouni, and Jiaguo Qi for many interesting and stimulating discussions over the years. I would also like to thank Corrie Thies for the assistance she provided in the final preparation of this dissertation, through both her friendship and her professional skills. Lastly, this dissertation is dedicated to my mother, Viola Humes, whose shining example and lifelong love and support have always been my life's most precious gift.

TABLE OF CONTENTS

Page

Page

Page

LIST OF ILLUSTRATIONS

Figure | Page

LIST OF TABLES

ABSTRACT

The overall topic of the research described in this dissertation was the partitioning of available energy at the Earth's surface into sensible and latent heat flux, with an emphasis on the development of techniques which utilize remotely sensed data. One of the major objectives was to investigate the modification of existing techniques, developed over agricultural surfaces, to "natural" ecosystems (i.e., non-agricultural vegetation types with variable and incomplete canopy cover).

Ground-based measurements of surface fluxes, vegetation cover, and surface and root-zone soil moisture from the First ISLSCP (International Land Surface Climatology Program) Field Experiment (FIFE) were used to examine the factors controlling the partitioning of energy at ground stations with contrasting surface characteristics.

Utilizing helicopter-based and satellite-based data acquired directly over ground-based flux stations at the FIFE experimental area, relatively simple algorithms were developed for estimating the soil heat flux and sensible heat flux from remotely sensed data. The root mean square error (RMSE) between the sensible heat flux computed with the remotely sensed data and the sensible heat flux measured at the ground stations was 33 Wm^{-2}. These algorithms were then applied on a pixel-by-pixel basis to data from a Landsat-TM (Thematic Mapper) scene acquired over the FIFE site on August 15, 1987 to produce spatially distributed surface energy-balance components for the FIFE site.

A methodology for quantifying the effect of spatial scaling on parameters derived from remotely sensed data was presented. As an example of the utility of

this approach, NDVI values for the FIFE experimental area were computed with input data of variable spatial resolution. The differences in the values of NDVI computed at different spatial resolutions were accurately predicted by an equation which quantified those differences in terms of variability in input observations.

CHAPTER 1

INTRODUCTION

Significance of Land Surface Fluxes of Moisture and Energy

In his Presidential address to the Royal Meteorological Society in 1979, J.L. Monteith closed with these remarks:

> " The evaporation of water and associated diffusion of water vapour and heat are processes of profound terrestrial importance . . . . in all these systems (climatological, hydrological, ecological, domestic, and industrial) one of the central thermodynamic problems is the partitioning of available energy between sensible and latent heat. In the last analysis, partitioning depends on the ratio of Δ to γ which is determined by the physical properties of water as liquid and as vapour. I believe that the nature and distribution of life on our planet depends just as much on the value of Δ/γ as on the magnitude of the Solar Constant and other prestigious parameters of geophysics. The study of natural evaporation is indeed one of the most necessary Ingredients of a real and Philosophical Meteorology."

In the years that have passed since Dr. Monteith's address, his view of the importance of this topic has been gradually understood and embraced by a broad scientific community that includes, but is not limited to, meteorologists. One of the most sweeping international initiatives to influence the Earth and atmospheric sciences over the last decade is the attempt to better understand the Earth as an integrated system. The cycling of water and energy is a key component of that integrated system on local, regional, and global scales.

The Critical Link Between Water and Energy Cycles

Despite the eloquent plea of Penman (1963), the combined processes of evaporation from land surfaces and transpiration from vegetation are commonly referred to with the rather awkward term "evapotranspiration" (ET). This author will yield to convention and hereafter will refer to the combined effect of the two processes with that term. Years of common usage of the term, however, have made Penman's initial objections even more valid; the reader is cautioned to keep in mind that the term evapotranspiration is simply a short-hand expression for two separate processes and not a process in itself.

The study of the combined effect of these two processes is particularly important because they form the critical link between the Earth's energy balance and water balance. The latent heat flux term in the energy balance equation is equivalent to the amount of energy required to evaporate the volume of water represented in the evapotranspiration term of the water balance. Therefore, a better understanding of the partitioning of available energy at the land surface into latent and sensible heat flux, and methods to quantify those fluxes, will lead to a better understanding of the coupling of these two fundamental terrestrial cycles. Further, it will also lead to a better understanding of the water balance and methods for quantifying one of its key components.

On the average, evaporation and transpiration from land surfaces account for approximately 60% of precipitation (Brutsaert, 1986). The practical benefits of better quantifying such a major component of the water balance have enormous societal impacts. These practical impacts include improvement in fundamental hydrologic and water resource applications, such as flood forecasting and the planning and management of water supply for agricultural, industrial, and domestic use.

Interactions Between Land-Surface Hydrology, the Atmosphere, and Climate

Globally, evaporation from the world's oceans supplies three times more water vapor, and thus much more latent heat flux, to the atmosphere than does the land surface (Eagleson, 1982). Nevertheless, the storages of near-surface and root zone soil moisture, and the fluxes of moisture and energy from the land surface to the atmosphere, are critically important for a number of reasons. The land surface supports agricultural activities which provide the world's food source. It is important, therefore, that we be able to better understand and quantify the response of land surface moisture storages and fluxes to potential changes in climatic forcing, as well as the feedback mechanisms by which those land-surface responses amplify or dampen the changes in climatic forcing.

The land surface also supports ecosystems of critical importance to the cycling of carbon and other nutrients. The processes involved in the biogeochemical cycling by these ecosystems can be moisture and/or energy-limited. The interaction between these biogeochemical cycles and the water and energy cycles is not well understood.

For some regions, such as the Amazon Basin, the recycling of moisture from the land surface is the major source of contributing to regional precipitation (Lettau et al., 1979; Salati and Vose; 1984; Shuttleworth, 1988b). For most regions, however, the dominant source of atmospheric water vapor is evaporation from ocean surfaces. Even in those cases, the land-surface energy fluxes act in combination with orographic effects to strongly influence where the latent energy will be released, as the water vapor condenses into precipitation (Eagleson, 1986).

Numerical experiments with general circulation models and with regional climatology models have shown that changes in surface vegetation, soil moisture, and albedo (and thus surface fluxes of moisture and energy) influence the magnitude and distribution of atmospheric parameters that control global and regional climate (Charney et al., 1977; Lettau et al., 1979; Shukla and Mintz, 1982; Rowntree and Bolton, 1983; Mintz, 1984; Henderson-Sellers and Gornitz, 1985; Laval, 1986; Nicholson, 1988). How these changes in land surface and climate conditions interact, including the effects of feedback mechanisms, is not well understood at any scale (local, regional, or global). One of the primary reasons that these interactions and feedbacks are not well understood is that it is difficult to quantify the land-surface fluxes of moisture and energy at local, regional, and global scales.

Most techniques for measuring or estimating the latent heat flux component of the energy balance utilize point-based instrumentation. These techniques are limited in areal extent to the area over which these point-based data are valid. There are a number of expressions which attempt to describe regional-scale evaporation (discussed in more detail below), but it is difficult to validate both the assumptions and the estimates provided by these expressions. If remote sensing techniques can be developed which accurately estimate the components of the surface energy balance for a variety of surface conditions, then spatially distributed values of surface fluxes could be derived from aircraft and satellite-based remotely sensed data. These spatially distributed flux estimates would be a fundamentally new tool to explore and quantify land-surface atmosphere interactions.

Spatial Scaling and the Integrating Effects of the Atmosphere

There are at least two separate spatial scaling issues which must be addressed in the study of land-surface fluxes of moisture and energy. The first issue relates to the procedures used to estimate surface fluxes using areal estimates of surface parameters. Such parameters are estimated from remotely sensed data and are areal-integrated averages of parameters that are actually spatially variable. Because the surface parameters are related to surface fluxes in a non-linear manner, the spatially integrated parameter values may not be related to the spatially integrated fluxes in the same way that point-based parameters and fluxes are related, especially as the scale of the areal integration increases.

The second scaling issue relates to how spatially variable fluxes are integrated in the atmospheric boundary layer (ABL). Spatially variable fluxes of moisture and energy near the land surface are mixed within the ABL and influence the properties of the regional ABL. These properties in turn control the regional atmospheric forcing exerted on the surface. In considering the question of catchment scale evaporation, Brutsaert (1986) pointed out that the atmosphere has the capacity of integrating and smoothing the effects of small-scale irregularities over larger areas. He stated that the improved parameterization of evapotranspiration at the regional and watershed scale will require a better understanding of the turbulent transport mechanisms in the atmospheric boundary layer.

One approach by which this can be achieved is modeling the dynamics of atmospheric boundary layer processes, validated with data from field experiments. The data required to develop and test these models include spatially distributed surface flux estimates. Spatially distributed flux estimates can be used as lower boundary conditions and the necessary measurements of the characteristics of the developing ABL.

These two different issues in spatial scaling of surface fluxes are not independent of each other. An understanding of the effects of spatial scaling in estimating surface fluxes from remotely sensed data is required in order to provide the surface boundary conditions for the modeling studies. The modeling studies will, in turn, provide information regarding the spatial scales at which those boundary conditions are required and the spatial scale of the atmospheric forcings which influence the surface fluxes.

In order to eventually understand land-surface/atmosphere interactions, the scaling of surface fluxes must be understood in the context of coupled surface/atmospheric boundary layer models. However, we must first understand the derivation of the spatially distributed surface flux estimates which will be used as input data for those coupled models. The research described in this dissertation will explore some of the spatial scaling issues related to the procedures used to estimate surface fluxes using areal estimates of surface parameters. The issue of how surface heterogeneities interact with the ABL is an important topic for ongoing and future research.

Existing Methods for Estimating Evapotranspiration

Expressions to Estimate Evapotranspiration from Meteorologic Data

An extensive treatment of this subject is given in the texts by Monteith (1973) and Brutsaert (1982). A few examples are provided here of equations which embody important concepts and have been widely used. The relationship between several of these expressions will be explored further in Chapter 2. The terms used in the equations presented in this chapter are defined in Table 1.1.

The concept of potential evapotranspiration introduced by Thornthwaite (1948) refers to the rate of evaporation from a large area covered completely and uniformly by actively growing vegetation which is well supplied with moisture (i.e., soil moisture does not limit the evaporation process). One of the expressions most widely used to estimate potential evapotranspiration was given by Penman (1948) as:

$$LE = \left(\frac{\Delta}{\Delta + \gamma}\right) R_{net} + \left(\frac{\gamma}{\Delta + \gamma}\right) E_a, \tag{1.1}$$

where L is latent heat of vaporization of water, in Jkg^{-1}; E is the rate of evaporation in $kgs^{-1}m^{-2}$; R_{net} is the net radiation in Wm^{-2}; Δ is the slope of the saturation vapor pressure versus temperature curve, $mbar^{o}C^{-1}$ (Celsius), evaluated at air temperature; γ is the psychrometric constant, in $mbar^{o}C^{-1}$; and E_a is a function of windspeed and

Table 1.1. List of Notations Used in Chapter 1

R_{net} = Net radiation	Wm^{-2}
G = Soil heat flux	Wm^{-2}
H = Sensible heat flux	Wm^{-2}
LE = Latent heat flux	Wm^{-2}
Q_n = Total energy flux available to be used for evaporation	Wm^{-2}
E = Rate of evaporation	$kgs^{-1}m^{-2}$
L = Latent heat of vaporization of water	$J\ kg^{-1}$
ρ = Density of air	$kg\ m^{-3}$
C_p = Heat capacity of air	$J \times kg^{-1}\ C^{-1}$
γ = Psychrometric constant, C_p/L	mbar C^{-1}
T_s = Surface temperature	°C
T_a = Air temperature at reference height	°C
e_s^* = Saturated vapor pressure at T_s	mbar
e_a^* = Saturated vapor pressure at T_a	mbar
e_a = Vapor pressure at reference height	mbar
r_a = Aerodynamic resistance for transport of heat and water vapor from surface to reference height	sm^{-1}
r_s = Surface resistance to evaporation	sm^{-1}
Δ = Slope of saturated vapor pressure vs. temperature curve, evaluated at some temperature	mbar C^{-1}

vapor pressure deficit at some reference point above the surface. There are several different functional forms used to estimate the E_a term, the most common being the product of vapor pressure deficit and a linear function of windspeed (Penman, 1948; Thom and Oliver, 1977). The first term of Equation (1.1) was thought of as the radiant energy contribution to evaporation, and the second term was conceptualized as the "drying power" of the air. The Penman equation has been the subject of many experimental and theoretical studies and has been widely used by engineers. Because it requires point-based data relating to net radiation, temperature, windspeed, and vapor pressure deficit, it is generally applicable only to the local areas over which measurements of those parameters are be valid. A common misapplication of the Penman equation is to calculate "potential" evapotranspiration using meteorological data collected over an area that is not evapotranspiring at the "potential" rate. When actual evaporation falls below the potential rate, the meteorological parameters required for the computation of "potential" evaporation are affected. Thus, it is not reasonable to use meteorological data acquired over nonpotential conditions to calculate the potential evapotranspiration rate. Because it was derived from a combination of bulk mass transfer and energy budget considerations, the Penman formulation and modifications of it have come to be known as the "combination approach".

Slatyer and McIlroy (1961) used the two-term structure of the Penman equation as a basis for interpreting the effects of regional or large-scale advection in regional evaporation. They suggested that, for a large homogeneous and thoroughly wetted area, the vapor pressure deficit near the surface would approach zero. Therefore, they considered the first term in Equation (1.1) to represent the lower limit of evaporation from a moist surface and referred to it as equilibrium evaporation, given by the equation:

$$LE_{eq} = \left(\frac{\Delta}{\Delta + \gamma}\right)(R_{net} - G) \tag{1.2}$$

in which the soil heat flux, G, Wm^{-2}, is included to describe the amount of energy available for evaporation.

However, larger scale perturbations in the atmosphere appear to prevent the establishment of steady, equilibrium conditions near the surface. Vapor pressure deficits are usually maintained over both land and ocean surfaces; hence, equilibrium evaporation is rarely observed in nature. With this in mind, Priestley and Taylor (1972) extended the concept of equilibrium evaporation by adding the empirical factor α to the expression for evaporation, giving the latent heat flux as:

$$LE = \alpha\left(\frac{\Delta}{\Delta + \gamma}\right)(R_{net} - G). \tag{1.3}$$

They evaluated data sets for a variety of surfaces (open water, bare soil, grass) and recommended a value of $\alpha = 1.26$ for average daily evaporation over a variety of surfaces. Many studies have been carried out to evaluate the empirical α factor and are described in more detail in Chapter 2.

Bouchet (1963) introduced the concept of a complementary relationship between actual and potential evaporation. Using heuristic arguments, he reasoned that, when the actual evapotranspiration (E_{act}) fell below potential evapotranspiration (E_p), there is an impact on the temperature, humidity, and turbulence of the air near the ground which further increases the evaporative demand. He defined E_p to be the evapotranspiration which would take place if only the available energy were the limiting factor. When $E_{act} = E_p$, he denoted it as E_{po} and obtained the expression:

$$E_p + E_{Act} = 2E_{po}. \tag{1.4}$$

Although no sound theoretical basis has been advanced for this concept (Monteith, 1981), it has been supported by experimental data (Morton, 1970; Fortin and Seguin, 1975; Kovacs, 1989).

Brutsaert and Stricker (1979) evaluated the complementary relationship described in Equation (1.4) using the Penman expression for E_p and the Priestley-Taylor expression for E_{po}. They obtained the expression known as the advection-aridity equation for actual regional evapotranspiration, given by:

$$LE = (2\alpha - 1)\frac{\Delta}{\Delta + \gamma}(R_{net} - G). \tag{1.5}$$

The exact form of the equation depends on the choice of the E_a function, and the α parameter must be assumed or empirically determined.

Another widely used expression for actual and potential evapotranspiration is the Monteith modification to the original Penman equation, generally known as the Penman-Monteith equation (Monteith, 1973; Thom and Oliver, 1977), or the resistance form of the combination equation, given by:

$$LE = \frac{\Delta (R_{net} - G) + \rho C_p (e_a^* - e_a)/r_a (R_{net} - G)}{\Delta + \gamma (1 + r_s/r_a)}, \tag{1.6}$$

where ρC_p, in $Jm^{-3}C^{-1}$, is the volumetric heat capacity; e_a^*, in mbars, is the saturated vapor pressure at the air temperature; e_a, mbar, is the actual vapor pressure of the air at a reference height above the surface; r_a is the aerodynamic resistance to the transfer of both heat and vapor (i.e., they are assumed to be the same), in ms^{-1}; and r_s is the surface resistance to the transfer of water vapor from the leaf surface to the canopy airspace, in ms^{-1}. Like the original Penman equation, this expression is derived from a combination of the energy-balance equation and the bulk transfer equations for heat and moisture transfer, but the equation is cast in terms of resistance parameters. The expression can be used to estimate potential evaporation by setting the value of r_s equal to the surface resistance to water vapor transfer when the vegetation surface is well-supplied with moisture. For most vegetation types, the value of r_s under "potential" conditions in nonzero. The only case for which $r_s = 0$ is the case of an open water surface and the case of free water on the vegetation surfaces due to interception or condensation. As the availability of soil moisture in the root zone of the vegetation becomes limiting, the r_s parameter increases, controlled by the physiological characteristics of the vegetation and its response to limited moisture supply.

The resistance approach was extended by Shuttleworth and Wallace (1985) to surfaces with sparse canopy cover, in which both the vegetation and the soil substrate interacted with the canopy airspace. Using the resistance analogy, they developed bulk transfer expressions utilizing aerodynamic and surface resistances to heat and vapor transfer between the soil and inter-canopy airspace, between the vegetation and the inter-canopy airspace, and between the intercanopy airspace and a reference level above the canopy. An expression that included the contributions of soil and vegetation to total latent heat flux was developed in terms of these resistances.

Soil/Plant/Atmosphere Simulation Models

A number of models have been developed which simulate the exchange of heat and moisture between the lower atmosphere, vegetation, and soil layers, ranging from very complex (Camillo et al., 1983; Sellers et al., 1986; van de Griend and van Boxel, 1989) to moderately complex (Deardorff, 1978; Taconet et al., 1986; Dickinson et al., 1986; Choudhury and Monteith, 1988). These models vary in the degree of detail and number of parameters with which the processes are described. Some of these models were developed with the intention of utilizing remotely sensed data for input; all of them implicitly estimate surface fluxes of heat and moisture in the process of numerically solving the series of equations describing the transfers of heat and moisture in the soil/plant/atmosphere system. Some of these models were designed to be used as tools to study local-scale exchanges of heat and moisture and the parameters that control them. Some were developed as improved land-surface parameterizations for general circulation models (GCMs). The current need for large-scale land-surface hydrologic components for GCMs has stimulated modification and simplification to some of these models and a proliferation of similar models.

One of the good features of most of the models mentioned above (particularly the more complex ones) is that they describe the processes which occur at a local scale in a physically realistic manner. In order to accomplish this, however, the models require apriori knowledge of, or must solve for, a large number of local-scale parameters. Many of these parameters, particularly soil and vegetation properties, have significant spatial variability over length scales of tens of meters and even greater variability over length scales of several kilometers. Some of the parameters have little physical meaning at length scales of hundreds of kilometers. While these models can be very effective tools to further our understanding of how the parameters and their interactions influence the surface fluxes of moisture and energy, their application would seem to be limited to the spatial scales for which the controlling parameters could be expected to be valid.

One of the objectives of the research described in this dissertation is to investigate how spatially integrated surface fluxes can be estimated as directly as possible from remotely sensed data, using a minimum number of parameters which can be observed at spatial scale of the desired flux estimate. An application of this research may be the production of spatially distributed flux estimates which could be used to validate or update models such as those described above.

Direct Measurements of Evapotranspiration

The most elementary technique to measure potential evaporation is the evaporation pan, from which the depth of water evaporated from an open water surface in a cylindrical pan is directly observed. Due to the limitations on pan size and spurious edge effects, the evaporation rate from a pan is usually 5-30% larger than that from a small lake or pond (Arya, 1988). In addition, the aerodynamic and surface resistances to evaporation for a soil and vegetation surfaces are not the same as that for open water, which provides another mechanism for error in the estimation of potential evaporation by the pan technique.

A direct method for measuring the amount of actual evaporation and transpiration from relatively small field plots is to use a weighing lysimeter (van Bavel, 1961). With this technique, changes in mass of an isolated volume of soil and vegetation are monitored. This is a very accurate technique, but it is limited to relatively small spatial scales. In addition, the isolation of the root zone from the surrounding soil can disturb some of the natural horizontal and vertical gradients in moisture and temperature which may affect the moisture transport in the soil.

Two micrometeorological methods commonly used for the measurement of sensible and latent heat flux are the Bowen ratio and eddy correlation techniques. Both techniques are believed to estimate latent and sensible heat flux fairly accurately (10-15%, under most conditions) for areas having level, homogeneous upwind fetches. Some sources of uncertainty for both techniques are described below. The fluxes measured with both of these techniques are limited in that they represent the fluxes over a relatively small upwind fetch area. The exact size of the fetch area for the two techniques varies according to instrument height, local topography, and windspeed. With instruments located about 2 meters above the surface, the typical length scale of the fetch area is approximately 30-80 meters (Brutsaert, 1982). The location of the fetch area depends on the prevailing wind direction.

The Bowen ratio technique relies on the development by Bowen (1926) that allows the partitioning of available energy between sensible and latent heat flux to be estimated from gradients of temperature and humidity. This technique involves measuring the near-surface vertical gradient of temperature and vapor pressure. For bare soil and short crops, for which the technique works best, this is usually accomplished by measuring air temperature and vapor pressure at two heights above the surface. For open water surfaces, the surface temperature and vapor pressure are sometimes used in conjunction with a measurement at one height above the surface. The Bowen ratio, β, which is defined as the ratio of the sensible heat flux (H) to the latent heat flux (LE), is then approximated as the ratio of vertical gradient in temperature to the vertical gradient of vapor pressure, $\Delta T/\Delta e$. To estimate the absolute value of the fluxes under conditions of no advection (i.e., it is assumed that the energy available for sensible and latent heat flux is given by (R_{net} - G)), and the latent heat flux is given by:

$$LE = \frac{(R_{net} - G)}{(1 + \beta)}. \tag{1.7}$$

The sign convention for the fluxes represented by LE, R_{net}, and G is for fluxes toward the surface to be positive and fluxes away from the surface to be negative. The estimates of sensible and latent heat flux obtained by this technique are not independent of one another, and there is no means to check the assumption that all the available energy is given by (R_{net} - G). The validity of this method is also dependent on the similarity of the temperature and humidity profiles above the surface (Brutsaert, 1982). The accuracy of the energy-balance Bowen ratio technique (EBBR) has been the subject of many studies (e.g., Fuchs and Tanner, 1970; Sinclair et al., 1975).

The eddy correlation technique involves a more direct and independent measurement of the sensible and latent heat fluxes. With this technique, simultaneous measurements of the rapid fluctuations in vertical windspeed, temperature, and specific humidity are made with special fast-response sensors. Sensible heat flux is computed as the covariance of the vertical velocity and temperature; latent heat flux is computed as the covariance of vertical velocity and specific humidity. This technique requires fewer assumptions about the near-surface atmosphere than does the EBBR technique. Energy balance is not implicitly assumed in the calculation of the fluxes; hence, measurement of all four components of the energy balance (R_{net}, G, H, LE) can be used to check the closure of the energy-balance relationship. However, the instrumentation required for these systems is delicate and takes considerable care to install, maintain, calibrate, and operate (Arya, 1988).

Techniques Utilizing Remote Sensing Data

Regional Scale. Methods for estimating evapotranspiration on a regional scale usually involve the use of thermal infrared satellite data and ground-based meteorological measurements, used as input to a one-dimensional boundary layer model. These models are similar to some of the less complex models described in the section above on soil/plant/atmosphere simulation models (Carlson and Boland, 1978; Carlson et al., 1981; Taconet et al., 1986; Soer, 1980; Deardorff, 1978). Day and night surface temperatures have been used in conjunction with relatively simple models to estimate soil thermal inertia (the product of thermal conductivity and heat capacity) and daily evaporation rates (Rosema et al., 1978). Price (1980, 1982) used an analytical approach to develop a relatively simple model for daily ET that required two surface temperature measurements within a diurnal cycle and standard meteorological quantities (assumed to be constant over very large areas of interest, on the order of 200 km^2). He concluded that these types of methods were somewhat useful for computing large-scale trends in evapotranspiration, but were limited in part by the spatial scale over which ground meteorological inputs could be extended.

Local Scale. The basis of the technique to estimate latent heat flux over homogeneous surfaces with a combination of remote sensing data and ground data is the surface energy-balance equation, given by:

$$R_{net} = G + H + LE. \tag{1.8}$$

In this form of the surface energy-balance equation, it is assumed that the additions and losses of energy due to advection, canopy storage, and photosynthesis are negligible. R_{net} is the net radiation flux, G is the soil heat flux, H is the sensible heat flux, and LE is the latent heat flux; all fluxes are given in Wm^{-2}. The flux represented by R_{net} is positive when directed toward the surface. The fluxes represented by G, H, and LE are positive when directed away from the surface. The overall strategy to estimate LE will be summarized first and then a more detailed description of the procedure for estimating each term will follow.

The four components of the net radiation term, R_{net}, are estimated using a combination of ground and remotely sensed data. The soil heat flux, G, is estimated as a fraction of the net radiation. That fraction is dependent on the amount of vegetation cover estimated from remotely sensed vegetation indices. The sensible heat flux, H, is evaluated with the simple bulk transfer relationship, in which H is a function of the surface-air temperature difference and an aerodynamic resistance to the transfer of heat (computed as a function of windspeed and canopy height). The latent heat flux term, LE, is then computed as the residual of the three known quantities in Equation (1.8).

The net radiation, R_{net}, is estimated from a combination of ground and remotely sensed data by considering the four major components of net radiation:

$$R_{net} = R_{s\downarrow} - R_{s\uparrow} + R_{l\downarrow} - R_{l\uparrow}, \tag{1.9}$$

where $R_{s\downarrow}$ is the incoming solar radiation (from approximately 0.15 to 4 μm), $R_{s\uparrow}$ is the outgoing (reflected) solar radiation, $R_{l\downarrow}$ is the incoming emitted long-wave radiation (approximately 4 μm to 1000 μm) from the sky, and $R_{l\uparrow}$ is the outgoing terrestrially emitted long-wave radiation, all given in Wm^{-2}. The incoming solar radiation is usually measured with a calibrated, ground-based, upward-looking pyranometer. The incoming long-wave radiation is estimated from ground-based measurements of air temperature and vapor pressure using the expression:

$$R_{l\downarrow} = \epsilon_a \sigma T_a^4, \tag{1.10}$$

where ϵ_a is the emissivity of the air, given by $\epsilon_a = 1.24*(e_a/T_a)^{1/7}$ (Brutsaert, 1975); σ is the Stefan-Boltzman constant ($Wm^{-2}K^{-4}$); T_a is the air temperature; and e_a is the vapor pressure (mb).

The outgoing terms of Equation (1.9) can be estimated using downward-looking remote sensing instruments at a variety of spatial scales. The reflected short-wave radiation measured by remote sensing instruments is measured in finite wavebands which do not cover the entire shortwave portion of the spectrum. However, Jackson (1984) demonstrated that the ratio of the radiance received in the finite wavebands of various sensors to the outgoing short-wave radiance over the whole shortwave portion of the spectrum (referred to by Jackson (1984) as the "partial to total" ratio) can be reliably quantified. The remote sensing measurements of the "partial" outgoing short-wave radiance are converted to $R_{s\uparrow}$ using the empirically determined partial/total ratios for a particular sensor. The outgoing long-wave radiance, $R_{l\uparrow}$, is estimated from the remotely sensed surface temperature, T_s, and the expression:

$$R_{l\uparrow} = \epsilon_s \sigma T_s^4, \tag{1.11}$$

where ϵ_s is the emissivity of the surface. It should be noted that the remotely sensed upwelling radiance (Wm^{-2}) represents the outgoing radiant flux density in the thermal bandpass of that particular sensor. Knowledge of the absolute value of the surface temperature or emissivity is not required for the calculation of $R_{l\uparrow}$.

The soil heat flux, G, is traditionally measured with soil heat plates placed just below the soil surface. It is not possible to estimate G directly with remote sensing data, because it is dependent on soil thermal properties and a subsurface soil temperature. For mature field crops with substantial vegetation cover and a small fraction of exposed bare soil, G is typically a small term in the energy-balance equation (less than 10% of R_{net} (Reginato et al., 1985)). Expressions which relate the ratio of G/R_{net} to spectral vegetation indices (combinations of spectral reflectance values in the visible and near-infrared wavebands) were proposed and tested over agricultural crops by Clothier et al. (1986) and Kustas and Daughtry (1990). These have the general form:

$$G = R_{net} (a - b*(NIR/RED)), \tag{1.12}$$

where NIR/RED is the ratio of the reflectances observed in the near-infrared and red bands, respectively. The constants a and b are empirically derived and would be expected to vary with sun angles and canopy type. However, for several crop types evaluated in the studies mentioned above, the constants did not vary significantly from values of a = 0.3 and b = 0.015.

The physical basis for this expression lies in the fact that the portion of the total net radiation that reaches the soil can be theoretically shown to be exponentially related to the leaf area index (Goudriaan, 1977). It can also be shown (Asrar et al., 1984) that the vegetation index (NIR/RED) is exponentially related to the leaf area index. Assuming that the soil heat flux is proportional to the net radiation that reaches the soil, it is physically reasonable that the soil heat flux would be proportional to the vegetation index in a nearly linear manner. However, Equation (1.12) has not been widely tested over non-agricultural types of vegetation and with conditions of low vegetation cover. This topic will be investigated in Chapter 4 of this dissertation.

The last term in the energy balance to be estimated with remote sensing measurements is the sensible heat flux, H, given by Huband and Monteith (1986a) as:

$$H = \frac{\rho C_p (T_o - T_a)}{r_a}, \tag{1.13}$$

where T_o is the aerodynamic surface temperature, or the temperature at the virtual source/sink height for the sensible heat flux; T_a is the air temperature at a reference height above the canopy; r_a is the stability-corrected aerodynamic resistance to heat transfer. The bulk-transfer relation in Equation (1.13) is often given in terms of the surface temperature (T_s) in the numerator instead of the aerodynamic temperature

(T_o). The form given by Huband and Monteith (1986a,b) is used here because it is more generally applicable to various types of surfaces. Differences between surface temperature and aerodynamic temperature for different types of surfaces are discussed briefly below and in more detail in Chapter 4. Several different expressions can be used to estimate r_a (Mahrt and Ek, 1984; Choudhury and Idso; 1985) as a function of windspeed at a reference height and surface roughness lengths for the transfer of heat and momentum (commonly computed as an empirical functions of canopy height). This topic will be discussed in more detail in Chapter 4.

For nearly complete and homogeneous canopy cover, the surface temperature measured with remote sensing instruments is very close to the aerodynamic temperature. For such conditions, the remotely sensed surface temperature, T_s, is used in place of T_o in Equation (1.13). This method has been shown to provide reliable estimates of sensible heat fluxes using remotely sensed data from ground-based (Reginato et al., 1985), aircraft-based (Jackson et al., 1987), and satellite-based (Moran et al., 1990) instruments. Several researchers have utilized independent measurements of H from the Bowen ratio or eddy correlation techniques, together with Equation (1.13), to solve for T_o (Huband and Monteith, 1986a,b; Choudhury et al., 1986). In comparing T_o with T_s measured with ground-based remote sensing instruments, it was observed that, even for homogeneous surfaces with nearly full canopy cover, such as mature wheat, there are differences between T_o and T_s on the order of 1-2°C. While some of this difference may be due to uncertainties in the estimation of r_a, it was suggested that the discrepancy may also be due to: (1) errors in the value of the surface emissivity, which is a parameter that relates the kinetic temperature of the surface to the radiometric temperature measured by remote sensing instruments, and (2) complexities of heat exchange within the canopy which give rise to small variations in the virtual source/sink height for heat transfer, causing it not to be at the level of the canopy surface sensed by remote sensing instrumentation.

In summary, the remote sensing technique for estimating latent heat flux, LE, involves the estimation of the R_{net}, G, and H components of Equation (1.8) with a combination of ground and remotely sensed data and solving for the LE term as the residual. For relatively homogeneous surfaces with nearly complete vegetation cover, the LE values computed with this technique agree well with LE values estimated by the Bowen ratio or eddy correlation techniques. The spatial scale over which this technique can be applied is limited by the area over which the ground-based measurements of temperature, vapor pressure, windspeed, and canopy height can be extended (Reginato et al., 1985). An analysis of the sensitivity of the LE values to errors in the observed input variables described above can be found in Moran (1990).

The Challenges of Estimating Fluxes with Remotely Sensed Data Over Surfaces With Partial Vegetation Cover

For surfaces with partial vegetation cover, the surface temperature derived from remotely sensed observations is a function of the emissivity and kinetic temperatures of both the soil and vegetation components of the surface. For partial canopy conditions, particularly when the soil surface is dry and the vegetation is actively transpiring, the kinetic temperature of the soil and vegetation components can be quite different (Kustas et al., 1990; Humes et al., 1991), and that difference varies throughout the diurnal heating cycle.

The degree to which these component temperatures contribute to the composite surface temperature is proportional to the fraction of exposed vegetation and soil surface. However, these component temperatures contribute to the aerodynamic temperature in proportion to the aerodynamic resistances to heat transfer between the soil or vegetation and the inter-canopy airspace. Thus, the surface temperature measured over partial canopy surfaces with remote sensing instruments is often significantly higher than the aerodynamic temperature (Stewart et al., 1989; Kustas et al., 1987; Kustas et al., 1989a). This causes an overestimation of the sensible heat flux (H) when the surface temperature is used in place of the aerodynamic temperature in Equation (1.13), which leads to an underestimation of latent heat flux (LE) using Equation (1.8).

There are also significant complexities in the estimation of roughness parameters and transfer coefficients for surfaces with partial vegetation cover (Verma and Barfield, 1979; Garratt, 1980; Hatfield, 1989; Kustas et al., 1989b). The empirical relationships used to relate canopy height to roughness lengths (Brutsaert, 1982) have not been shown to be valid over surfaces with partial vegetation cover.

Additionally, the soil heat flux term, G, is significantly larger for surfaces of partial vegetation cover than for surfaces with more complete vegetation cover.

Because G is usually quite small for conditions of complete vegetation cover, errors in the estimate of this component for surfaces with nearly complete vegetation cover do not significantly impact the estimation of LE in Equation (1.8). However, for surfaces with partial vegetation cover, errors in the estimation of G can give rise to significant errors in the estimation of the LE with Equation (1.8).

Recently, Ham et al. (1990, 1991) showed experimentally that the evaporation and transpiration contributions of the soil and vegetation components of a partially vegetated surface can be the result of very complex and highly variable interactions within the soil-canopy-atmosphere system. It is indeed challenging to try to estimate the net surface fluxes arising from these complex dynamics by using a combination of remotely sensed data and commonly available ground data. This topic will be explored further in Chapter 4.

Scope of This Research

The main objectives of the research described in this dissertation were as follows:

(1) To better understand and quantify the surface parameters which control the partitioning of available energy at the land surface into sensible and latent heat flux;

(2) To develop and validate, at the scale of single ground-based flux stations, techniques to estimate latent and sensible heat flux as directly as possible from a combination of remotely sensed

data types and commonly available ground data for an area with partial vegetative cover;

(3) To utilize those techniques on a pixel-by-pixel basis to generate a spatially distributed map of latent and sensible flux for experimental site of First ISLSCP (International Satellite Land Surface Climatology Project) Field Experiment (FIFE); and

(4) To quantitatively evaluate the relationship between the variability of spatially distributed surface characteristics and the variability of remotely sensed observables used to estimate them.

In order to accomplish these objectives, the five topics described below were addressed. Each topic is presented in subsequent chapters as indicated.

Topic 1: Evaluation of a Widely Used Empirical Coefficient for the Partitioning of Sensible and Latent Heat Flux

One of the simplest expressions often used to estimate the amount of available energy used as latent heat flux is the well-known Priestley-Taylor (1972) equation. This expression was intended to be used to estimate regional scale latent heat flux for conditions in which evapotranspiration is limited by the available energy. Because of its simplicity, it is widely used as a method to partition the available energy into sensible and latent heat flux. In Chapter 2, the expression was evaluated analytically to better understand the physical factors influencing the value of the partitioning coefficient in that expression. The partitioning coefficients, for which many researchers have reported experimentally determined values, were analytically evaluated in terms of several controlling surface parameters included in the resistance-combination (Penman-Monteith) equation for evapotranspiration. Using values of surface parameters typical for different types of surfaces (i.e., open water, grassland, agricultural crop, forest), the range of values for the partitioning coefficient predicted by the analytical evaluation was in general agreement with the observed values of the partitioning coefficient over those various surface types reported in the literature. Typical diurnal and seasonal differences in atmospheric variables in the analytical expression were also shown to account for the trend and magnitude of observed diurnal and seasonal variations in the partitioning coefficient reported in the literature.

Topic 2: Evaluation of Surface Parameters Controlling the Partitioning of Available Energy Over Grassland Field Site

The remainder of the research topics were investigated with the use of field data from the FIFE (First ISLSCP (International Satellite Land Surface Climatology Project) Field Experiment), carried out over a prairie grassland in 1987 and 1989 (Sellers et al., 1988). Ground-based measurements of energy-balance components (Bowen ratio and eddy correlations measurements) at several ground sites were used in conjunction with ground-based soil moisture measurements to evaluate the surface and near-surface parameters influencing the partitioning of available energy into sensible and latent heat flux under various conditions. The results of this analysis (Chapter 3) suggested that different surface characteristics influenced the partitioning of latent and sensible heat flux as a function of time since wetting. This analysis also suggested that, in order to estimate fluxes from a combination of remotely sensed and commonly available ground data, the remotely sensed observations needed to provide an integrated effect of many complex and interacting surface processes.

Topic 3: Use of Remotely Sensed Data to Estimate Energy-Balance Components at Local Scales

In Chapter 4, various methods for estimating surface soil heat flux, sensible heat flux, and latent heat flux from a combination of ground and remotely sensed data were evaluated. Ground-based, aircraft-based, and satellite-based remote sensing data were used in conjunction with flux data from many of the FIFE ground sites to evaluate relationships between radiometric surface temperature and aerodynamic temperature under various surface conditions. Based on these relationships, an algorithm was developed to compute surface fluxes from satellite based remotely sensed data and ground-based estimates of near-surface air temperature and windspeed. This algorithm was validated by comparison with ground-based surface flux measurements and was compared to the fluxes estimated from remotely sensed data using the traditional model described above and with a modification of that model described by Kustas et al. (1989a).

Topic 4: Production of Distributed Map of Latent and Sensible Heat Flux Over the FIFE Site

In Chapter 5, a spatially distributed map of "instantaneous" soil heat flux, sensible heat flux, and latent heat flux for the FIFE site was developed utilizing, on a pixel-by-pixel basis, the algorithm developed and validated in Chapter 4. The data used to produce the spatially distributed fluxes included: (a) an atmospherically corrected Landsat Thematic Mapper image of the FIFE site on August 15, 1987, (b) a spatially distributed map of net solar radiation (corrected for topographic effects) produced by Dubayah et al. (1990) from the same Landsat TM image, and (c) ground-based estimates of air temperature, windspeed, vapor pressure, and estimates of canopy height for different vegetation classes.

Topic 5: Spatial Scaling: Relationship Between Variability in Spatially Integrated Surface Characteristics and Variability in Derived Parameters

In Chapter 6, an approach was evaluated which provides a framework to quantify the relationship between the variability of the surface properties observed with remote sensing (e.g., reflectances in particular wavebands) and surface parameters derived from those observations at various spatial scales. The example used to demonstrate this approach was that of the Normalized Difference Vegetation Index computed from red and near-infrared surface reflectances. The differences between the mean of the distributed values of NDVI over area of increasing spatial scale were compared to the values of NDVI computed with "lumped" values of red and near-infrared reflectances. The difference between the lumped and distributed values was quantified in terms of the variance of the red and near-infrared reflectances and the second derivative of the function with respect to the reflectances. This approach was shown to be a useful one for quantifying the differences in distributed and lumped responses for a non-linear function.

Note on Surface Flux Terminology

All of the surface fluxes described throughout this dissertation are in units of energy per unit time per unit area (most commonly given in $Wm^{-2)}$. In many fields which involve rigorous use of radiometric principles and terminology, a quantity with these units is correctly referred to as a surface flux density, as opposed to a surface flux. However, in the field of micrometeorology, a surface flux density is much more commonly referred to simply as a "surface flux". In order to be consistent with the more widely accepted terminology for the field of application, the terminology "surface flux" will be utilized throughout this dissertation, but with the recognition that the more rigorous terminology would utilize the term "surface flux density".

CHAPTER 2

AN ANALYTICAL EVALUATION OF THE PRIESTLEY-TAYLOR EQUATION

Introduction

A widely used equation for estimating the fraction of available energy used for evaporation from a well-watered surface with minimal advection was given by Priestley and Taylor (1972) as:

$$LE = \alpha\left(\frac{\Delta}{\Delta + \gamma}\right)[R_{net} - G]. \tag{2.1}$$

The notation and units for the equation variables are given in Table 2.1, and α is an empirically derived coefficient. This equation was an extension of the concept of equilibrium evaporation (Priestley, 1959; Slatyer and McIroy, 1961). The concept of equilibrium evaporation holds that, when unsaturated air is in contact with a saturated surface over a long fetch, it will tend to become saturated, and amount of available energy used in evaporation from the surface is given by the expression:

$$LE = \left(\frac{\Delta}{\Delta + \gamma}\right)[R_{net} - G]. \tag{2.2}$$

Note that when α approaches 1, the Priestley-Taylor expression is equal to the Slatyer and McIroy (1961) equilibrium evaporation and the Bowen ratio, β (H/LE), approaches Δ/γ. The value of Δ, the slope of the saturation vapor pressure versus temperature curve, is evaluated at the near-surface air temperature.

Table 2.1. List of Notations

R_{net} = Net radiation	Wm^{-2}
G = Soil heat flux	Wm^{-2}
H = Sensible heat flux	Wm^{-2}
LE = Latent heat flux	Wm^{-2}
Q_n = Total energy flux available to be used for evaporation	Wm^{-2}
E = Rate of evaporation	$kgs^{-1}m^{-2}$
L = Latent heat of vaporization of water	$J\ kg^{-1}$
ρ = Density of air	$kg\ m^{-3}$
C_p = Heat capacity of air	$J \times kg^{-1}\ C^{-1}$
γ = Psychrometric constant, C_p/L	mbar C^{-1}
T_s = Surface temperature	°C
T_a = Air temperature at reference height	°C
e_s^* = Saturated vapor pressure at T_s	mbar
e_a^* = Saturated vapor pressure at T_a	mbar
e_a = Vapor pressure at reference height	mbar
r_a = Aerodynamic resistance for transport of heat and water vapor from surface to reference height	sm^{-1}
r_s = Surface resistance to evaporation	sm^{-1}
f_E = Evaporation fraction, $LE/(LE + H)$	---
Δ = Slope of saturated vapor pressure vs. temperature curve, evaluated at some temperature	mbar C^{-1}
γ^* = $\gamma(1 + r_s/r_a)$	mbar C^{-1}
β = Bowen ratio, H/LE	

The value of the empirical coefficient α has been interpreted to be related to the departure of the surface from the concept of equilibrium evaporation. This relationship was intended for use at large spatial scales on the order of tens of thousands of square kilometers. It was based, in part, on a consideration of the physical processes in the planetary boundary layer and on assumptions about the relative sizes of the advective and radiant energy inputs of large land areas. Using data sets for several different types of surfaces, including open water and various vegetation types, Priestley and Taylor (1972) reported a range of α values from 1.08 to 1.32 for daily evaporation and recommended an average daily value of α = 1.26.

Since then, many studies have evaluated the value of α for various types of surfaces and conditions. For open water surfaces, grasses, and short crops, most researchers have reported average daily values fairly close to 1.26. A summary of these investigations and the reported values of average daily α are provided in Table 2.2. Most of the investigations over surfaces which consisted either of open water or areas with short, well-watered vegetation reported average daily values near 1.26. An investigation over saturated bare soil reported by Barton (1979) provided a somewhat mean lower daily value for α (1.08).

In a study carried out over a large lake, de Bruin and Keijman (1979) found a mean daily value of 1.29 for data collected over summer months. However, they also reported a strong diurnal variation in the value of α, ranging from 1.15 early in the day to 1.42 in midafternoon. They also reported seasonal variations in monthly

Table 2.2. Summary of α Values Reported by Various Investigators. Unless otherwise noted, most values are average daily values.

Investigation	Surface Conditions	α Value
Priestley-Taylor, 1972	Open water and various short vegetation types	1.26
Davies and Allen, 1973	Irrigated ryegrass	1.27
Jury and Tanner	Potatoes	1.28
Mukammal and Neumann, 1975	Grass	1.29
Stewart and Rouse, 1977	Lakes and wet meadows	1.26
Barton, 1979	Bare soil	1.05
DeBruin and Keijman, 1979	Lake (summer, monthly mean) Lake (spring/fall, monthly mean)	1.29 1.5
McNaughton and Black, 1973	Douglas fir forest, dry Douglas fir forest, wet	1.05 1.18
Black, 1979	Douglas fir forest (dry; thinned) Douglas fir forest (dry; unthinned)	0.80 0.84
Shuttleworth and Calder, 1979	Spruce forest (dry; daytime) Spruce forest (wet; advective conditions) Pine forest (wet)	0.6-0.8 8.5-11.5 1.44-1.79

average values that ranged from 1.20 in August to values near 1.5 for the spring and fall months.

Based on a relationship between Bowen ratio and air temperature derived from several sets of field data, Davies and Allen (1973) reported that the range of possible α values is relatively small (1.26-1.27) for the temperature range 15-30°Celsius (C). Brutsaert (1982) characterized the agreement in the α values observed under non-water-limiting conditions over many different types of surfaces, including open water, grass, and short crops, as "remarkable". He conjectured that this was likely due to a fortuitous compensation of specific humidity of non-wet leaf surfaces by a larger effective roughness and thus larger transfer coefficient for the vegetated surfaces. In the work reported here, that interaction is quantified in a manner which explains the range of α values observed for various surfaces.

The studies carried out over forested areas, however, showed much more variation in observed α values than those over water and short crops. When the root-zone of a forest canopy was well-supplied with moisture, but there was no water on the vegetation surfaces from interception or condensation (a "dry" forest canopy), fairly small values of α were observed (0.6-1.05). When intercepted water was available for evaporation, the α values were generally larger (1.18-1.79). Because of the wide range of α values they observed, Shuttleworth and Calder (1979) questioned the relevance of the Priestley-Taylor concept for the spruce and pine forests. They warned against the indiscriminate use of any simplistic equation with a large empirical content and concluded with the statement that "the laws of physics are not influenced by human desire for computational simplicity".

Efforts to extend the Priestley-Taylor relationship beyond the non-water-limited, non-advective conditions for which it was intended by making empirical adjustments to the α factor have also been reported. Jury and Tanner (1975), working with two seasons of data over irrigated potatoes, proposed an empirical correction to the α parameter to account for conditions of high local advection. This correction was a function of the ratio of average vapor pressure deficit for the advective period to the average annual vapor pressure deficit for the site.

Other researchers have developed empirical corrections to the α factor to extend the use of the expression to conditions in which available soil moisture, as opposed to available energy, limits evapotranspiration. Priestley and Taylor (1972) considered this topic in their original study; they concluded that the critical water content at which evapotranspiration became moisture-limited varied considerably for different types of surfaces (bare soil and different vegetation types) and hence could not be generalized for all types of surfaces. Davies and Allen (1973) developed an empirical correction to α which was an exponential function of the available soil moisture for their ryegrass sites. Recently, Flint and Childs (1991) developed such an expression for moisture-limited conditions over a partially vegetated clearcut forest site.

The α factor is also used in the advection-aridity approach advanced by Brutsaert and Stricker (1979). In their approach, the Bouchet (1963) concept of a complementary relationship between potential and actual transpiration is combined with the regional advection effects implicit in the equilibrium evaporation concept.

In keeping with large-scale application of the Priestley-Taylor relationship that was originally intended, there have been successful attempts to model the value of the α parameter (de Bruin, 1983; McNaughton and Spriggs, 1986, 1989) with a simple model of the atmospheric boundary layer (ABL) coupled with the Penman-Monteith equation. These models include ABL parameters such as temperature and humidity profiles, rate of growth of the ABL height, and rate of entrainment of dry air at the top of the ABL, as well as surface parameters controlling evaporation, notably, aerodynamic resistance (r_a) and surface resistance to evaporation (i.e., canopy resistance, stomatal resistance, r_s). de Bruin (1983) reported that, for ABL conditions typical of those for a sunny summer day in the mid-latitudes, α was primarily controlled by the surface resistance parameter, r_s, when $r_s < 120\ sm^{-1}$, and only slightly controlled by r_a. When $r_s > 120\ sm^{-1}$, α was more sensitive to r_a. Using the ABL model with different assumed values for r_a and r_s, good agreement was obtained with the α values reported in the literature for various surface types. The model also predicted diurnal variations in the α parameter consistent with observations, including fairly constant values during the midday hours when evaporation was highest.

Although the Priestley-Taylor equation was intended to be used as an estimate of regional evaporation, the simplicity and minimal input data requirements have made the Priestley-Taylor equation a popular choice for applications at various scales. It has often been applied to smaller scales; indeed, validation and calibration of the empirical coefficient is by necessity usually done by comparison to a single ground station.

Objectives

The main points to be addressed in the remaining sections of this chapter are:

(1) To show the algebraic relationship between the Priestley-Taylor α parameter and the surface parameters used in the Penman-Monteith combination equation;

(2) To use this relationship, together with typical values of the Penman-Monteith controlling parameters, to predict the corresponding range of values for α for different surface types;

(3) To compare the range of α values predicted in this manner to values observed in empirical studies;

(4) To evaluate whether or not the trend toward stable values for short crops versus more variable values for forested areas, as well as observed daily and seasonal variations, can be attributed to the differences in typical values of Penman-Monteith controlling parameters for those surfaces;

(5) To provide a better understanding of the conditions under which α would be expected to be relatively constant and conditions under which it would be expected to vary, thus

providing guidelines about the range of conditions under which values attained in previous studies over particular surfaces can be applied to other surfaces and conditions.

Theory

The resistance forms of the bulk-transfer relationships describing the fluxes of sensible and latent heat fluxes are given by the following expressions (Monteith, 1973):

$$H = \rho C_p\,(T_s - T_a)/r_a; \tag{2.3}$$

$$LE = \rho C_p\,(e_s^* - e_a)/\gamma(r_a + r_s). \tag{2.4}$$

T_s is the surface temperature and e_s^* is the saturated vapor pressure at that temperature.

The evaporative fraction, f_E, describes the fraction of energy available for either latent or sensible heat flux which is actually expended as latent heat flux, described by the expression:

$$f_E = \frac{LE}{LE + H}. \tag{2.5}$$

Dividing the right-hand side of Equation (2.5) by LE yields the relationship between the evaporative fraction and Bowen's ratio, β:

$$f_B = \frac{1}{1+\beta}. \tag{2.6}$$

Substituting Equation (2.3) and Equation (2.4) into Equation (2.5), one obtains:

$$f_B = \frac{\dfrac{e_s^* - e_a}{T_s - T_a}}{\dfrac{e_s^* - e_a}{T_s - T_a} + \gamma(1 + \dfrac{r_s}{r_a})}. \tag{2.7}$$

In order to maintain consistency with expressions given in the literature, the term Δ is introduced, which is the slope of the saturated vapor pressure versus temperature curve $((e_s^*-e_a^*)/(T_s-T_a))$, where e_a^* is the saturated vapor pressure at air temperature. The numerator and first term of the denominator in Equation (2.7) can be expressed as:

$$\frac{e_s^* - e_a}{T_s - T_a} = \Delta + \left(\frac{e_a^* - e_a}{T_s - T_a}\right). \tag{2.8}$$

Substituting Equation (2.8) into Equation (2.7) yields the following expression for f_E:

$$f_E = \frac{\Delta + \left(\dfrac{e_a^* - e_a}{T_s - T_a}\right)}{\Delta + \dfrac{e_a^* - e_a}{T_s - T_a} + \gamma\left(1 + \dfrac{r_s}{r_a}\right)}. \tag{2.9}$$

Without yet assuming which terms of the energy balance can be neglected, the energy used for latent heat flux can then be expressed as:

$$LE = f_E \cdot Q_n, \tag{2.10}$$

where Q_n is the total energy available to be used as either sensible or latent heat flux. Substituting Equation (2.9) into Equation (2.10), one obtains the following expression for the latent heat flux:

$$LE = \frac{\Delta + \left(\dfrac{e_s^* - e_a}{T_s - T_a}\right)}{\Delta + \dfrac{e_s^* - e_a}{T_s - T_a} + \gamma\left(1 + \dfrac{r_s}{r_a}\right)} \cdot Q_n. \tag{2.11}$$

The equation given by Priestley and Taylor (1972), prior to the assumption that $Q_n = R_{net} - G$, is:

$$LE = \alpha \frac{\Delta}{\Delta + \gamma} [Q_n]. \tag{2.12}$$

From comparison of Equation (2.10) and Equation (2.12), the relationship between the evaporative fraction and the Priestley-Taylor α parameter is:

$$f_E = \alpha \frac{\Delta}{\Delta + \gamma}. \tag{2.13}$$

Substituting Equation (2.9) into Equation (2.13) and rearranging, one obtains an analytical expression for the Priestley-Taylor α parameter, i.e.:

$$\alpha = \frac{\Delta + \left(\dfrac{e_s^* - e_a}{T_s - T_a}\right)}{\Delta + \dfrac{e_s^* - e_a}{T_s - T_a} + \gamma\left(1 + \dfrac{r_s}{r_a}\right)} \Big/ \frac{\Delta}{\Delta + \gamma}. \tag{2.14}$$

It is useful to evaluate special cases of Equation (2.14). When the surface resistance is equal to zero (as is the case for an open water surface or for evaporation of intercepted water from a canopy) and the vapor pressure deficit above the canopy goes to zero, then $\alpha = 1$ as expected based on the equilibrium evaporation concept. However, it is interesting to note that, even when the vapor pressure deficit goes to zero (as in the case of equilibrium evaporation concept), as long as the surface resistance to evaporation is non-zero, the value of α under the so-called equilibrium conditions is given by $(\Delta + \gamma)/(\Delta + \gamma^*)$, where $\gamma^* = \gamma(1+r_s/r_a)$.

Under conditions of no advection, the surface energy balance is:

$$R_{net} = G + H + LE \tag{2.15}$$

and the energy available to be used as either sensible or latent heat flux is:

$$Q_n = R_{net} - G. \tag{2.16}$$

Equation (2.12) now becomes:

$$LE = \frac{\Delta + \left(\dfrac{e_s^* - e_a}{T_s - T_a}\right)}{\Delta + \dfrac{e_s^* - e_a}{T_s - T_a} + \gamma\left(1 + \dfrac{r_s}{r_a}\right)} (R_{net} - G). \tag{2.17}$$

Additionally, the assumption that the energy balance is given by Equation (2.15) provides a constraint between the variables in Equation (2.17). As shown by Jackson et al. (1977), by substituting Equation (2.3) and Equation (2.4) into Equation (2.15) and rearranging, one obtains:

$$T_s - T_a = \frac{r_a(R_{net}-G)\gamma^* - \rho C_p\,(e_a^* - e_a)}{\rho C_p(\Delta + \gamma^*)}, \tag{2.18}$$

where γ^* is:

$$\gamma^* = \gamma\left(1 + \frac{r_s}{r_a}\right). \tag{2.19}$$

Hence, substituting Equation (2.18) into Equation (2.17) and simplifying, one obtains an expression for LE of the form:

$$LE = \left[\frac{\Delta}{\Delta + \gamma^*} + \frac{\rho C_p(e_a^* - e_a)}{r_a(R_{net}-G)(\Delta + \gamma^*)}\right] \cdot (R_{net} - G). \tag{2.20}$$

It is easily seen that Equation (2.20) is algebraically identical to the common form of the Penman-Monteith (Monteith, 1973) combination equation, commonly given the form:

$$LE = \frac{\Delta\,(R_{net}-G) + [\rho C_p(e_a^* - e_a)/r_a]}{\Delta + \gamma^*}. \tag{2.21}$$

For purposes of examining the range of values for the Priestley-Taylor α parameter, it is more useful to use the form given in Equation (2.20) and express the α parameter as:

$$\alpha = \left[\frac{\Delta}{\Delta + \gamma^*} + \frac{\rho C_p(e_a^* - e_a)}{r_a(R_{net} - G)(\Delta + \gamma^*)}\right] / \frac{\Delta}{\Delta + \gamma}. \tag{2.22}$$

This equation is algebraically equivalent to one given in the appendix of Choudhury and Idso (1985), in the context of describing the importance of a model for surface, or canopy, resistance as an aid in interpreting the Priestley-Taylor coefficient. In the next section, typical values of γ^* for different surfaces are used to show that the range of α values observed for different surfaces can be quantitatively explained by the relationship of surface parameters given in Equation (2.22).

Computed Values of α for Different Surface Types

In this section, the ranges of α values predicted by Equation (2.22) are evaluated for four cases: open water, grass or short crop, forest (dry canopy), and forest (wet canopy). Assuming conditions of moderate windspeed (3 ms^{-1}) and plentiful soil moisture, typical values of r_a and r_s were used for these different surfaces and are summarized in Table 2.3.

From Equation (2.22), it can be seen that α is a function of five variables: Δ, $(R_{net}$-G), r_s, r_a, and $(e_a^* - e_a)$. For this analysis, the variables Δ and $(R_{net}$-G) were varied over reasonable ranges. Because Δ is a function of T_a, Equation (2.22) was

Table 2.3. Values for r_a, r_s Assumed for Typical Surfaces Under Conditions of Moderate Windspeed sm^{-1}

	r_a	r_s	r_s/r_a
Open Water	60	0	0
Grass, Short Crop	20	50	2.5
Forest, Dry Canopy	6	120	20
Forest, Wet Canopy	6	0	0

evaluated with a range of T_a values from 15-30°C; $(R_{net}\text{-}G)$ was varied from 100-600 Wm^{-2}. Values for r_s and r_a were fixed for each surface type at the values given in Table 2.3. The value of vapor pressure deficit was held constant for each of two cases evaluated for each different surface type; one case at $(e_a^*\text{-}e_a) = 10$ mbars and the other case at $(e_a^*\text{-}e_a) = 15$ mbars. The results for the lower vapor pressure deficit case (e_a^*- e_a = 10 mbars) are shown in Figure 2.1. The results for the higher vapor pressure deficit case ($e_a^*\text{-}e_a$ = 15 mbars) are shown in Figure 2.2.

Under actual field conditions, these variables are not independent. For example, $(R_{net}\text{-}G)$ and T_a are obviously dependent on one another; large T_a values would not occur at low R_{net} values. Additionally, although r_s and r_a were held constant here for each surface type, there are definite interactions between vapor pressure deficit and r_s (Choudhury and Monteith, 1986) and between r_s and $(R_{net}\text{-}G)$ which serve to narrow the allowable range of α values. All of the variables are expected to vary diurnally in a complex way which is influenced by the interactions between them. For example, in their analysis of the diurnal variation of α for well-watered wheat in Arizona, Choudhury and Idso (1985) noted the following interactions: (1) the product of r_a and R_{net} had less diurnal variation than either quantity separately, (2) the ratio of r_s/r_a remained fairly constant throughout the day although r_s and r_a each varied separately, and (3) most of the diurnal variation in α seemed to be due to diurnal variation in vapor pressure deficit.

Because the variables in Equation (2.22) are not independent, ranges of α values for a given surface are actually more constrained than the curves shown in

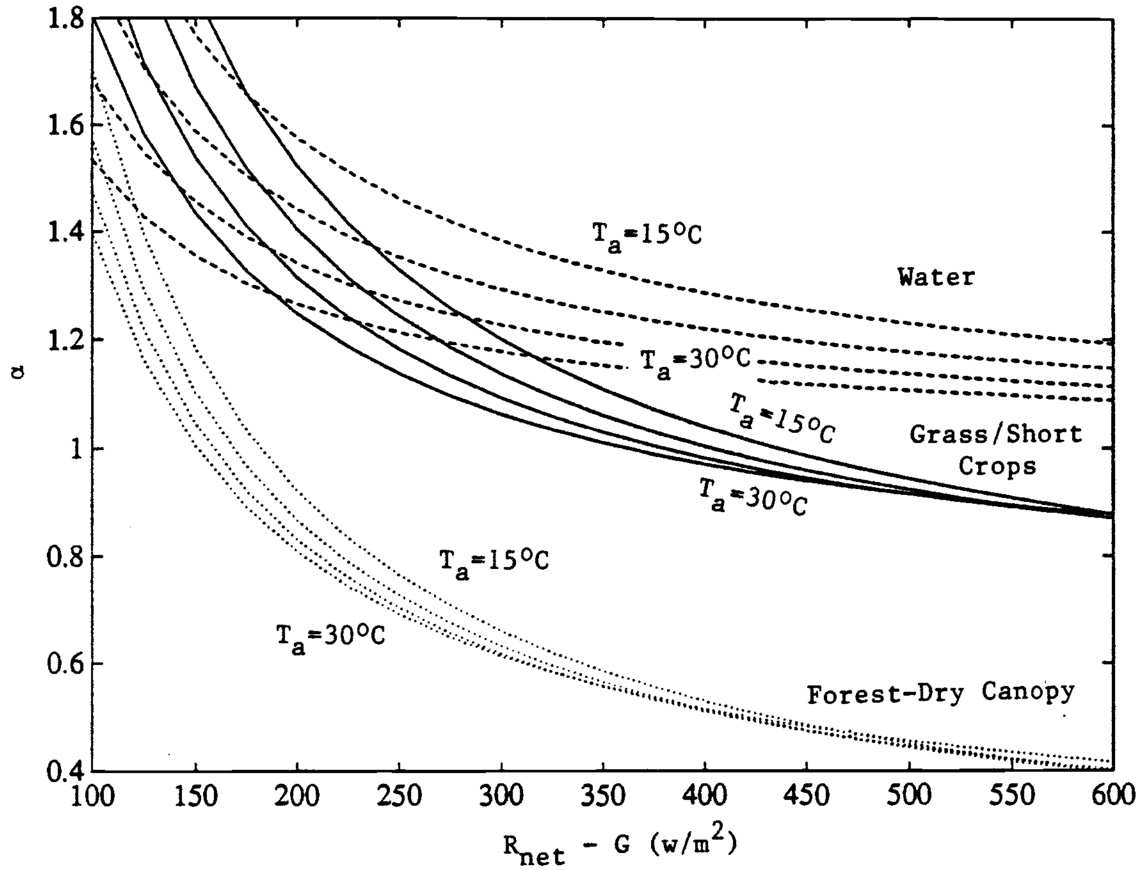

Figure 2.1. α values computed using typical resistance values for open water (dashed lines), grass/short crops (solid lines), and forest with dry canopy (dotted lines); different curves for each surface type represent a range of air temperature values from 15-30°C; vapor pressure deficit is fixed at 10 mbars.

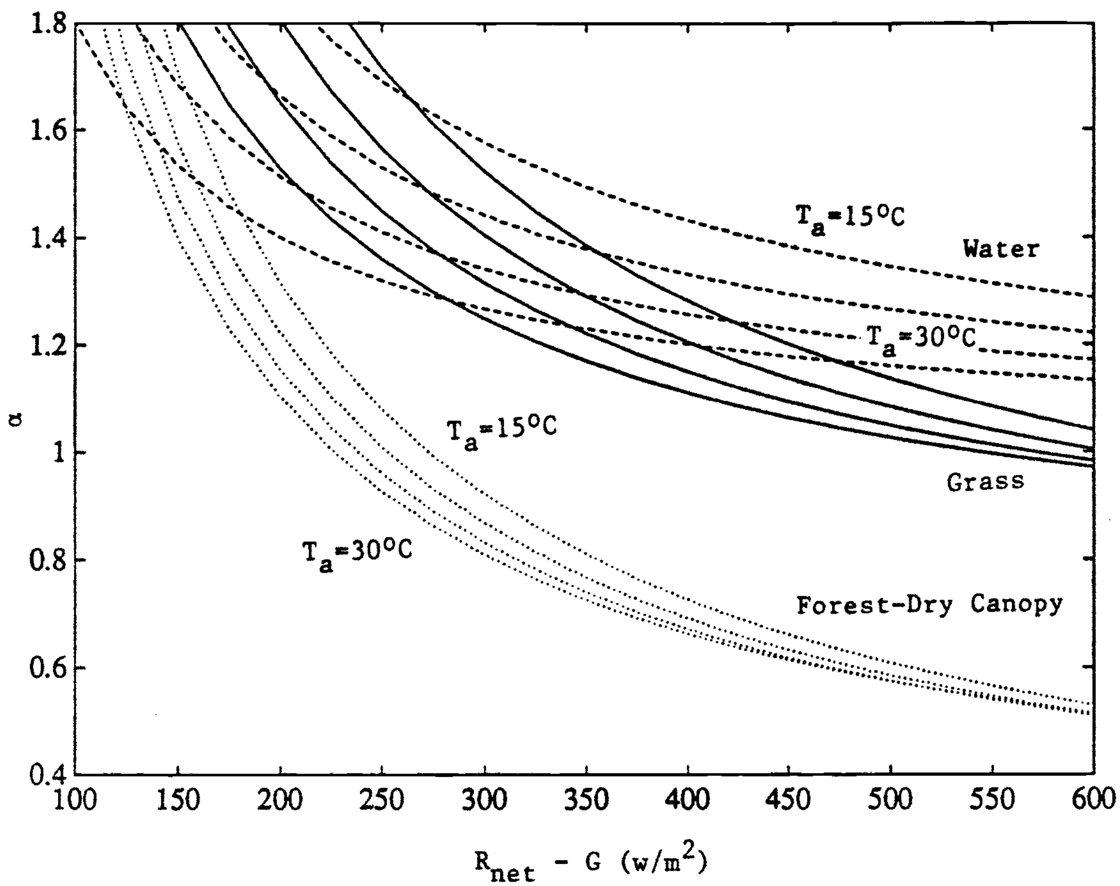

Figure 2.2. α values computed using typical resistance values for open water (dashed lines), grass/short crops (solid lines), and forest with dry canopy (dotted lines); different curves for each surface type represent a range of air temperature values from 15-30°C; vapor pressure deficit is fixed at 15 mbars.

Figures 2.2 and 2.3 would indicate. However, the major objective of this analysis was not to compute exact values of α under particular conditions, but rather to show how typical values of the five variables for each of the surface types tended to constrain α to the range of values observed in the literature for different surface types. Some general diurnal trends can also be verified by evaluating the curves in Figures 2.2 and 2.3 at different combinations of T_a, R_{net}-G, and vapor pressure deficit which would be typical for the different surface types at midday hours.

For the case of open water (dashed lines in Figures 2.1 and 2.2), the range of α values predicted by Equation (2.22) at midday values for R_{net} (approximately 300-500 W/m^2) is generally between 1.2-1.4. This is consistent with the observations of de Bruin and Keijman (1979) over a large lake in the Netherlands. As noted above, they also observed seasonal trend in the average values for α. For the spring and fall months, they reported an average α value of about 1.5; for the summer months, the average α value was closer to 1.20. An evaluation of Figure 2.2 suggests that this behavior is predicted by Equation (2.22). During the summer months, when T_a and R_{net} are at maximum values, the predicted α value is close to 1.20. For lower values of R_{net} and T_a, the predicted α values are near 1.50.

For the case of a surface with a relatively complete cover of moderate height grass or relatively short crops, the average daily values for the α parameter reported in the literature were generally close to α = 1.26. Half-hourly values of the α parameter computed from the Bowen ratio flux measurements taken over the grassland in central Kansas (the site of the FIFE Field Experiment) are shown in

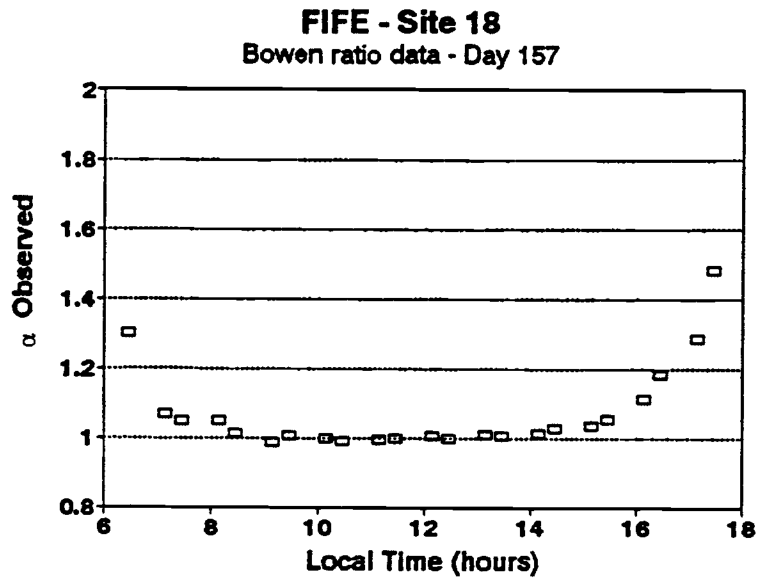

Figure 2.3a. Half-hourly values of the α parameter computed from fluxes measured with Bowen ratio system for FIFE Site 18, Day 149 (cloudy conditions most of the day).

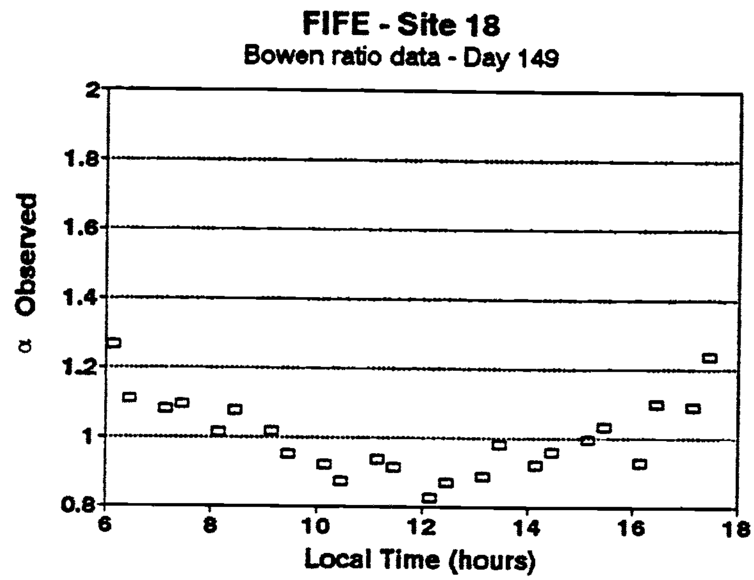

Figure 2.3b. Half-hourly values of the α parameter computed from fluxes measured with Bowen ratio system for FIFE Site 18, Day 157 (June 6, 1987, "Golden Day", clear conditions).

Figures 2.3a (cloudy conditions) and 2.3b (clear conditions). On both of these days, moisture in the root zone of the grassland was plentiful and conditions were near-potential. The midday value for α was close to 1.0 for both days, but was more constant for the day with clear conditions.

The curves shown in Figures 2.1 and 2.2 indicate that Equation (2.22) predicts α values which bracket this observed value for a surface with resistance values fairly typical of moderate height grass or relatively short crops. For (R_{net}-G) values typical of midday, when most of the evaporation would take place, α values are predicted to range from about 0.9-1.3 for the resistance values selected for this case (r_s = 50 sm^{-1}; r_a = 20 sm^{-1}). The diurnal variation in α shown in the half-hourly values from one of the FIFE sites is generally predicted by Equation (2.22) in that lower (R_{net}-G) values tend toward higher α values.

For the case of forested areas under conditions of a dry canopy (i.e., no free water on the canopy surface), most experimental studies reported in the literature provide an average daily α value of about 0.7. The curves shown in Figures 2.1 and 2.2 indicate that Equation (2.22) predicts values of α within that range. The ratio r_s/r_a is much larger for the forest (r_s/r_a = approximately 20) than for the short vegetation (r_s/r_a = approximately 2.5), which drives the values of α predicted by Equation (2.22) to significantly smaller values.

For the case of forested areas under conditions of a wet canopy, the wide range of α values predicted by Equation (2.22) is shown in Figure 2.4 for vapor pressure deficits of 5 mbars (dashed lines) and 10 mbars (solid lines). The striking

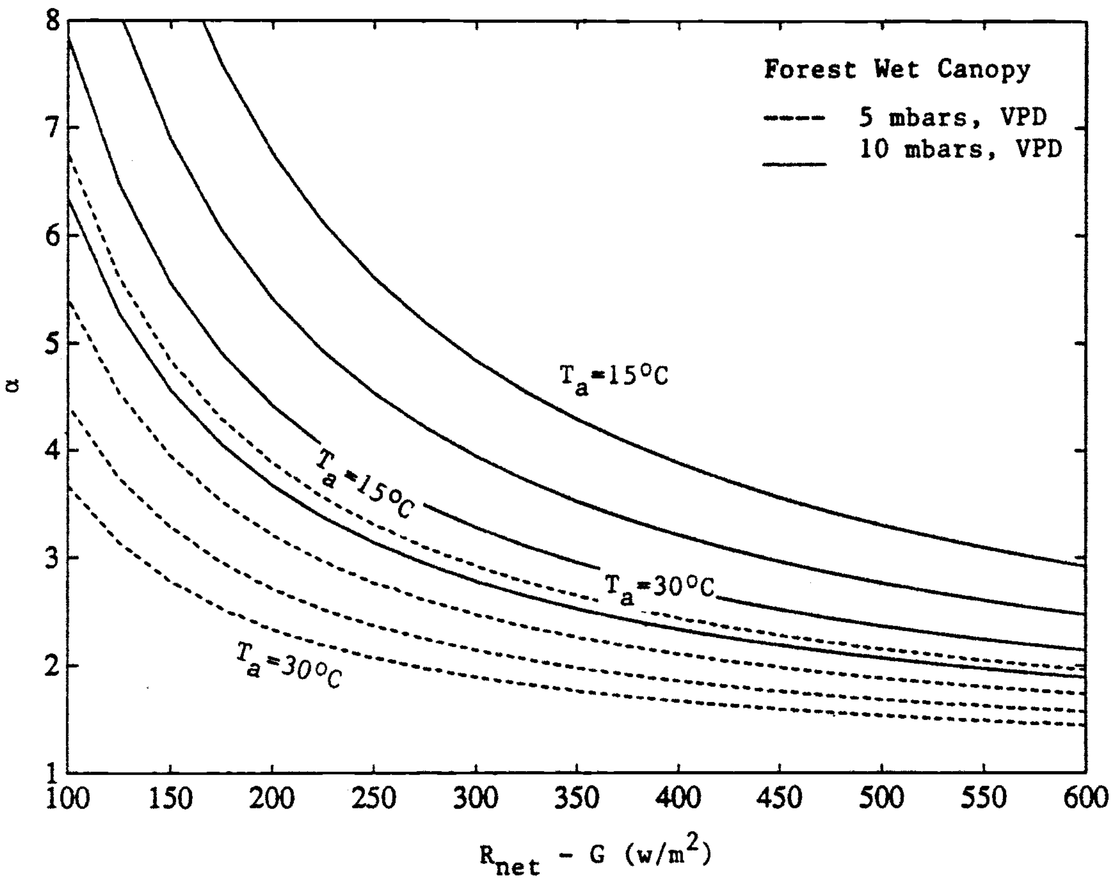

Figure 2.4. α values computed using typical resistance values for a forest with wet canopy conditions; different curves represent a range of air temperature values from 15-30°C; vapor pressure deficit is fixed at 5 mbars (dashed lines) and 10 mbars (solid lines).

difference between the curves for the wet canopy forest and those for other surfaces arises from the fact that the r_s/r_a ratio tends to zero for a wet canopy, while the r_a value is still quite small (assumed 6 sm^{-1} for this analysis). These widely varying values of α, which can be predicted from Equation (2.22), caused Shuttleworth and Calder (1979) to justifiably question the indiscriminate use of a constant value of α over different surfaces.

Discussion

One of the primary objectives of this analysis was to demonstrate that the Priestley-Taylor α factor, though treated in the literature as an invariant parameter, is simply a function of the physical parameters and variables which were intentionally ignored in developing the concept of equilibrium evaporation (i.e., the effects of near-surface vapor pressure deficit and aerodynamic and surface resistances). It is important to keep in mind that the equilibrium evaporation concept, and the Priestley-Taylor modification to it, were developed to describe evaporation over regional scales. The surface parameters and variables which control α (R_{net}-G, r_s, r_a, $e_a^*-e_a$) may vary considerably over regional scales and thus require less physical meaning at regional scales than at local scales. Attempts to model the α parameter with a coupled surface/boundary layer model are useful for considering the regional scale behavior of α. McNaughton and Spriggs (1989) and de Bruin (1983) showed that the surface resistance parameter (r_s) had a stronger effect on α than most of the atmospheric parameters and variables they considered, such as rate of entrainment at the top of the ABL.

However, almost all attempts to estimate the α parameter ultimately involve computations using flux estimates from a single surface flux station which measures a local-scale surface flux. At this scale, it is not necessary to invoke regional-scale boundary layer models to ascertain the factors controlling α, although the behavior of the regional-scale atmospheric boundary layer does exert an influence on the local-scale near-surface vapor pressure deficit and temperature. By comparing the Penman-Monteith combination equation with the Priestley-Taylor equation, it is a simple matter to quantify α in terms of near-surface vapor pressure deficit, aerodynamic, and surface resistances.

There is no fundamental physical basis to support the concept that α should be constant for different surface types. The analysis presented here quantifies and supports the hypothesis by Brutsaert (1982) that the close agreement in α factors observed over various surfaces is indeed due to a fortuitous interaction between values of r_a, r_s/r_a, and vapor pressure deficit typical for various surface types. This analysis also demonstrates that the large r_s/r_a ratios typical for forested areas give rise to the smaller values of α observed for forested areas than for open water or short crops. Additionally, because the canopy moisture status for a forest gives rise to very large variations in the r_s/r_a ratio, the large variations in α values observed under wet/dry canopy conditions (Shuttleworth and Calder, 1979) should be expected according to Equation (2.22).

One other issue addressed by this analysis is the validity of "calibrations" for the α factor which are derived under a particular set of experimental conditions. As discussed above, the interdependent relationships between the five parameters and variables controlling α will tend to constrain α to a moderately small range of values for particular surface types. However, Equation (2.22) suggests that there is a need for caution in extending a value for α that was derived for one experimental site under particular climate and vegetation conditions to other climate and vegetation conditions at that same site or other sites. It should be expected that α will be different for areas or conditions with significantly different values for the parameters controlling α, namely (R_{net}-G, T_a, r_a, r_s, and vapor pressure deficit). For example, a value of α calibrated for a particular site on a warm, sunny day with mild winds may be significantly different on a cooler, cloudy day with stronger winds. Furthermore, in extending values of α measured at one experimental site to other sites or other conditions, plant physiology and environmental conditions which control the ratio r_s/r_a should be expected to give rise to variations in α in the manner predicted by Equation (2.22).

Summary

The analysis described in this chapter shows that the algebraic relationship between the Priestley-Taylor equation and Penman-Monteith combination equation gives rise to an expression for the Priestley-Taylor α factor as a function of R_{net}-G, Δ (and, therefore, T_a), r_a, r_s, and vapor pressure deficit. These quantities appear in the second term of the combination equation; that term was intentionally ignored in the development of the concept of equilibrium evaporation at the regional scale and the Priestley-Taylor modification to that concept. The α factor has come to be viewed as an empirically derived factor and is usually calibrated on a local scale. By utilizing typical values for aerodynamic and surface resistances for different types of surfaces (open water, grass or short crop, forest with dry or wet canopy), and by varying the values of net radiation, air temperature, and vapor pressure deficit over reasonable ranges, it was shown that Equation (2.22) predicts ranges of values for α which are consistent with field observations of open water, short crop, and forest canopies under dry and wet conditions. The ranges of α values for each surface are quite strongly dependent on the near-surface vapor pressure deficit and the ratio of r_s/r_a for different surfaces.

CHAPTER 3

EVALUATION OF PARAMETERS CONTROLLING THE PARTITIONING OF SENSIBLE AND LATENT HEAT FLUX AT FIFE GROUND SITES

Introduction

A number of models are available which numerically simulate the transfer of moisture and heat in the soil/plant/atmosphere system. These models adequately describe the dynamics of those exchanges for surfaces with partial vegetation cover, but they require apriori knowledge of many parameters which are only valid over a relatively small spatial scale. Because the overall motivation for this research is to develop techniques to estimate surface fluxes in a spatially distributed manner with remotely sensed data, it is necessary to identify a few key parameters controlling those fluxes which can be observed at the scale of the intended application.

The focus of this chapter is to evaluate the effect of physical parameters such as amount of vegetation cover, surface soil moisture, and root-zone soil moisture on the partitioning of available energy into latent and sensible heat flux. The motivation for doing this is to try to identify, with experimental data, the first-order controlling processes which would define the minimum requirements for relatively simple formulations to estimate fluxes. These formulations must utilize observable parameters which capture the first-order controlling processes. In this chapter, those first-order controlling processes will be evaluated; subsequent chapters will focus on methods to capture the effects of these key controlling processes with remotely sensed data.

Background

The processes of evaporation from an exposed soil surface and transpiration from vegetation can be limited by one of two fundamentally different sets of factors. Just after precipitation or irrigation, when both the near-surface soil layer and the root zone are well-supplied with moisture, the evaporation and transpiration processes are limited by the amount of energy available for evaporation. These conditions are similar to those described for the concept of "potential" evaporation developed by Thornthwaite (1948). Since the development of that concept, our understanding of evaporation processes has evolved to include the concept that, even under non-moisture-limiting conditions, there is a non-zero surface resistance to evaporation controlled by the physiology of plants. Therefore, the rate of evaporation under energy-limited conditions is controlled by characteristics of the vegetation; different types of vegetation will have different rates of transpiration when well-supplied with moisture.

As moisture in the near-surface soil layer and the soil root-zone becomes less plentiful, the processes of evaporation and transpiration become limited by the amount of moisture available to be evaporated and transpired. The time at which this transition occurs, and the rate of evaporation and transpiration after that transition, are determined by soil parameters which control the storage and movement of moisture to the surface and the root zone, as well as vegetation characteristics which control the response of the vegetation to limited moisture. The rate of moisture-limited evaporation and transpiration is usually much slower than the rate of energy-limited evaporation. These two different modes of limitation for evaporation processes are conceptualized in Figure 3.1.

Even in the case of a local-scale area equivalent to the fetch for a single ground flux station (length scale of approximately 50 m), there is likely to be considerable heterogeneity in both root-zone and surface soil moisture. Therefore, even for a local-scale area, it is unlikely that all portions of the area will undergo this transition at the same time. Jackson et al. (1976) described the rate of evaporation from a bare soil surface as a linear combination of fractional areas undergoing energy-limited and moisture-limited evaporation. They deduced these fractional areas undergoing different processes from composite albedo measurements over the soil surface. This suggests that the proper use of variables measured over heterogeneous surfaces with remotely sensed data may involve the interpretation of those surface parameters as the combined effect of fractional areas undergoing different processes. As a first step, however, it is necessary to examine ground data which provide experimental evidence about the processes controlling the partitioning of available energy under various soil and vegetation conditions. Eventually, knowledge about the temporal and spatial variation in these controlling processes can perhaps be used to develop methodologies which can take optimal advantage of the various types of information available from remotely sensed data.

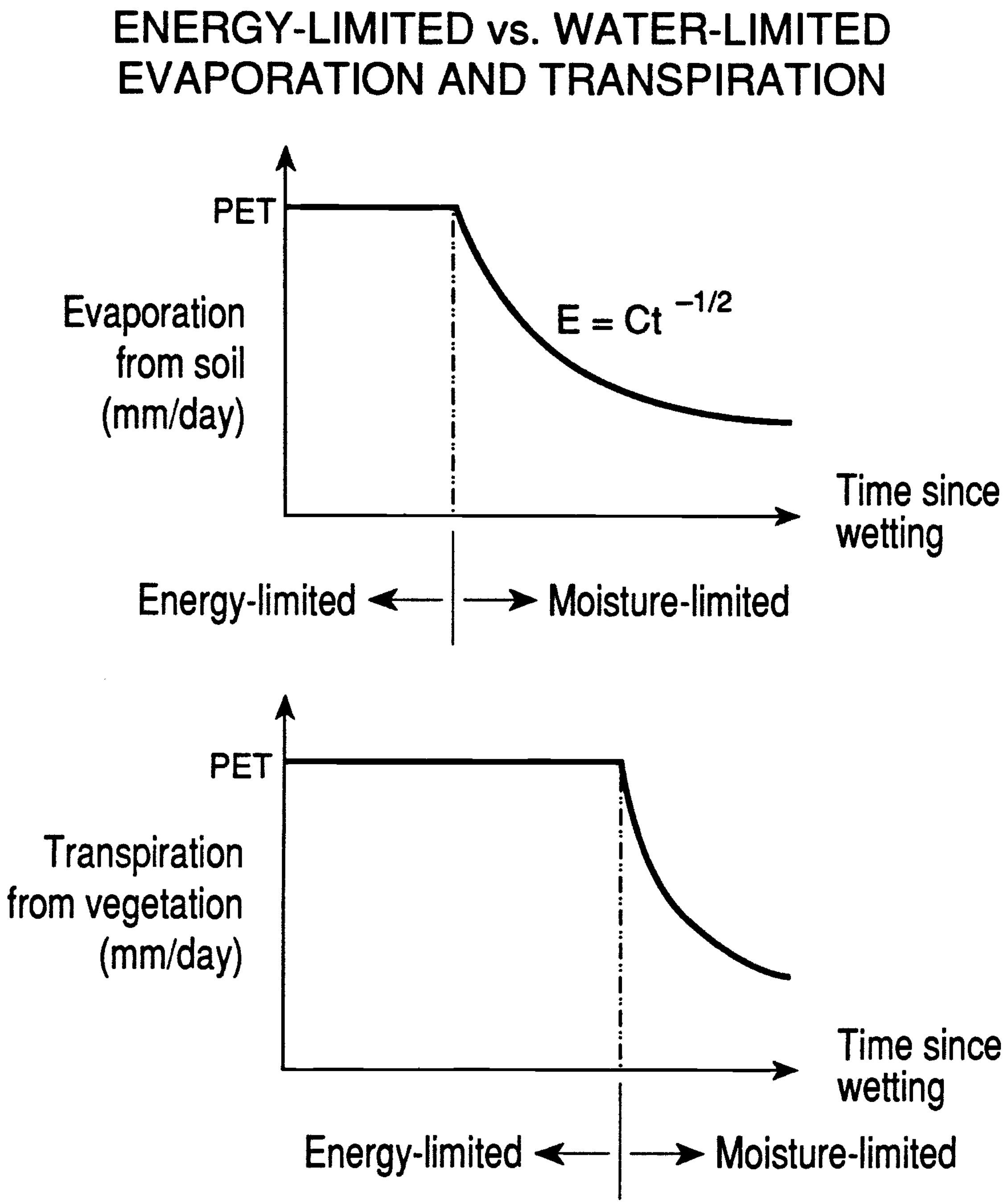

Figure 3.1. Schematic illustration of the concept of energy-limited versus water-limited evaporation and transpiration as a function of time since wetting (modified from Eagleson, 1978).

Objectives

The objectives of the analysis described in this chapter are as follows:

(1) To evaluate the factors controlling the partitioning of available energy into latent and sensible heat flux at the local scale for the FIFE experimental area by examining experimental evidence from several FIFE ground stations with different soil and vegetation conditions; and

(2) To investigate how the controlling factors for a particular ground station vary as a function of time since precipitation.

Experimental Site and Data Collection

Experiment Design and Objectives

The First ISLSCP (International Land Surface Climatology) Field Experiment (FIFE) was carried out over a 15 x 15 km predominantly prairie grassland area of central Kansas. The overall objectives of this interdisciplinary experiment were: (a) to provide an experimental data set with which to better understand the interaction of vegetated land surfaces with the atmosphere, and (b) to determine the extent to which satellite remote sensing data can be used to observe and quantify this interaction. A detailed description of the experiment plan is given by Sellers and Hall (1987), an overview of the experiment implementation is given by Sellers et al. (1988), and a summary of preliminary analysis is given by Sellers et al. (1990).

The original experiment consisted of three major 10-15 day campaigns, called Intensive Field Campaigns (IFCs), throughout the grassland growing season from May through August 1987. The intention was to obtain measurements during three major stages of vegetation development: "Greening up" (IFC 1), "Peak Greenness" (IFC2), and "Dry Down" (IFC 3). A fourth IFC was carried out in early October during a period of vegetation senescence. After preliminary analysis of the 1987 data set, another measurement campaign was planned and carried out from July 24 through August 12, 1989. All of the campaigns consisted of simultaneous coordinated ground, aircraft, and satellite measurements. In addition to collecting radiometric data at various scales, surface energy flux measurements were made at a number of ground-based sites; detailed measurements of soil and vegetation characteristics were made at many of these sites. Additionally, ground- and aircraft-based measurements were made of atmospheric boundary layer characteristics, including estimates of fluxes from aircraft-based instruments. An illustration of the field experiment activities for one day is shown in Figure 3.2 (reproduced from Sellers et al. (1988)).

Site Description

The experimental site is a 15 x 15 km area located near Manhattan, Kansas (39°9'N, 96°40'W) near the northeastern extent of the Flint Hills region. Approximately the northwestern quarter of the experimental area is occupied by the Konza Prairie Long Term Ecological Reserve (LTER). The tallgrass prairie is composed primarily of big bluestem (*Andropogon geradi*), little bluestem (*Andropogon*

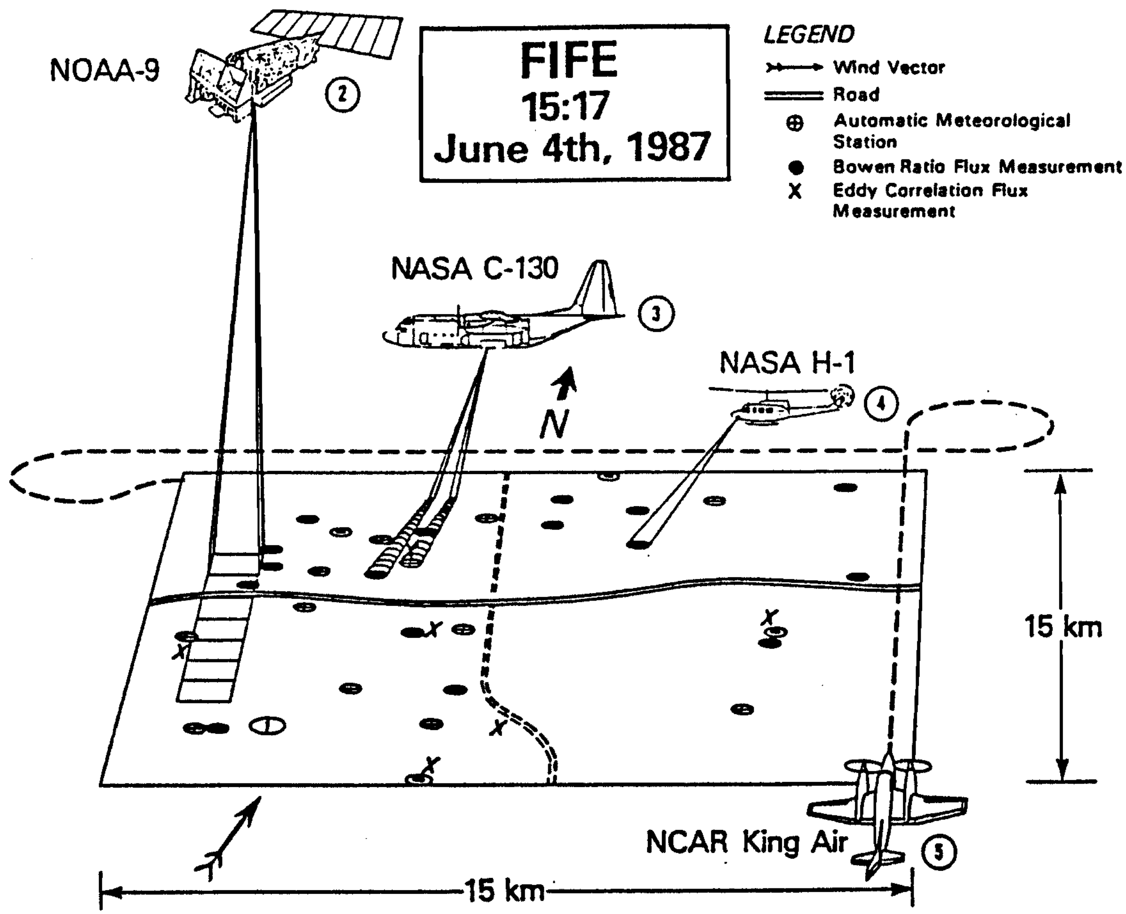

Figure 3.2. Illustration of the simultaneous acquisition of ground-based, aircraft-based, and satellite-based data for a typical day during a FIFE Intensive Field Campaign (from Sellers et al., 1988).

scoparious), and Indian grass (*Sorghastrum nutans*), but 36 other species have also been identified in a detailed vegetation study of the area (The Tallgrass Laboratory, 1984). The LTER has been used for many years for controlled studies to determine the effect of management practices on grassland productivity, such as burning dead biomass from previous growth at various intervals. In limited areas on the LTER, buffalo are being reintroduced and are allowed to graze, but these areas were not intensive grazed during the 1987 and 1989 campaigns. The rest of the experimental site is also predominantly prairie grassland which undergoes varying management practices with regard to burning and grazing. Some areas of the experimental site are intensively grazed by cattle, and there is one significant agricultural area in the southeastern quadrant of the experimental site that is roughly 3 x 3 km. Additionally, bands of woody vegetation exist along the drainage areas. The natural variations and anthropogenic activities over the site give rise to significant variations in vegetation cover over the experimental area. To quantify these variations, the LAI values measured at all the surface sites in early and mid-August of 1987 are provided in Table 3.1.

The topography of the experimental site consists mainly of rolling hills, with total relief of about 50 meters. The textural classifications of the near-surface soil layers range from silty loams to silty clay loams. Approximately six different soil series were identified in the special soil survey done in conjunction with the FIFE Experiment (Soil Conservation Survey, 1987). There is considerable variability in the hydraulic characteristics of these soils, most likely due to significant variations in the

Table 3.1. Values of LAI for FIFE Sites--Average of Measurements Made in Early August and Mid-August.

Site #	LAI 8/87
1	0.88
2	0.32
3	0.52
5	0.61
6	0.67
7	0.99
8	0.76
9	0.66
10	1.62
11 (16,18)	1.08
12	0.78
13	0.79
14	0.98
22	0.64
24	1.00
20	0.92
26	0.29
23	0.72
25	0.42
27	0.26
28	0.85
29	0.41
30	0.29
31	0.87
34	0.90
36	0.26
38	0.40
40	0.53
42	1.08
44	0.43

clay content. Because of the interplay between topography and the processes of soil development in the area, there is a strong correlation between soil type and elevation. Soil depth varies considerably over spatial scales on the order of tens of meters and is also correlated with elevation and topography. The mean annual precipitation for the area is 750 mm; the climate is temperate midcontinental with warm, moist summers and cool, dry summers.

Ground Measurements Used in This Analysis

Flux Measurements. The locations of the 18 ground-based surface flux measurements and 16 automatic meteorological stations in operation during most of the 1987 campaigns are shown in the plan view diagram of the FIFE site illustrated in Figure 3.3. A major consideration in the experimental design was that the locations of the surface flux stations be representative of the characteristics of the entire site. Thus, the sites were distributed among flat hilltops, flat valleys, sloping hillslopes of varying aspects, burned, and unburned areas roughly in proportion to the occurrence of those conditions over the entire site (Sellers et al., 1990). The surface flux stations were set up and implemented by approximately five different investigator teams; either the Bowen ratio or eddy correlation techniques were used for estimating the latent and sensible heat fluxes at each of the ground-based flux sites. Several participants studied the possible effects of differences in instrumentation on the fluxes measured at various sites (Shuttleworth et al., 1989; Fritchen and Qian, 1990; Nie and Kanamasu, 1990). It was necessary to locate some of the stations on

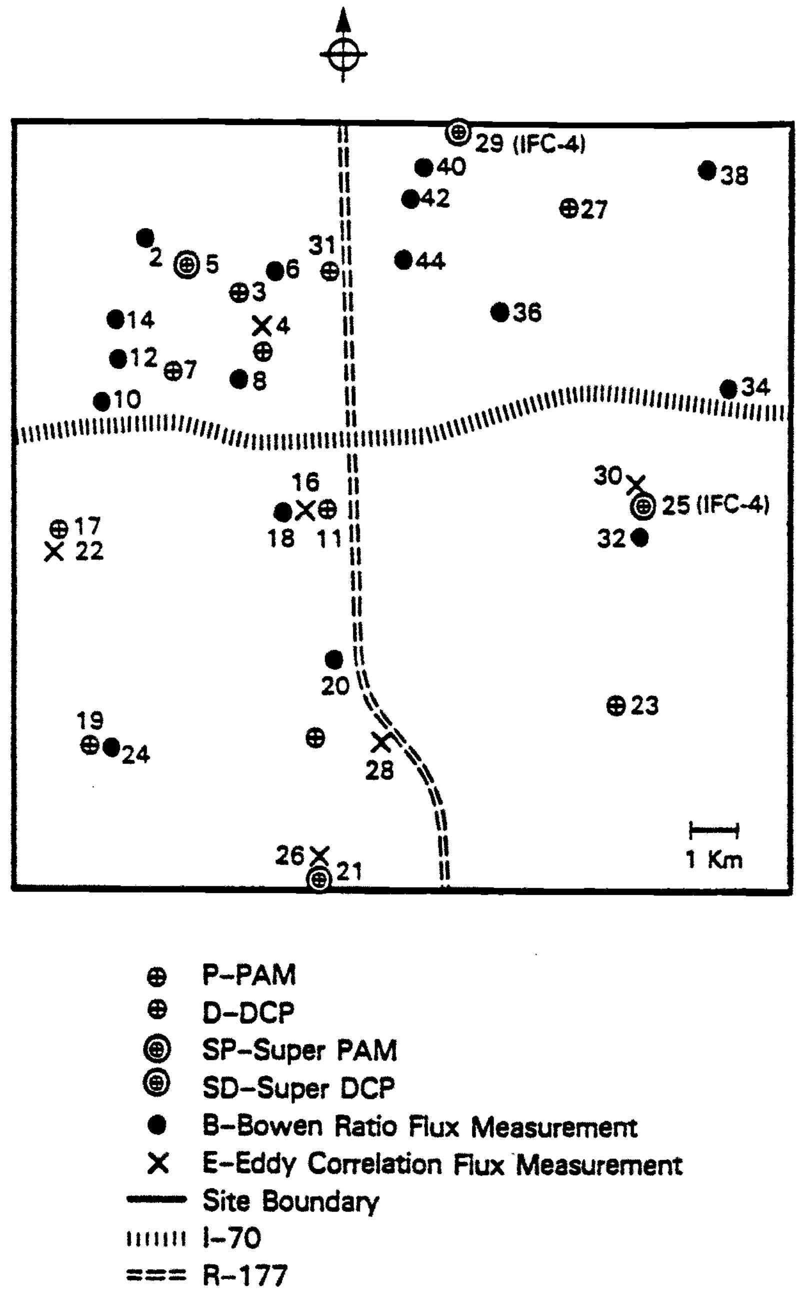

Figure 3.3. Plan view of the FIFE site showing the locations of the ground-based flux stations and automated meteorological sites (PAM and Super PAM stations) for 1987 Intensive Field Campaigns. Flux sites are numbered with even numbers; met stations are numbered with odd numbers (from FIFE 1987 Experiment Plan).

sloping surfaces, requiring the use of the flux estimation techniques over some areas in which their applicability is not yet firmly established. The locations of the flux stations and meteorological stations for the 1989 campaign are shown in Figure 3.4. For both campaigns, there were no flux stations in either the woody vegetation or agricultural areas.

Soil Moisture Measurements. For almost all days during the IFCs and for many days in between the IFCs as well, gravimetric soil moisture measurements were made at all of the meteorological and flux station sites. Five soil samples at each of two depths (0-5cm and 5-10cm) were collected at random locations just adjacent to the anticipated fetch area of the flux stations for each site each day. The five estimates of soil moisture content by weight were averaged to obtain the daily soil moisture estimate for each depth. The samples were usually acquired between 9 a.m. and 1 p.m. local time (Central Daylight Time). Neutron probe measurements were made at the meteorological stations and flux sites in order to derive estimates of volumetric soil moisture at depths from 20-100 cm. These measurements were made at approximately 6-8 day intervals for most of the ground sites.

Vegetation Characteristics. For each ground site, samples were collected approximately once/week from five 0.1 m^2 areas near the meteorological or flux stations. Fresh live-standing, dead-standing, and dead biomass was collected from those areas. Grass and non-grass vegetation types were separated for processing; this included running the samples through a leaf area meter and drying the samples. Fresh weights, dry weights, and leaf area index were reported for all five samples for

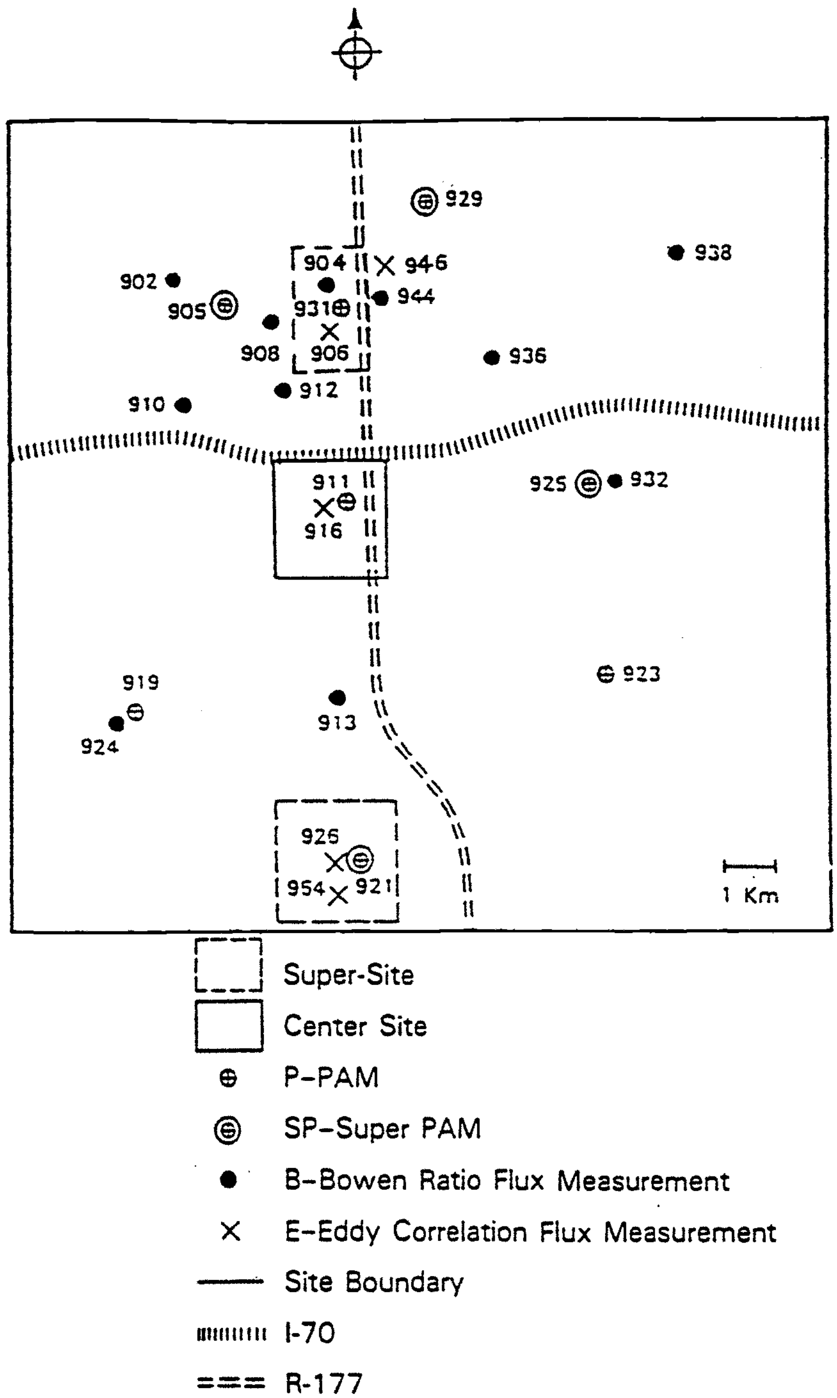

Figure 3.4. Plan view of the FIFE site showing the locations of the ground-based flux stations and automated meteorological sites (PAM and Super PAM stations) for 1989 Intensive Field Campaigns. Flux sites are numbered with even numbers; met stations are numbered with odd numbers (from FIFE 1989 Experiment Plan).

each site on each date, separated by grass and non-grass. The average of the five samples for each date is utilized in this analysis. As is common with measurements of this type, the standard deviation in the five samples for a given site on a given day was often 20-50% of the average value. Before the destructive sampling took place, canopy heights were also recorded for each of the sample areas.

Analysis of Factors Controlling Energy Partitioning at Single Sites

Throughout this analysis, the partitioning of available energy into sensible and latent heat flux will be quantified by the observed evaporative fraction, f_E, defined as:

$$EF = LE/(LE + H). \tag{3.1}$$

As shown in the previous chapter (Equation 2.6), the evaporative fraction provides the same information as the Bowen ratio, β, and they are related by the expression:

$$EF = 1/(1 + \beta). \tag{3.2}$$

A preliminary evaluation of the variation in energy partition at surface flux sites for the 1987 FIFE data was performed by Shuttleworth et al. (1989) with data from relatively clear days in each IFC. One of the most encouraging conclusions from that analysis was that, for clear days, the midday evaporative fraction for a given site was usually relatively constant and was well-correlated with the all-day evaporative fraction. From the standpoint of eventually using remotely sensed data to estimate surface fluxes, this was a rather positive conclusion. However, Shuttleworth et al. (1989) were unable to find significant correlations between the evaporative fraction for different sites and the following surface parameters (chosen as those that might be relatively easily estimated with remotely sensed data): leaf area index, soil moisture (0-5 cm), and fraction of green vegetation. For their analysis, they used ground measurements of these parameters. The results for their analysis of data from August 15, 1987 are shown in Figure 3.5.

Based on the analysis described above, we can infer that evaluating the behavior of all sites on isolated days is not likely to be very helpful in evaluating the factors controlling the fluxes. Different portions of the experimental area received varying amounts of precipitation in the days prior to August 15, 1987. Therefore, it is likely that evapotranspiration in some areas of the site that day was energy-limited and, in some areas, it was moisture-limited. In the analysis to be described below, the behavior of two different ground sites was evaluated as a function of time since wetting to determine which soil and vegetation characteristics appear to control the evaporative fraction as a function of time.

The two ground sites selected were Sites 18 and 26. Site 18 was situated on a ridgetop location which had been burned the previous year and was not used for grazing. Site 26 was situated on a ridgetop location in an area of rather intense grazing. The LAI values for these sites during IFC 1 (late May-early June) and IFC 2 (mid-August), extracted from the FIFE Information System, are summarized in Table 3.2. The raw data for LAI samples from Site 18 in August show higher than

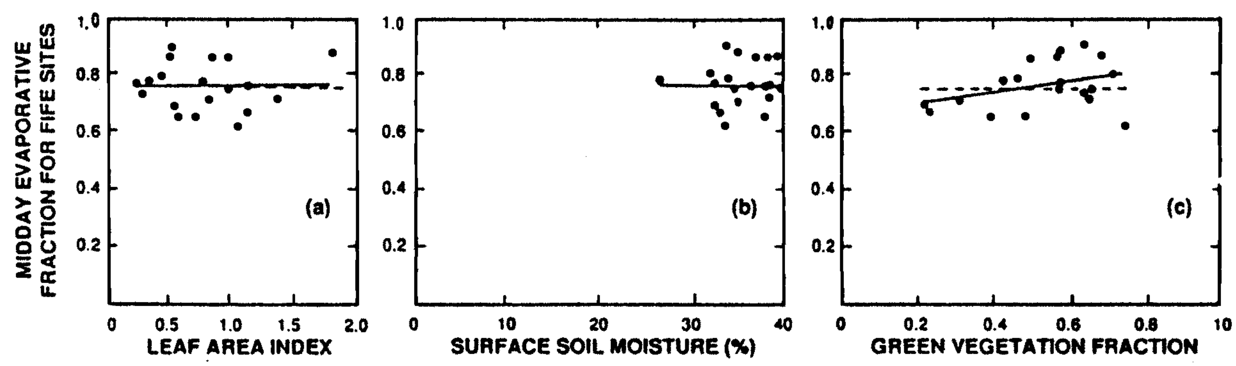

Figure 3.5. The proportion of energy used for evapotranspiration around midday on 15 August 1987 at 20 FIFE surface flux sites plotted against the equivalent site specific values of (a) leaf area index, (b) surface soil moisture, and (c) green vegetation fraction (from Shuttleworth et al., 1990).

Table 3.2. LAI Values at Sites 18 and 26 for IFC1 and IFC3.

Site	LAI - Average of Late May and Early June	LAI - Average of Early and Mid-August
18	1.63	1.08
26	0.78	0.29

average variability, and there is some reason to suspect that the value reported in Table 3.2 for that site in August is somewhat low. Although neither of these sites were located on the Konza LTER, they were selected because they were each representative of two different vegetation conditions which were prevalent over the experimental site. Site 18 represents an area which is well managed with respect to burning dead biomass from previous years. It has a moderate to high amount of vegetation cover compared to most other ground sites. Site 26 represents an area that is rather intensively grazed; it has a lower amount of vegetation cover than most other sites in the experimental area. The flux measurements at Site 18 were made using the Bowen ratio technique by scientists from the University of Nebraska. The flux measurements at Site 26 were made using eddy correlation techniques by a team of scientists from the Institute of Hydrology in Wallingford, England.

Analysis of Fluxes in Early Summer

During the first IFC in 1987, carried out in late May and early June, fairly extensive precipitation occurred over most of the experimental site on Days 147 and 148 (May 28-29). The evaporative fraction, computed from the flux station data, and ratio of soil moisture by weight to saturated soil moisture (θ/θ_{sat} for the 0-5 cm soil layer) are plotted for Sites 18 and 26 in Figures 3.6a and 3.6b, respectively. The data are for the time period just after the extensive precipitation event, from Day 149 (May 30) through Day 157 (June 6). A few small precipitation events occurred at Site 26 on days 149 and 152, but the general trend in surface soil moisture for both

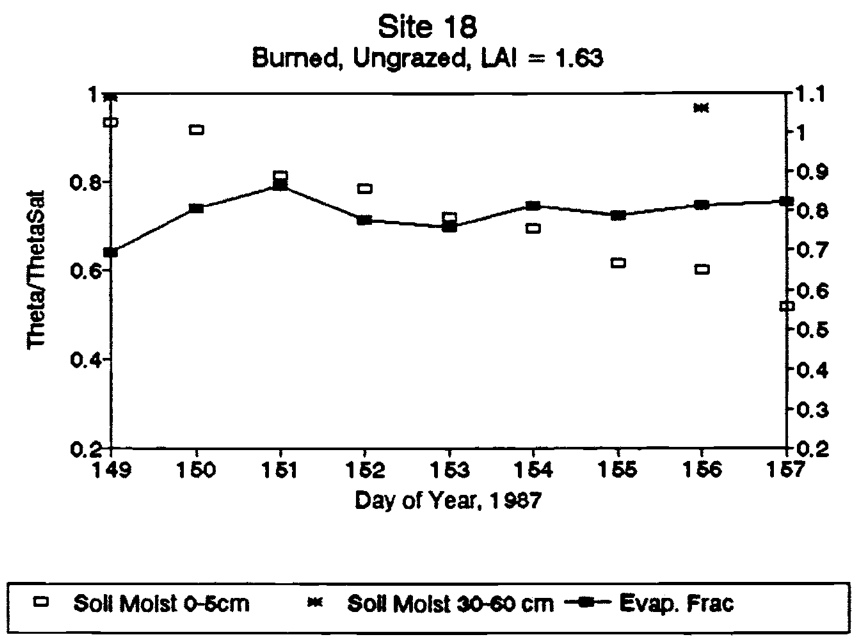

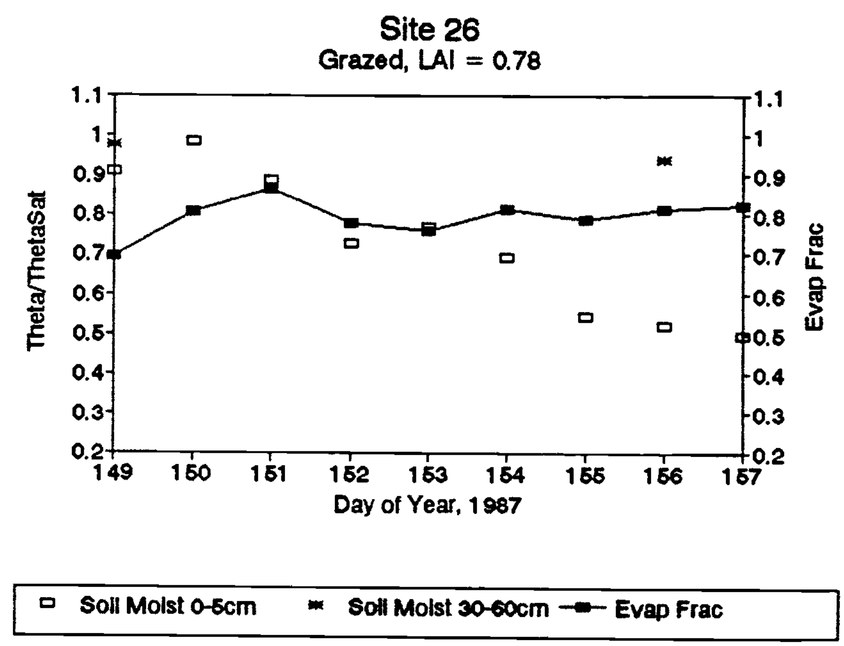

Figure 3.6a. (Top) Evaporative fraction (solid squares), θ/θ_s in the 0-5cm deep soil layer (open squares), and θ/θ_s averaged over 20-60 cm depth (*) for Site 18, Day 149 (May 30) - Day 157 (June 6), 1987.

Figure 3.6b. (Bottom) Evaporative fraction (solid squares), θ/θ_s in the 0-5cm deep soil layer (open squares), and θ/θ_s averaged over 20-60 cm depth (*) for Site 26, Day 149 (May 30) - Day 157 (June 6), 1987.

sites is an approximately 30% decrease over that time period. However, over that same time period, the evaporative fraction remained nearly constant and fairly high (approximately 0.8 for both sites). Thus, the data show that, for sites with either sparse and moderately vegetation cover, the evaporative fraction remained very high, although the surface soil moisture decreased substantially over that time period.

Soil moisture profile data from the neutron probe measurements show that the root-zone soil moisture was near saturation during this time period and remained so for several days thereafter. The profile data for Sites 18 and 26 are shown in Figures 3.7a and 3.7b, respectively. The near-surface gravimetric soil measurements taken at depths 0-5 cm and 5-10 cm were converted to volumetric moisture content using the bulk density values measured at the individual field sites; these data are also shown in Figures 3.7a and 3.7b.

The data shown in Figures 3.6 and 3.7 suggest the following for sites with either moderate or sparse vegetation cover (and plentiful moisture in the root-zone soil profile): soil evaporation contributes to the total evaporative flux when moisture is available in the surface layer (as evidenced by the rapid decrease in surface soil moisture with time), but soil moisture in the surface layer does not limit the total evaporative flux when it becomes small (as evidenced by the fact that the evaporative fraction remained high for both sites while the surface soil moisture decreased significantly). It can be inferred from these data that the sum of the rate of soil evaporation and vegetation transpiration remained invariant over this time period, although these data suggest that the contribution by these different processes to the

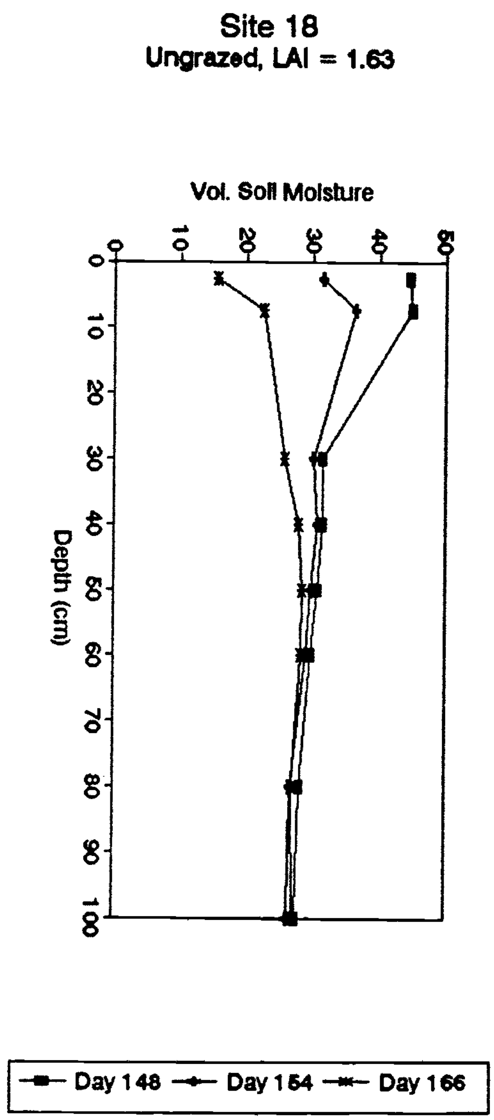

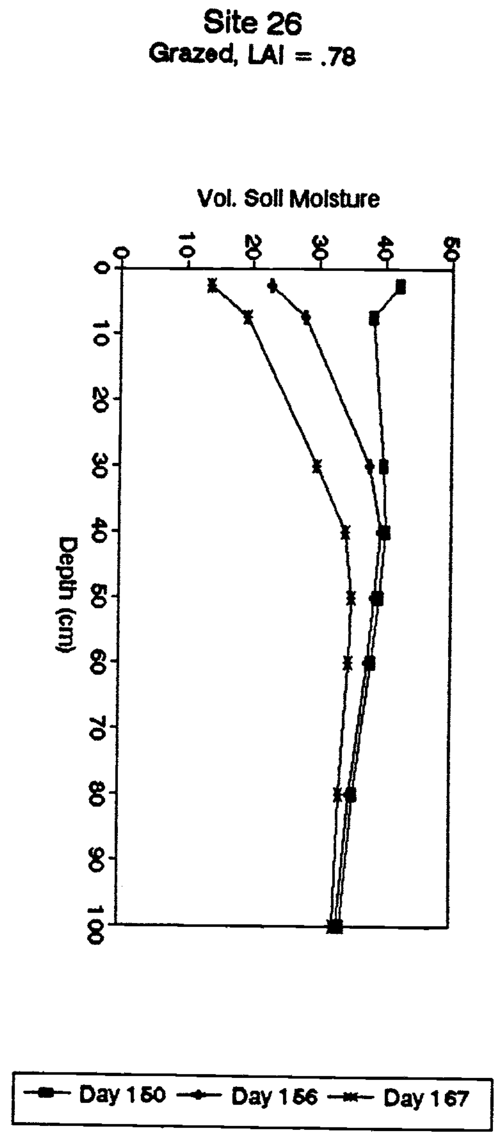

Figure 3.7a. (Left) Soil moisture profiles for Site 18 on three separate days. Upper two points are from gravimetric soil moisture samples converted to volumetric soil moisture with measured values for bulk density. Values for depths 20-100 cm are from measurements with a neutron probe.

Figure 3.7b. (Right) Soil moisture profiles for Site 26 on three separate days. Upper two points are from gravimetric soil moisture samples converted to volumetric soil moisture with measured values for bulk density. Values for depths 20-100 cm are from measurements with a neutron probe.

total evaporative flux changed from the beginning to the end of this time period.

A consideration of the values of average midday vapor pressure deficit measured at 2m above the surface at the flux sites helps to provide qualitative evidence for the mechanism by which the sum of evaporation and transpiration remained invariant from day to day over this time period. For Site 26, the average midday vapor pressure deficit 2 meters above the canopy was 7 mbars on Day 149, 19 mbars on Day 156, and 33 mbars on Day 166. For those days on which the surface soil moisture is relatively dry, the air in the inter-canopy and above-canopy airspace is warmer and drier, as evidenced by higher vapor pressure deficits on those days. As the soil surface dries, the increased vapor pressure deficit provides more atmospheric demand for the moisture available by vegetation transpiration. Thus, when the vegetation root zone is well-supplied with moisture, the microclimate feedbacks force the transpiration rate from the vegetation to increase as the evaporation from the soil decreases.

Correlation Between Soil Moisture and Vapor Pressure Deficit

To further investigate the relationship between soil moisture and above-canopy vapor pressure deficit for partial canopies, the gravimetric soil moisture in the 0-5cm layer is plotted versus average midday vapor pressure deficit for Site 26 in Figures 3.8a and 3.8b. In Figure 3.8a, the data from all days during IFCs 1, 2, and 3 are included. Because high values for windspeed on a given day would tend to mitigate the surface effects on vapor pressure deficit, only the data for days with

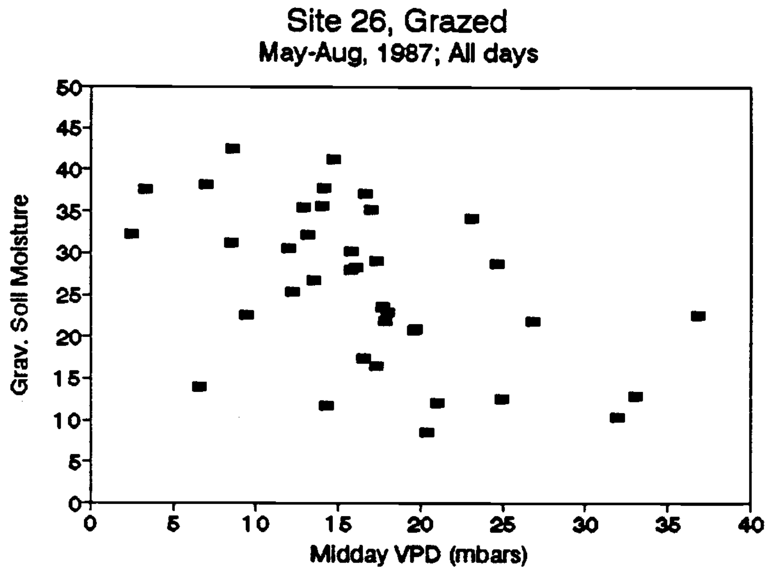

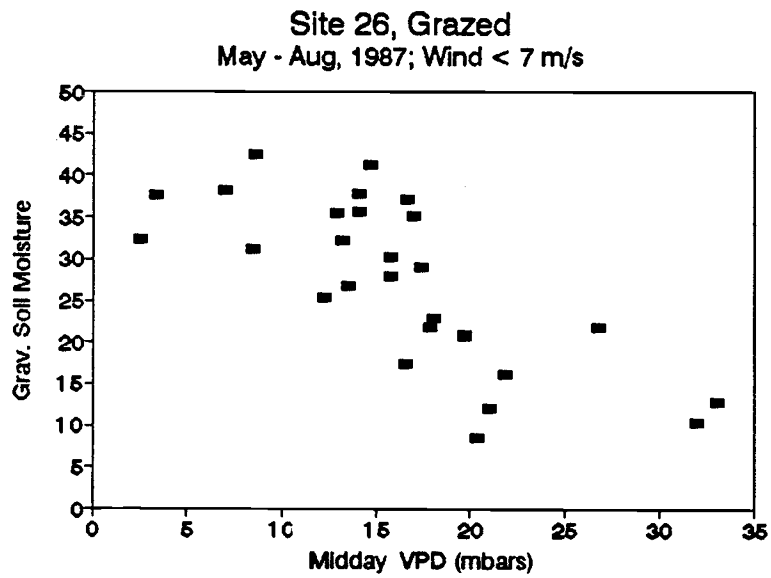

Figure 3.8a. Gravimetric soil moisture for the 0-5cm depth vs. average midday values of vapor pressure deficit for Site 26. Data shown include all days in IFCs 1,2,3 (May-August 1987).

Figure 3.8b. Gravimetric soil moisture for the 0-5cm depth vs. average midday values of vapor pressure deficit for Site 26. Data shown are for those days with average midday windspeed values < 7 m/s.

windspeeds less than 7 ms^{-1} are shown in Figure 3.8b. There appears to be a correlation between surface soil moisture and near-surface vapor pressure deficit on days with low and moderate windspeeds. The purpose in presenting these data is not to derive a quantitative relationship between the two variables, but to simply provide experimental evidence of the type of microclimate feedbacks that can influence evaporative fluxes over surfaces with partial vegetation cover. These feedbacks add additional complexity to the problem of ascertaining the factors controlling evaporative fluxes for these types of surfaces.

Analysis of Fluxes in Late Summer

During the third IFC in 1987, carried out in August, the limited data available from neutron probe measurements indicate that root-zone soil moisture at most sites was significantly smaller than it was in IFC 1. The relationship between evaporative fraction and surface soil moisture was evaluated as a function of time since wetting for several sites during this time period. Data from Site 26 were not available for the first half of IFC 3; therefore, for this comparison, data from Site 30 were used instead. Site 30 was also extensively grazed, and values of leaf area index were very similar to those at Site 26. The surface energy fluxes at Site 30 were also measured with eddy correlation instrumentation.

The evaporative fraction and fractional surface soil moisture data for Day 220 (August 8, 1987) through Day 234 (August 21, 1997) are shown in Figures 3.9a and 3.9b for Sites 18 and 30, respectively. On Day 224, a very intense rainstorm occurred

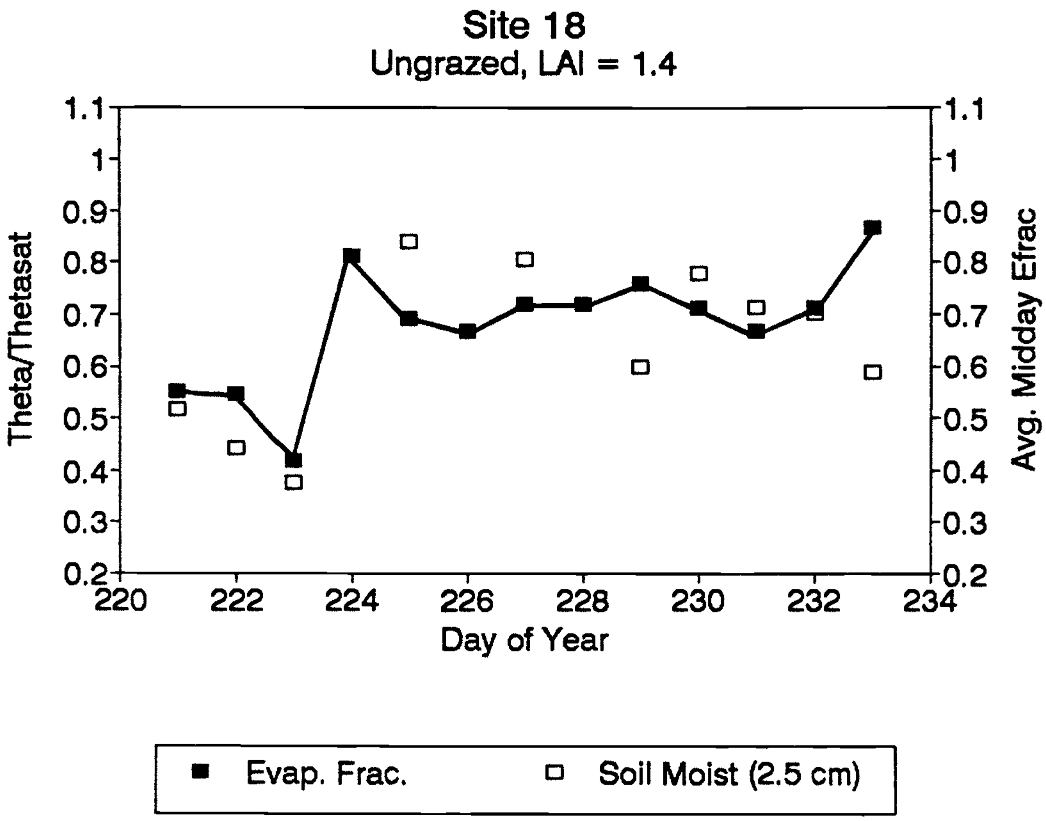

Figure 3.9a. Evaporative fraction (solid squares), θ/θ_s in the 0-5cm deep soil layer (open squares), and $\theta/\theta s$ averaged over 20-60 cm depth (*) for Site 18, Day 220 (August 8) - Day 233 (August 21, 1987).

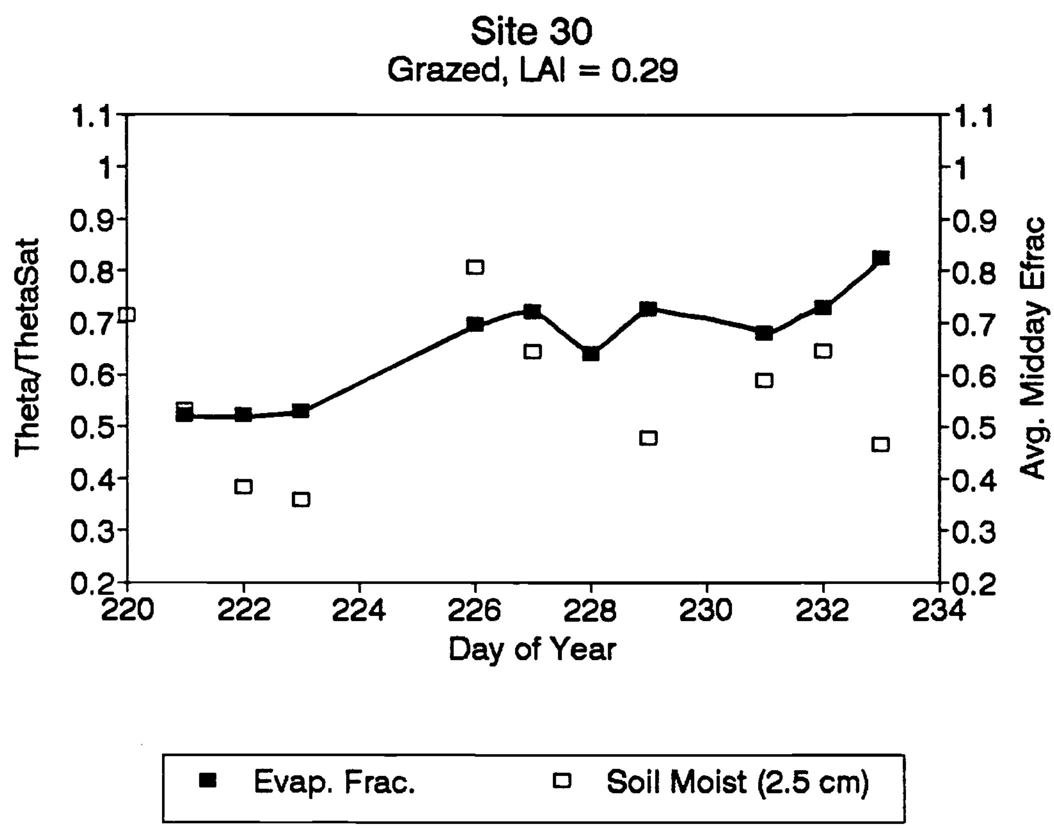

Figure 3.9b. Evaporative fraction (solid squares), θ/θ_s in the 0-5cm deep soil layer (open squares), and $\theta/\theta s$ averaged over 20-60 cm depth (*) for Site 30, Day 220 (August 8) - Day 233 (August 21, 1987).

over most of the experimental site. Before the rainfall event, under conditions of relatively low soil moisture in both the surface layer and the root zone, the evaporative fraction at both stations was limited by available moisture. The data in Figure 3.9a-b suggest that, for a period of time after the rainfall event, the evaporative fraction tracks closely with the surface soil moisture. The most likely explanation for this is that the root-zone moisture was too low for vegetation transpiration to dominate the total evaporative flux during periods of low surface soil moisture. Thus, the surface soil moisture does appear to have a controlling effect on the total evaporative fraction when viewed as a function of time under these conditions.

Aggregation of Sites With Similar Characteristics

In order to further evaluate the concept that different surface parameters control the evaporative fraction during different stages of drying (i.e., as a function of time since wetting), it is useful to evaluate the behavior of more than two sites. The most ideal conditions for making that evaluation would require a rainfall event which covered the entire site and saturated the surface and root zone for all the ground sites, followed by many days of a gradual dry-down period over the whole area. Unfortunately, during the IFCs for 1987, such conditions did not exist. There were rainfall events which covered the whole experimental area, but they were not followed by sufficiently long periods of no precipitation at most sites. In addition, there were many closely spaced small events which caused wetting at some ground sites but not at others.

During the IFC in 1989, conditions were somewhat more favorable to observe a dry-down period for all sites in the experimental area. In order to further evaluate the factors controlling the evaporative fluxes under different conditions, it is useful to look at the evaporative fraction as a function of time since precipitation for many sites, grouped by different possible controlling surface parameters. In Figures 3.10a and 3.10b, the average evaporative fraction is plotted as a function of time since wetting, with the sites grouped according to vegetation and soil characteristics, respectively. For the data shown in Figure 3.10a, the 10 flux stations reporting data for the 1989 IFC were grouped by grazing practices. In 1989, there were three sites that were heavily grazed and seven sites that were not grazed. The grazed sites had significantly lower vegetation cover than the ungrazed sites. For the results shown in Figure 3.10b, the sites were grouped into two categories according to soil type. The five sites with silt loam soil textures were grouped into the first category, and the five sites with silty clay loam soil textures were grouped into the second category. The error bars shown in both Figures 3.10a and 3.10b represent the standard deviation of the evaporative fraction values of the sites that were averaged in that group.

The results shown in Figure 3.10a suggest that, under the post-rainfall conditions of the 1989 IFC, the sites with less vegetation cover (grazed sites) had a larger mean value of evaporative fraction than sites with more vegetation cover. The

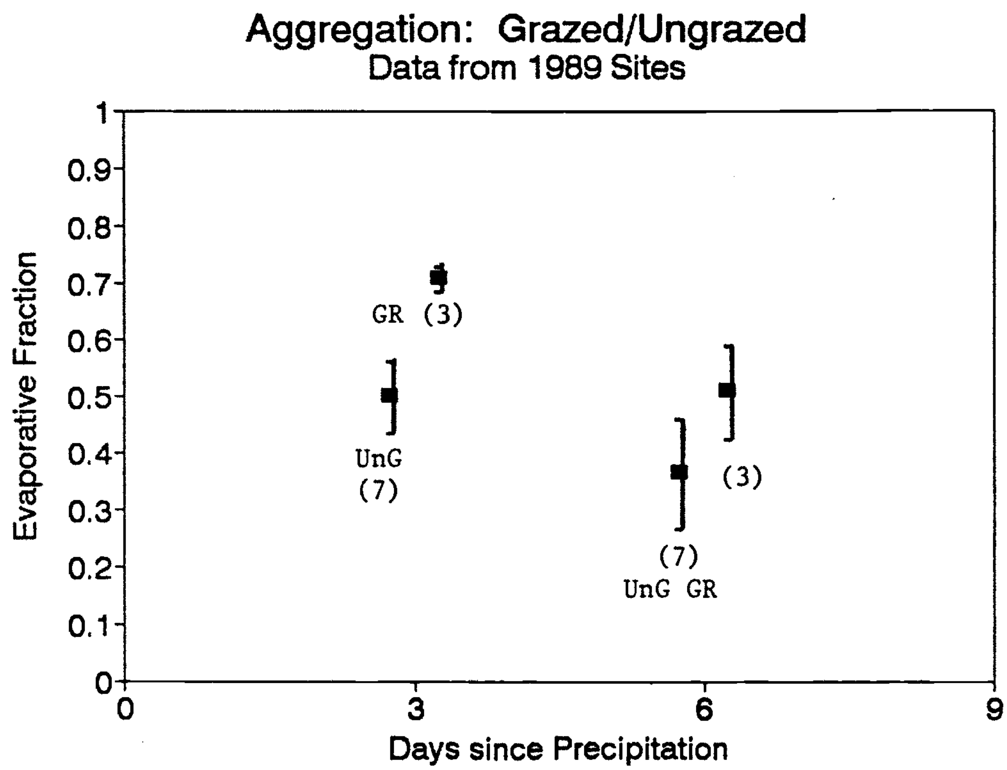

UnG = Average for Ungrazed Sites, 7 sites
G = Average for Grazed Sites, 3 sites

Figure 3.10a. Average evaporative fraction as a function of time since precipitation for the ground-based flux sites, aggregated by grazing practices.

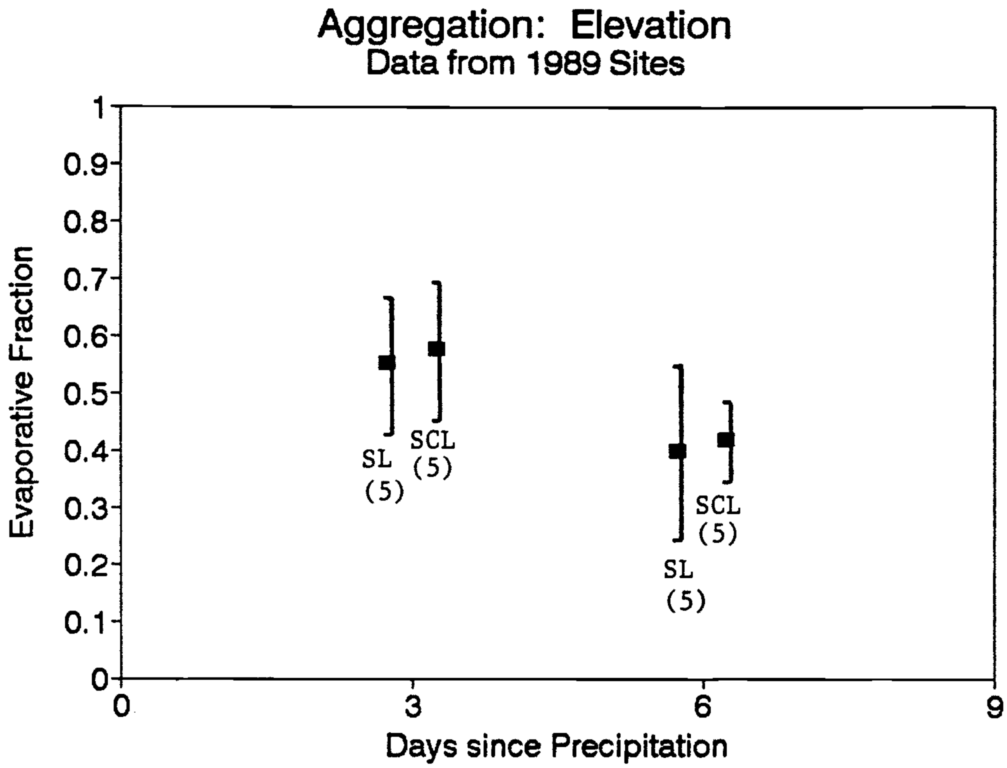

SL = Silt Loam sites, <420 m elevation
SCL = Silt Clay Loam sites, > 420 m elevation

Figure 3.10b. Average evaporative fraction as a function of time since precipitation for the ground-based flux sites, aggregated by elevation. Elevation is a surrogate variable for soil type. Soils at sites with elevation > 420 m (5 sites) have silt loam texture and sites at < 420 m (5 sites) have silty clay loam textures.

results shown in Figure 3.10b suggest that the soil texture did not have a significant influence on evaporative fraction under these conditions. The evaluation of a few individual sites with 1987 data did not suggest that the amount of vegetation cover had a significant effect on the evaporative fraction. These results underscore the other evidence presented in this chapter that the factors controlling the total evaporative fluxes for surfaces with partial vegetation cover are difficult to quantify for general conditions.

Summary and Conclusions

In this chapter, data from the First ISLSCP Field Experiment (FIFE) were examined to evaluate the factors controlling the partitioning of available energy into latent and sensible heat flux under various field conditions, as quantified by the evaporative fraction measured at ground-based flux stations. The primary conclusion to be drawn from the data presented here is that the factors controlling the partitioning of available energy for surfaces with partial vegetation cover (such as portions of the FIFE experimental area) are very difficult to quantify for general conditions. Factors such as vegetation cover, surface soil moisture, root-zone soil moisture, and soil type appeared to influence the evaporative fraction to varying degrees under different field conditions and time since wetting. The factors influencing the evaporative fraction for particular sites appeared to be dynamic and quite dependent on the moisture status of the entire soil profile.

The implications of this analysis for the estimation of energy balance components with remotely sensed data are that it is not a simple task to develop process-based models which can adequately capture the dynamics of complex, interactive processes with a few remotely sensed variables. In order to obtain an estimate of the partitioning of the sensible and latent heat flux over partially vegetated surface with remotely sensed data, a relatively simple energy-balance approach will be investigated in subsequent chapters.

CHAPTER 4

THE ESTIMATION OF SOIL HEAT FLUX AND SENSIBLE HEAT FLUX OVER FIFE GROUND STATIONS WITH REMOTELY SENSED DATA

Introduction

In this chapter, the feasibility of using remotely sensed data from helicopter- and satellite-based instruments to estimate the surface soil heat flux and sensible heat flux is investigated. The fluxes are estimated with a combination of ground and remotely sensed data at scales compatible with the fetch areas of the individual ground-based flux stations. The fluxes computed with a combination of ground and remotely sensed data are compared with those estimated at the ground stations. As discussed in Chapter 1, the surface fluxes for areas with partial vegetation cover are controlled by many factors and complex interactive processes which cannot be determined by instantaneous remotely sensed observations at a single view angle and time. Rather, the focus of this research was to utilize the unique opportunity that exists in the wealth of ground data available for the FIFE experiment to determine how to best utilize remotely sensed data for the estimation of surface fluxes and to identify the best algorithm to use to create a spatially distributed map of surface fluxes for the entire site. The potential contribution of this type of spatially distributed map of surface fluxes is to provide a set of spatially distributed boundary conditions for coupled models of the interactions between surface fluxes and the atmospheric boundary layer.

In particular, this chapter focuses on the estimation of the soil heat flux and the sensible heat flux component of the surface energy balance. The latent heat flux is computed as a residual quantity after estimating the other three components of the surface energy balance. The estimation of net radiation over a surface as topographically complex as the FIFE experimental site is a separate topic of research. Dubayah et al. (1990) produced a map of net solar radiation for the FIFE site using the Landsat TM data for August 15, 1987. This map will be adjusted for net long-wave radiation and used as input for computing the latent heat flux over the site in the next chapter. Consequently, the topic of the estimation of net radiation will not be addressed here.

Approach

In order to evaluate the estimation of surface energy-balance components with remotely sensed data over the FIFE site with remotely sensed data acquired at various spatial scales, the following analyses are presented:

(1) Remotely sensed reflectances and temperatures obtained over several FIFE ground stations with a helicopter-based sensor are compared with simultaneous measurements with a ground-based sensor;

(2) Various techniques for estimating soil heat flux and sensible heat flux from the helicopter-based remotely sensed data are evaluated by comparison with fluxes measured at the ground-

based stations with Bowen ratio and eddy correlation techniques;

(3) Extracts of data from a Landsat TM scene are corrected for atmospheric effects and compared with reflectances and temperatures acquired simultaneously with helicopter- and ground-based instruments; and

(4) Various techniques for estimating soil heat flux and sensible heat flux from the satellite-based remote sensing data are evaluated by comparing the fluxes estimated with the satellite data to the fluxes measured at the ground-based stations with Bowen ratio and eddy correlation techniques.

Experimental Data

All of the analysis in this chapter relates to the use of different types of traditional ground-based data and remote sensing data acquired with different sensors during the FIFE campaigns in 1987. The ground-based data relating to soil moisture, leaf area index, and canopy height used in the analysis were acquired by FIFE staff personnel at Kansas State University and were described in Chapter 3. The instrumentation utilized for various ground-based data from the surface flux stations used in this analysis is summarized in Table 4.1. Detailed documentation describing the data acquired at most of the ground-based flux stations was provided by each lead investigator and is available in the FIFE Information System. The

Table 4.1. Ground Flux Stations Used in Analysis of Fluxes with Helicopter-based Remote Sensing Data (BR = Bowen ration apparatus; EC = Eddy correlation apparatus).

Site #	Team Institution (Lead Investigator)
2	BR - Kansas State University (Kanemasu)
8	" " " "
10	" " " "
20	BR - University of Washington (Fritschen)
36	" " " "
40	" " " "
42	" " " "
44	" " " "
16	EC - University of Nebraska (Verma)
	BR - " " " *
26	EC - Institute of Hydrology (Stewart, Shuttleworth)
24	BR - GSFC/ARS/University of Delaware (Kustas)
30	EC - GSFC/ARS/University of Delaware (Field)
28	EC - USGS (Weaver)

* BR data reported in FIFE Data Information System as Site 18 (co-located with 16), but BR data are used in this analysis and reported in Figures as 16.

remotely sensed data used in this analysis will be briefly summarized below. More detailed documentation about each of the remotely sensed data types described below is also available in the FIFE Information System.

Ground-Based Remote Sensing Data

Ground-based measurements of canopy reflectance and temperature were made at some of the FIFE flux stations by a team from the University of Nebraska led by Dr. Blaine Blad. The following description of the data acquisition and processing is a summary of the documentation provided by that team. A more detailed description of the acquisition and data processing procedures are also available from the FIFE Information System.

The measurements were made with a Barnes Model 12-1000 Modular Multiband Radiometer (MMR) mounted on a portable mast 3.4m above the soil surface. With the 15° field of view of the instrument, the area on the ground sensed by the instrument was approximately 7.5 meters in diameter. Because one of the objectives of the measurements was to characterize the bi-directional reflectance of the surface and the view angle effects on surface temperature, the mast apparatus was designed to take measurements at several different angles for a particular target within a few minutes. These ground-based reflectance and temperature measurements were made at different times of day at different sites throughout all four Intensive Field Campaigns (IFCs) in 1987. Approximately 8-15 target areas were measured repeatedly at each of the flux stations within approximately one hour. For this analysis, only nadir-view data were used, and the reflectance and temperature results from all targets observed approximately +/- 15 minutes of the helicopter overpasses were averaged to obtain the reflectance and temperature measurements for a particular site.

The MMR measures analog voltages in response to the target radiance in 8 spectral wavebands: 0.45-0.52 μm (B1), 0.52-0.60 μm (B2), 0.63-0.69 μm (B3), 0.76-.90 μm (B4), 1.15-1.30 μm (B5), 1.55-1.75 μm (B6), 2.08-2.35 μm (B7) and 10.4-12.5 μm (B8). The voltages measured in the first 7 bands were converted to surface reflectance by utilizing voltages measured over a calibrated $BaSO_4$ reflectance plate before and after the target measurements. The voltage in the thermal band was converted to temperature using calibration coefficients determined for the instrument at the USDA-ARS U.S. Water Conservation Laboratory.

Surface temperature estimates were also corrected for downwelling reflected thermal radiation and the emissivity of the surface. The emissivity values were derived from temperature measurements made at each site with and without an aluminum tent. The temperature measurements used to calculate emissivity values were made under conditions for which incoming direct radiation was at a minimum, either at night or under completely overcast skies. The emissivity values estimated for each of the sites during the various IFCs ranged from 0.97-0.99.

Helicopter-Based Remote Sensing Data

A Barnes Model 12-1000 Modular Multiband Radiometer (MMR) was also included in a package of instruments mounted in a helicopter. The instrument package consisted of the MMR, two 35mm cameras, and a video recording system. An audio tone was recorded on the video tape to signal the times of data acquisition from the MMR. The instrument package could be positioned to view the surface at either nadir or off-nadir angles (15, 30, 45, and 60°). Only nadir-view data were used for this analysis. On days with relatively clear-sky conditions, the helicopter was flown over several sites at different times of the day. When acquiring data over a site, the helicopter hovered at an altitude of about 230m above ground level. The MMR was configured to be flown with a 1° instantaneous field of view (IFOV). The target area on the ground sensed with each MMR measurement was approximately 4 meters in diameter.

For measurements during IFCs 2, 3, and 4, the detector and chopper voltages were recorded on a data logger along with the voltages from wavebands 1-8. The detector and chopper voltages were not recorded during IFC 1, however, and thus it is not possible to calculate reflectances for the lead sulfide bands of the MMR for data acquired during IFC 1. Calibration of the MMR for absolute radiance and compensation for thermal effects was carried out by FIFE investigators at Goddard Space Flight Center and are described in detail by Markham et al. (1988). Reflectances were calculated by utilizing irradiance measurements derived from simultaneous measurements made with a second MMR mounted over a calibrated

$BaSO_4$ reflectance panel on the ground. The MMR and plate apparatus was located near the center of the field site, and the measurements were made at one-minute intervals. The temperature estimates from the MMR data were corrected by this author for the effects of reflected long-wave sky radiation and for emissivity.

Satellite-Based Remote Sensing Data

The satellite data used in the analysis below were extracted from a Landsat 5-Thematic Mapper (TM) image acquired on August 15, 1987 and provided by Earth Observation Satellite Company (EOSAT). The spectral wavebands of the TM sensor are: 0.45-0.52 μm (TM1), 0.53-0.61 μm (TM2), 0.62-0.69 μm (TM3), 0.78-.90 μm (TM4), 1.57-1.78 μm (TM5), 2.10-2.35 μm (TM7), and 10.4-12.5 μm (TM6). The ground spatial resolution of the sensor in the six wavebands in the visible and near-infrared regions of the electromagnetic spectrum is 30 meters; the ground spatial resolution of the thermal band (TM6) is 120 meters.

Until recently, Landsat TM data could be acquired from EOSAT on computer compatible tape (CCTs) in either the CCT-A format or the CCT-P format. The data on both CCT-A format tapes and CCT-P format tapes include a radiometric correction to the "raw" digital numbers. It is possible to reverse this radiometric correction (Holm et al., 1989) for applications which require knowledge of the raw digital numbers, such as absolute sensor calibration. The calibration coefficients supplied by EOSAT (Landsat TM Technical Notes, EOSAT, 1986) are intended to be used to convert the "corrected" digital numbers to apparent at-satellite radiance as a linear function of gain and offset coefficients. Additionally, on both CCT-A and CCT-P format tapes, the thermal band is resampled to provide a 30-meter spatial resolution compatible with the spatial resolution of the other bands.

On CCT-P format tapes, a geometric correction is applied to the data which are not present on the CCT-A format tapes. This geometric correction is a cubic convolution procedure which is applied to the raw data to smooth the blocky appearance of the resampled data. The original spectral response of each 120-meter pixel is not saved in this procedure, and the smoothing operation cannot be reversed. Hence, it is preferable to use the CCT-A tapes for applications which require the best possible radiometric integrity of the data in the thermal band.

However, all of the Landsat TM data acquired over the FIFE site in 1987, 1988, and 1989 are available only in CCT-P format. Fortunately, the FIFE site is relatively homogeneous over spatial scales of approximately 100 meters, so that the geometric correction procedure applied to the CCT-P format data is not likely to degrade the integrity of the data in the thermal band as much as it might for an area with many abrupt boundaries in surface temperature, such as an agricultural area.

With regard to the radiometric correction applied to the data on the CCT-P tape, the data provided in the FIFE Information System and used in this analysis were original CCT-P tape corrected digital numbers. The radiometric correction was not reversed, and the calibration coefficients provided by EOSAT were used to convert the corrected digital numbers to apparent at-satellite radiance. For applications requiring the best possible radiometric integrity of the data in the visible and near-infrared bands, it would be desirable to reverse those corrections and apply the most recent sensor calibration coefficients obtained by current research in that area (for example, Slater et al., 1986). However, for this analysis, it is not likely that use of the original CCT-P data had a substantial effect on the results reported here. The procedures described in this chapter utilize only the data from bands TM3 and TM4 to obtain vegetation indices, and the vegetation indices are then related to parameters controlling the soil heat flux and the sensible heat flux. The uncertainty in those relationships is considerably larger than the error in the values of the vegetation indices resulting from use of the CCT-P data.

One closely related application that is more sensitive to the radiometric accuracy of the Landsat TM data in the visible and near-infrared bands is the estimation of net solar surface radiation from TM data. As noted above, the estimation of the net solar radiation for the FIFE site using TM data was a separate topic of research discussed by Dubayah et al. (1990). The net solar radiation map that they produced from the August 15, 1987 TM image over the FIFE site will be used in the next chapter. A summary of their discussion of sources of error in the net solar radiation values is included there.

For all of the TM images available over the FIFE experimental site, the ground flux stations and meteorological stations were located on the image by FIFE Information System personnel. For each ground station that could be located with reasonable confidence, the digital numbers for approximately 2-5 image pixels were averaged to provide an estimate of the satellite measurements over each ground site.

As described above, the digital numbers were converted to apparent at-satellite radiances with the gain and offset coefficients provided by EOSAT. The procedure for correcting the satellite data for atmospheric effects and the computation of surface reflectance and temperature values for these extracts of satellite data are discussed in a separate section below.

Comparison of Ground and Helicopter-Based Data

Comparisons of the values of nadir-view surface reflectances and temperatures measured with the ground-based MMR and the helicopter-based MMR are shown in Figures 4.1, 4.2, and 4.3. The data shown in Figures 4.1 and 4.2 are for MMR Band 3 (RED) and MMR Band 4 (NIR) reflectances, respectively. The data points are labeled with the flux station ground site numbers. These points represent all the times of data acquisition for which ground data and helicopter data were acquired at the same site simultaneously. The data set includes measurements taken at different times of day for 2-3 days in each IFC. The solar zenith angle at the time of acquisition ranges from approximately 20° to 70°. The solid line on the plots is the 1:1 line, which represents exact agreement between the ground- and helicopter-based reflectances. The agreement between the ground- and helicopter-based reflectances shown in these figures is quite good for MMR Band 3 and reasonably good for MMR 4.

The comparison between ground- and helicopter-based surface temperatures shown in Figure 4.3 is quite good. Unfortunately, the thermal band data were not

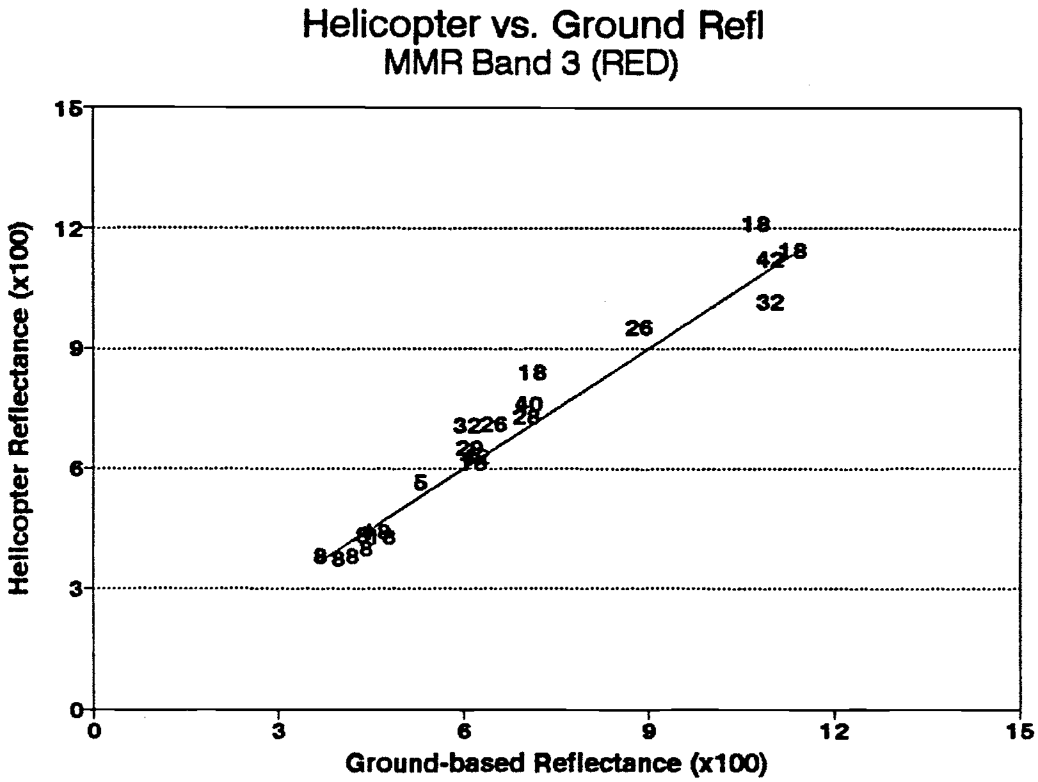

Figure 4.1. Comparison of MMR Band 3 reflectances derived from near simultaneous data acquired over various ground sites with nadir-viewing ground and helicopter-based instruments. Data shown include points from several days in each IFC.

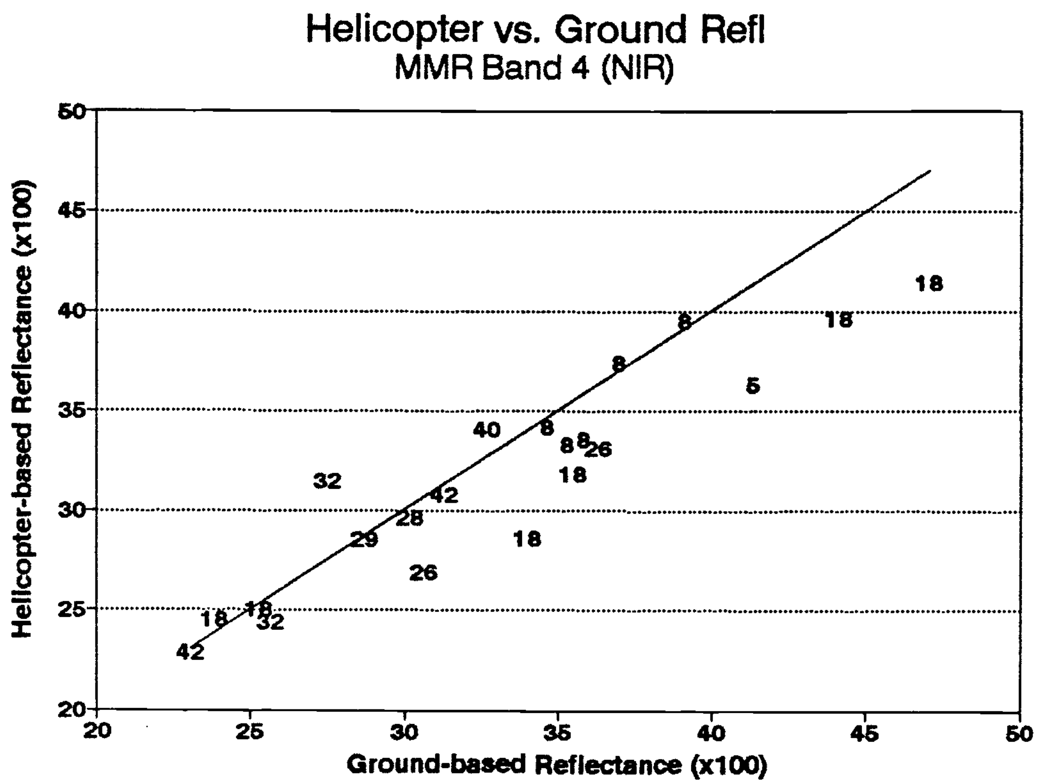

Figure 4.2. Comparison of MMR Band 4 reflectances derived from near simultaneous data acquired over various ground sites with nadir-viewing ground and helicopter-based instruments. Data shown include points from several days in each IFC.

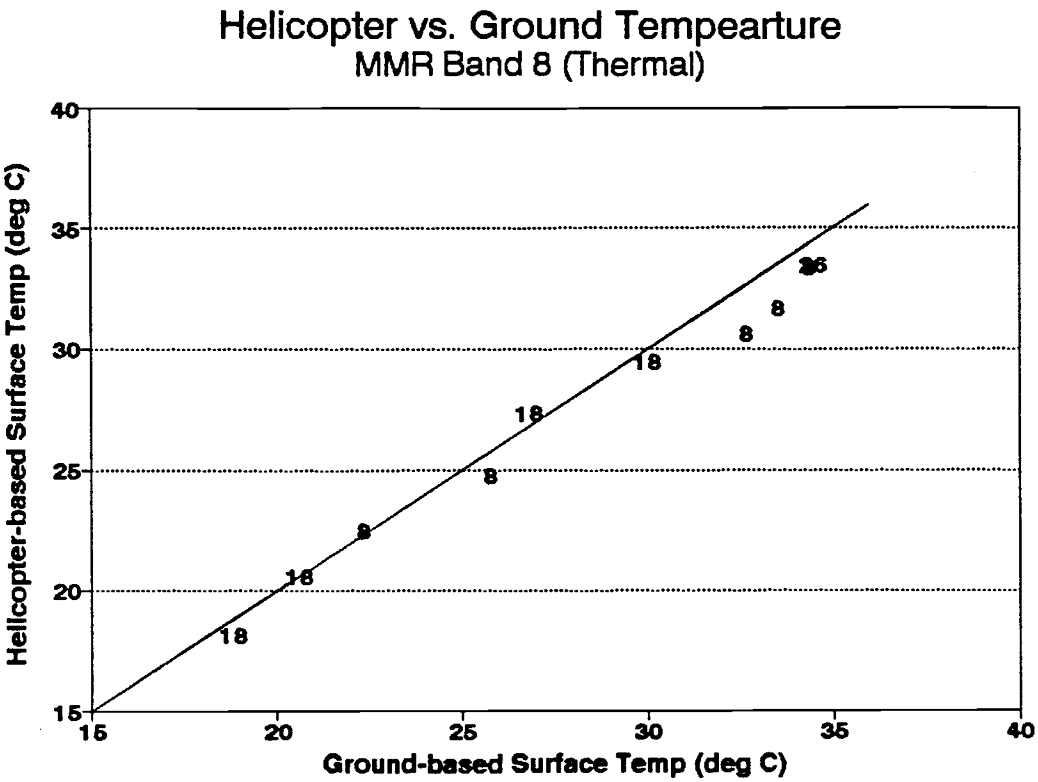

Figure 4.3. Comparison of surface temperatures derived from MMR Band 8 from near simultaneous data acquired over various ground sites with nadir-viewing ground and helicopter-based instruments. Data shown include points from several days in IFC 2, IFC 3, and IFC 4.

available from the ground-based instrument during IFC 1 and portions of IFC 4; therefore, there are fewer data points available for comparison than for the case of the Band 3 and Band 4 reflectances.

Given the possible sources of error in these measurements, the agreement between the ground-based and helicopter-based reflectances and temperatures is fairly good. Because it took more time to move the ground-based apparatus to several target areas near the flux station, the ground points represent data acquired over about a 30-minute period bracketing the helicopter overpass time. They also represent an average of about 6-8 different target areas near the flux stations which did not overlap exactly with the areas viewed by the helicopter instrument. Additionally, there are several sources of error in deriving the reflectance estimates from the helicopter instrument. These include: (1) possible errors in the cross-calibration of the instrument used in the helicopter and the instrument used over the reflectance plate on the ground, and (2) possible differences in the irradiance at the site of the ground reflectance plate and the flux station sites, arising from topography and atmospheric conditions.

Estimation of Fluxes with Helicopter-Based Data

Various methods for deriving soil heat flux and sensible heat flux from a combination of ground-based data and helicopter-based remotely sensed data were evaluated using data from nearly all the time periods and stations for which the helicopter data were available. The results were compared with the fluxes measured with eddy correlation or Bowen ratio techniques at the ground flux stations. The site number designations and summary information on the instrumentation and investigator teams for the various flux stations used in this analysis are presented in Table 4.1. Helicopter-based data were available for several different time periods on 3 or more different days in each IFC.

In this section, the comparison of ground-based estimates of soil heat flux with various methods for estimating the soil heat flux as a function of net radiation and other remotely sensed variables is presented. Next, the relationships between surface temperature and aerodynamic temperature are explored as a foundation for developing a method to estimate sensible heat flux. Last, the comparison of ground-based sensible heat flux with various methods for estimating the sensible heat flux from remotely sensed surface temperature is presented.

Estimation of Soil Heat Flux

Physical Considerations. The physical characteristics of the surface which affect the soil heat flux, G, are: (1) the amount of net radiation received by the exposed soil, and (2) soil state variables and parameters which control the fraction of soil net radiation absorbed by the soil (such as soil temperature, soil moisture, and soil thermal properties). The fraction of total net radiation which reaches the soil can be expressed as (Goudriaan, 1977):

$$R_{net,soil} = R_{net,total} \exp\left(-.5\sec\theta_z * LAI\right), \tag{4.1}$$

where $R_{net,soil}$ (Wm^{-2}) is the net radiation reaching the soil surface, $R_{net,total}$ (Wm^{-2}) is the total net radiation at the surface, θ_z is the solar zenith angle, and LAI is the leaf area index. (The reader should note that, in this chapter only, the total net radiation reaching the surface is referred to as $R_{net,total}$ in order to distinguish from the fraction of the net radiation reaching the soil surface, $R_{net,soil}$. In other chapters of this dissertation, in which partitioning of the net radiation between soil and canopy is not addressed, the total net radiation is referred to simply as R_{net}.) The constant 0.5 in Equation (4.1) is a function of leaf angle distribution, where the value of 0.5 is assumed for a spherical leaf distribution.

The procedure by which remotely sensed data can theoretically be used to estimate G from $R_{net,total}$ with fairly simple physical considerations would be to: (1) estimate $R_{net,total}$ from remotely sensed data as described in Chapter 1, (2) estimate LAI using vegetation indices derived from remotely sensed data together with an empirical relationship between vegetation indices and LAI, (3) apply Equation (4.1) to estimate the fraction of total net radiation reaching the soil (i.e., the value of $R_{net,soil}$), and (4) use remotely sensed estimates of soil moisture to estimate the fraction of $R_{net,soil}$ that is used for soil heat flux. The feasibility of this approach was evaluated using data from IFC 3 and IFC 1.

Using the LAI data acquired at each surface site approximately once per week, and the $R_{net,total}$ values estimated at the ground-based flux stations for all of the helicopter data periods, the value of $R_{net,soil}$ was computed using Equation (4.1). In order to evaluate the relationship between observed G and the physically based parameters described above (i.e., soil moisture, leaf area index), the G values observed at the same time periods were plotted against $R_{net,soil}$ computed from Equation (4.1) for the data periods during IFC 3. The results are shown in Figure 4.4, where the data point labels represent the values of the ratio of gravimetric soil moisture observed on that day to saturated soil moisture for that site (θ/θ_{sat}, or relative soil moisture saturation). The results show that, for the IFC 3 time period, G is a fairly constant fraction of $R_{net,soil}$ when $R_{net,soil}$ is greater than about 300 Wm^{-2}. When $R_{net,soil}$ is less than about 300 Wm^{-2}, i.e., in the early morning or late afternoon hours, the ratio of $G/R_{net,soil}$ flattens out. Importantly, there does not appear to be a significant trend in the relationship for different values of relative soil moisture saturation.

Because the relationship between G and $R_{net,soil}$ flattens out at lower values of $R_{net,soil}$, it might be concluded that diurnal trends in G are not fully accounted for in Equation (4.1). However, by examining the same results as those shown in Figure 4.4 plotted with data labels which show the time of day of the observation (Figure 4.5) and the ground station number (Figure 4.6), it can be deduced that lack of sensitivity of G to computed $R_{net,soil}$ at lower values of $R_{net,soil}$ is more likely due to the fact that the magnitude of the uncertainty in estimating $R_{net,total}$ at the ground stations is a greater percentage of G when G is less than 50 Wm^{-2} than for larger values of G. Another very likely source of error in the results shown in Figures 4.4-

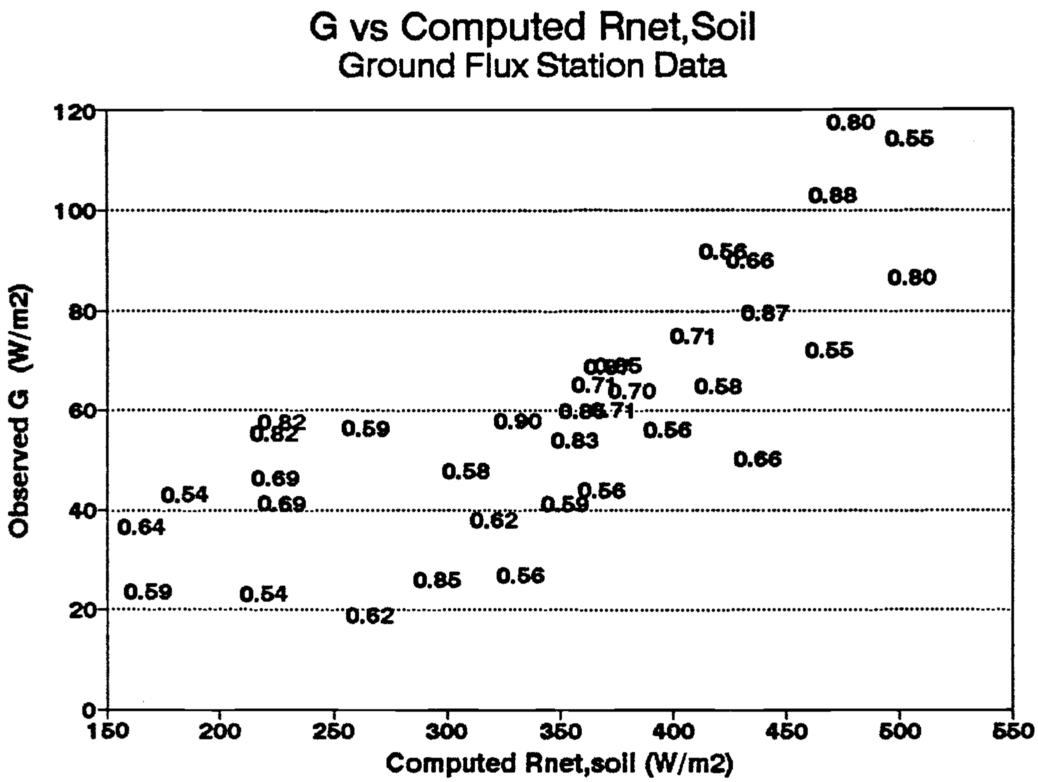

Figure 4.4. Soil heat flux measured at various ground flux stations plotted against $R_{net,soil}$ as estimated from Equation (4.1) together with ground-based measurements of $R_{net,tot}$ and LAI for days during IFC3. Data points are labeled with values for fraction of soil moisture saturation.

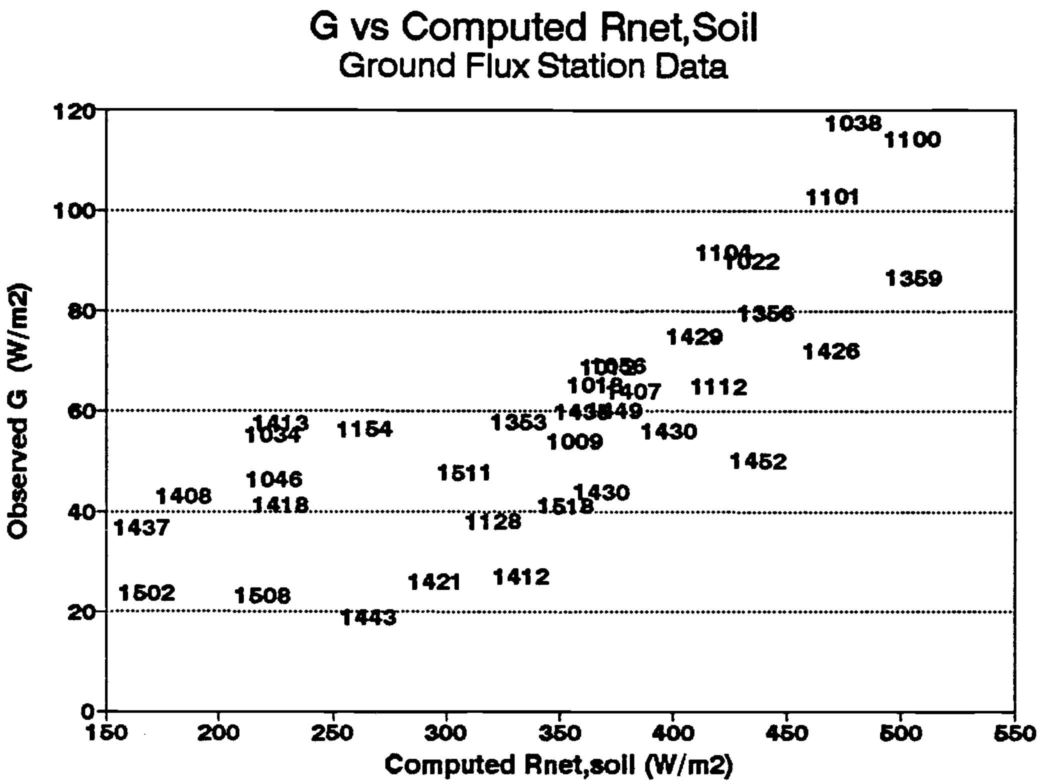

Figure 4.5. Soil heat flux measured at various ground flux stations plotted against $R_{net,soil}$ calculated with Equation (4.1) for days during IFC3. Data points are labeled with local time of day of observations.

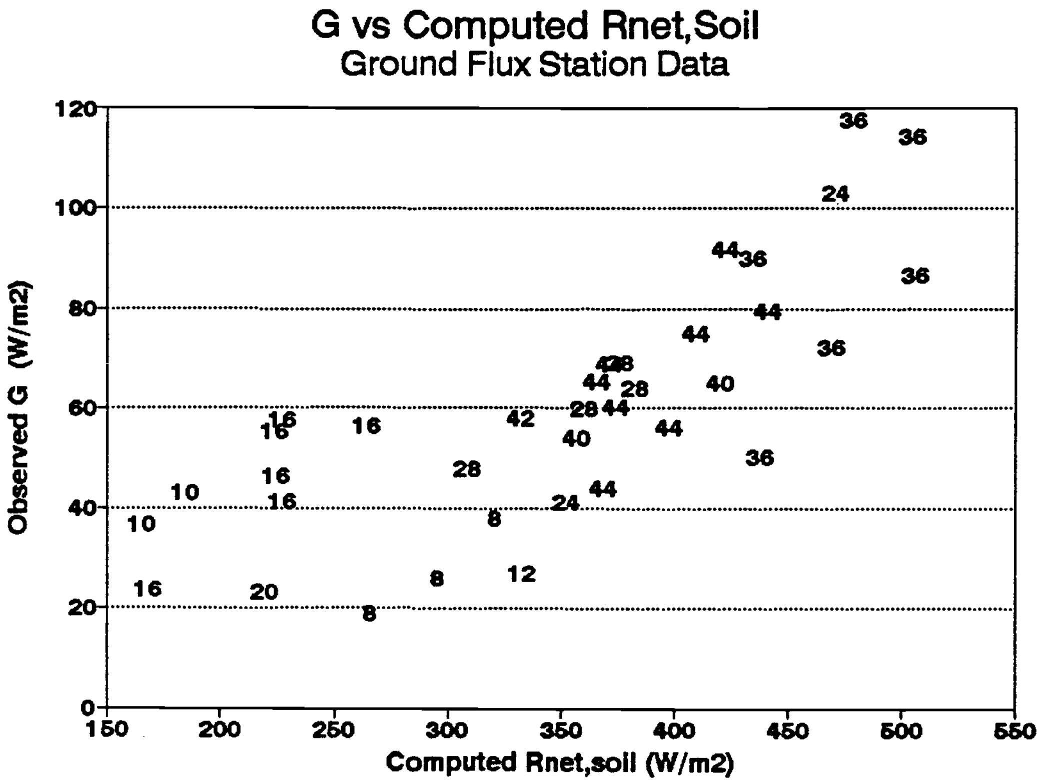

Figure 4.6. Soil heat flux measured at various ground flux stations plotted against $R_{net,soil}$ calculated with Equation (4.1) for days during IFC3. Data points are labeled with ground station site numbers.

4.6 is that the ground measurements of LAI values for sites 10 and 16 underestimated the actual LAI.

The correlation of G with $R_{net,soil}$ computed from Equation (4.1) is relatively strong over reasonable ranges of G. In addition, there are no trends shown in the other factors plotted as data labels in Figures 4.4-4.6. It appears that the most important physical factor controlling the fraction of R_{net} used as soil heat flux is the fractional area of exposed soil subject to direct radiation. As described by Equation (4.1), this is controlled by a combination of the solar zenith angle and the LAI.

In order to evaluate the feasibility of estimating LAI from vegetation indices derived from the helicopter-based reflectance data in MMR Bands 3 and 4, the values of two vegetation indices were plotted against LAI measured at the ground stations. As mentioned in the description of the LAI measurements in Chapter 3, the LAI measurements represent an average of 5 measurements at a given site on a given day, and the standard deviation among those 5 measurements was often as large as 60% of the average LAI value.

The first vegetation index computed from the helicopter-based MMR Band 3 (RED) and MMR Band 4 reflectances was the Normalized Difference Vegetation Index (NDVI), given by:

$$\text{NDVI} = (\rho_{NIR} - \rho_{RED})/(\rho_{NIR} + \rho_{RED}), \tag{4.2}$$

where ρ_{NIR} is the reflectance in MMR Band 4, and ρ_{RED} is the reflectance in MMR Band 3. The second vegetation index computed from helicopter-based MMR data was the Soil Adjusted Vegetation Index (SAVI), given by (Huete, 1988) as:

$$\text{SAVI} = [(\rho_{NIR} - \rho_{RED})/(\rho_{NIR} + \rho_{RED} + L)][1 + L]. \tag{4.3}$$

L is an arbitrary constant shown by (Huete, 1988) to have a slightly different optimal value over different ranges of values for LAI. The value of the constant used in this case was L = 0.5. The SAVI was developed in an attempt to minimize the effect of soil background effects on the vegetation index for surfaces with sparse and moderate vegetation cover.

The relationship between the NDVI and LAI for the helicopter-based data acquired over several days in IFC 3 is shown in Figure 4.7. The data labels are the solar zenith angles at the time of acquisition of the helicopter-based remote sensing data. The relationship between the SAVI and LAI for the same data periods is shown in Figure 4.8. For both indices, there is considerable scatter in the relationship, most likely due to the large scatter in the LAI values measured at the ground stations. As expected, the values of the vegetation indices vary with solar zenith angle at the time of observation. Any empirical relationships developed between the vegetation indices and the LAI using this data would be very site specific and would be dependent on solar zenith and azimuth angle during the remote sensing data acquisition.

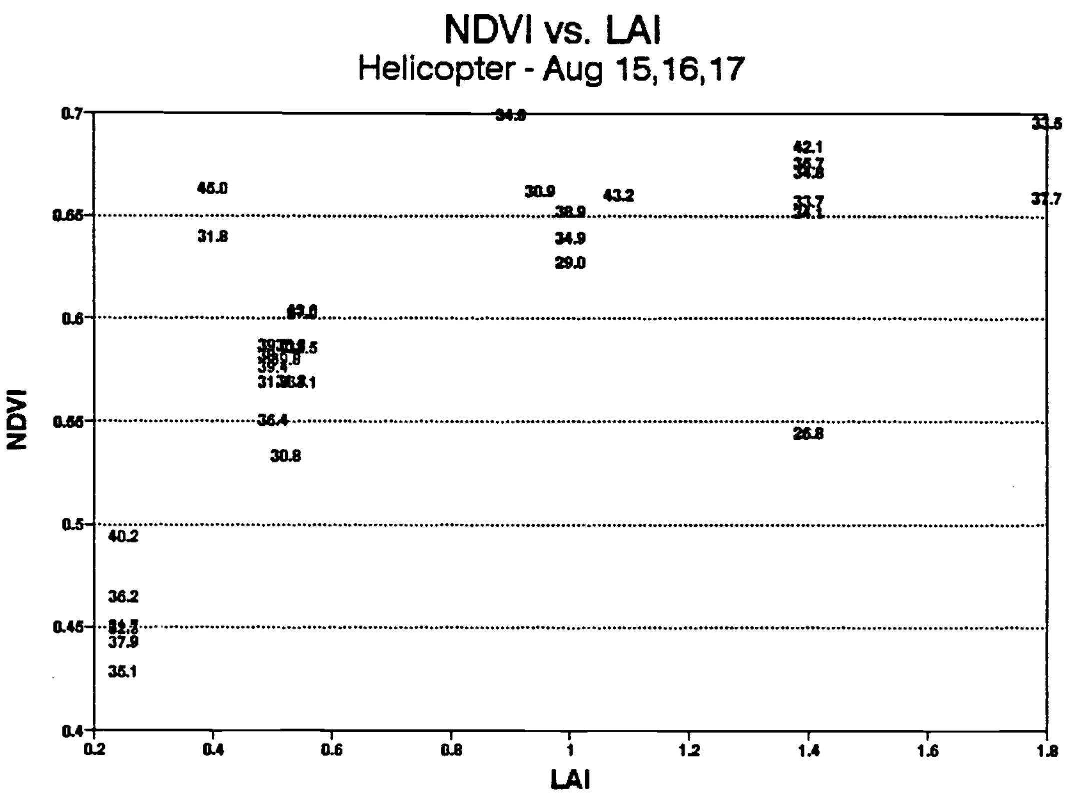

Figure 4.7. Values of Leaf Area Index (LAI) vs. NDVI calculated from helicopter-based data in IFC3. Data labels are the solar zenith angles for the time of the data acquisition.

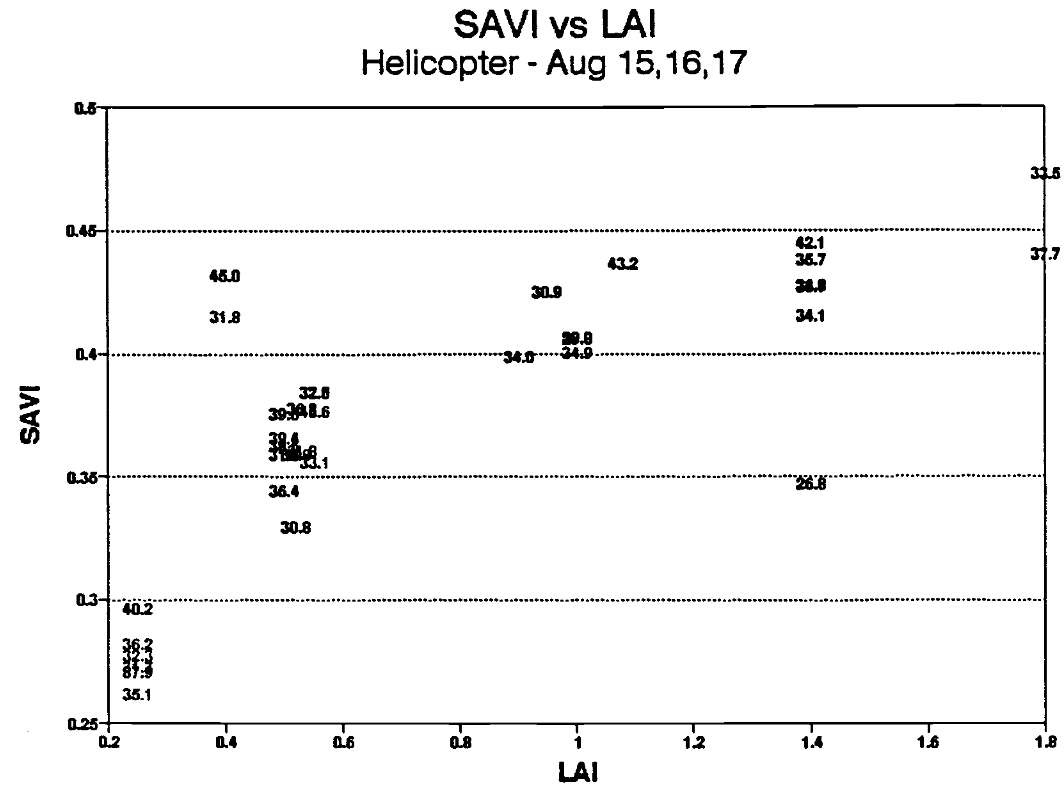

Figure 4.8. Values of Leaf Area Index (LAI) vs. SAVI calculated from helicopter-based data in IFC3. Data labels are the solar zenith angles for the time of the data acquisition.

Direct Relationships Between G and Vegetation Indices

It is not possible at this time to derive traditional measures of vegetation cover, such as LAI, directly from remote sensing data without the influence of solar angle effects. Because both vegetation cover and solar zenith angle are factors which determine the amount of $R_{net,total}$ which reaches the soil surface, there is some physical basis to expect that a relationship would exist between the ratio of $G/R_{net,total}$ at different solar zenith angles and vegetation indices derived from remotely sensed observations at those same solar zenith angles.

As discussed in Chapter 1, several researchers evaluated this relationship for several types of agricultural crops (Clothier et al., 1986; Kustas and Daughtry, 1990). The relationship derived by Kustas and Daughtry (1990) using data from bare soil, cotton, and alfalfa crops was:

$$G/R_{n,total} = 0.325 - 0.208 * (NDVI). \qquad (4.4)$$

They concluded that this relationship should be evaluated further over other types of vegetated surfaces.

The values for $G/R_{net,total}$ measured at the ground flux stations plotted against NDVI estimated from the helicopter-based remotely sensed data are presented in Figure 4.9. The regression relationship between them is shown as the lower solid line in Figure 4.9. The Kustas and Daughtry (1990) relationship is also plotted in Figure 4.9 as the upper solid line. These results indicate that the relationship between vegetation indices and the ratio of $G/R_{net,total}$ are rather specific to the

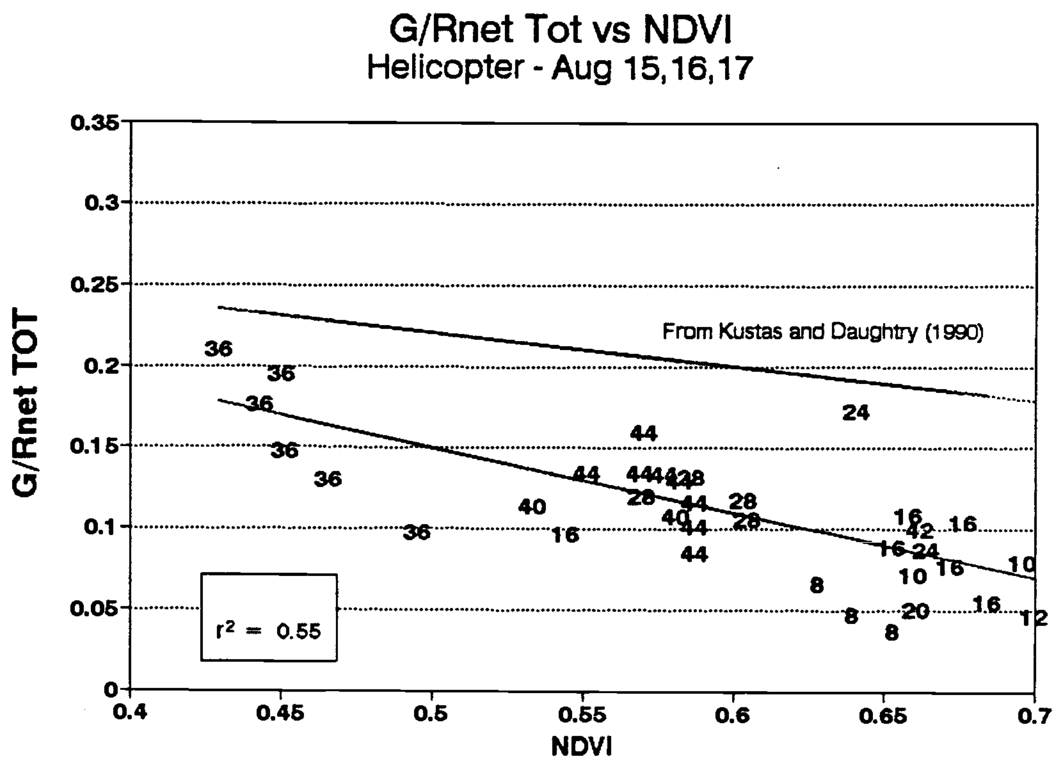

Figure 4.9. Ratio of G/Rnet,total plotted against NDVI values derived from the helicopter remote sensing data during IFC3. The data labels refer to the ground-based site number.

vegetation type or structure. This is not unexpected, because the relationship between vegetation indices and vegetation cover is different for different vegetation types and structures. The regression equation derived from the data shown in Figure 4.9 is:

$$G/R_{net,total} = 0.35 - 0.40 * (NDVI). \tag{4.5}$$

The values for $G/R_{net,total}$ measured at the flux stations for these same time periods are plotted against the SAVI in Figure 4.10. The correlation coefficient between the SAVI and $G/R_{net,total}$ is not significantly different than that between the NDVI and $G/R_{net,total}$. Because the NDVI is still more widely used at this time, the subsequent analysis of relationships between vegetation indices and $G/R_{net,total}$ will primarily utilize the NDVI.

In order to evaluate how well Equation (4.5) predicts the soil heat flux for this same data set, values of G were derived from Equation (4.5) using helicopter-based NDVI and the $R_{net,total}$ from the ground-based flux stations. These computed G values are plotted against the observed G values shown in Figure 4.11. It should be noted that this is not a validation of Equation (4.5) because the results shown in Figure 4.11 represent the application of Equation (4.5) to the same data set from which it was derived. The purpose of comparing these computed values of G with the observed values of G is simply to check the uncertainty with which G can be computed for that same data set. The root mean square error (RMSE) for the results shown in Figure 4.11 was 15 Wm^{-2}. This level of error in estimating soil heat

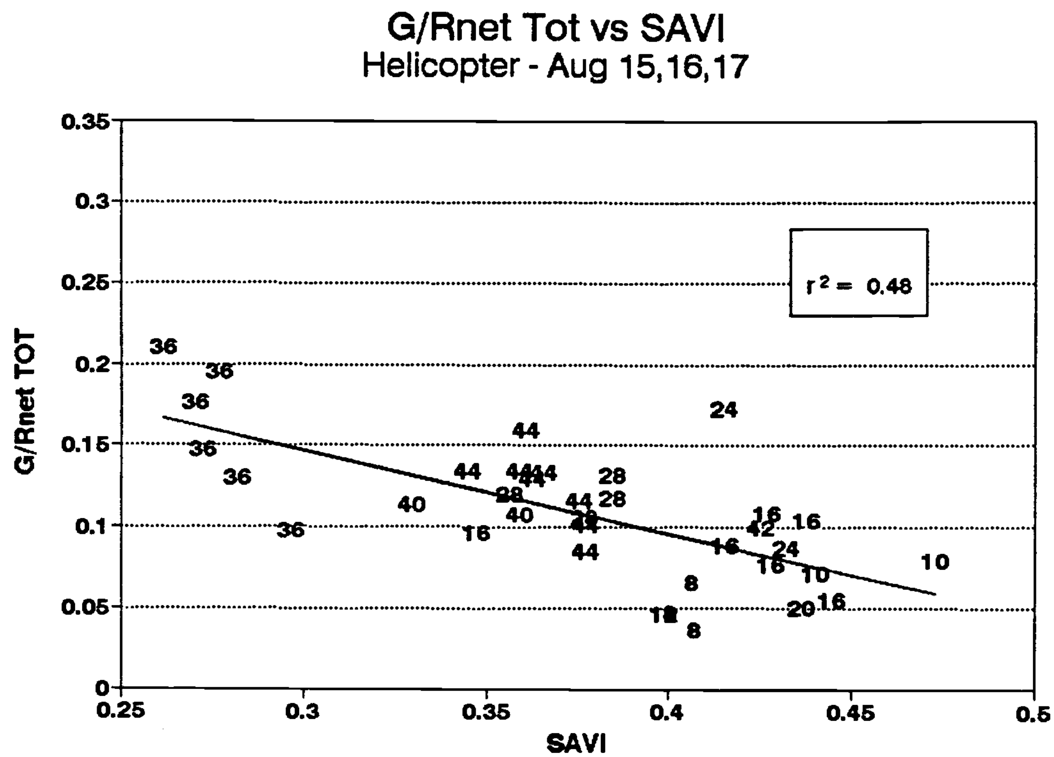

Figure 4.10. Ratio of G/Rnet,total plotted against SAVI values derived from the helicopter remote sensing data during IFC3. The data labels refer to the ground-based site number.

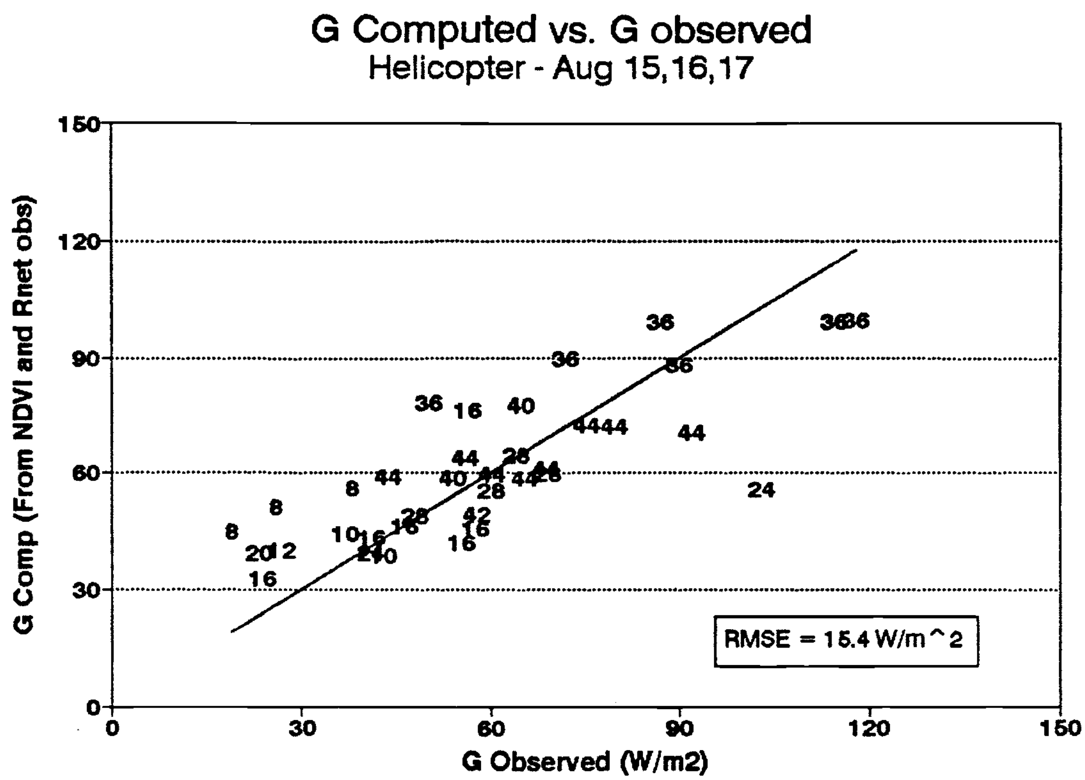

Figure 4.11. Soil heat flux measured at the ground-based flux sites versus the soil heat flux computed from Equation (4.5) using helicopter-based remotely sensed data and ground estimates of $R_{net,total}$.

flux is well within the level of uncertainty with which soil heat flux can be measured with ground-based instruments. However, it should be noted that, in practical application, the uncertainty in the estimation of G with a relationship such as Equation (4.5) is subject to uncertainty in the estimation of $R_{net,total}$ with a combination of ground and remotely sensed data, a topic not addressed in this research.

Surface Temperature, Aerodynamic Temperature, and Surface Factors

Background. As discussed in Chapter 1, there are many challenges associated with the estimation of sensible heat flux with remotely sensed data over surfaces with partial vegetation cover. One of the primary difficulties is that the net aerodynamic temperature, which is the temperature at the virtual source/sink height for net exchange of heat between the soil/canopy system and the atmosphere, is a rather dynamic quantity which results from complex interactions between the soil, canopy, and intercanopy airspace (Kustas et al., 1989a). The relationship between aerodynamic temperature and sensible heat flux is given by:

$$H = \rho C_p \, (T_o - T_a)/r_a, \tag{4.6}$$

where H is the sensible heat flux (W/m^{-2}), ρC_p is the heat capacity of air ($Jm^{-3}C^{-1}$), T_o is the aerodynamic temperature, T_a is the air temperature at a reference height above the canopy, and r_a (sm^{-1}) is the aerodynamic resistance to heat transfer computed as a function of canopy height and windspeed at a reference height above the surface.

Under conditions for which the kinetic temperature of both the exposed bare soil surface and the vegetation are nearly the same (such as early in the day or under conditions when the surface soil is quite moist), then the aerodynamic temperature does not deviate substantially from the composite surface temperature measured with a remote sensing instrument. However, when the exposed bare soil surface is dry, and at a very different kinetic temperature than transpiring vegetation, the aerodynamic temperature is a complex function of many factors. These factors include: (1) soil and vegetation temperatures, (2) the degree of aerodynamic contact between the soil and vegetation surfaces and the intercanopy airspace, and (3) modifications to the intercanopy airspace that result from interactions with both the soil and vegetation components of the surface.

Kustas et al. (1989a) developed a semi-empirical expression for an adjustment to aerodynamic resistance which accounted somewhat for the shift of the source-sink height for heat due to changes in the contribution to H from the soil and vegetation surfaces. They proposed an expression for the quantity kB^{-1}, the ratio of the roughness lengths for heat and momentum:

$$kB^{-1} = 0.17u(T_s - T_a), \tag{4.7}$$

where u is the windspeed at a reference height, and T_s is the surface temperature measured with remote sensing instruments. The adjusted aerodynamic resistance, r_a', is given by the expression:

$$r_a' = r_a + kB^{-1}(r_a/u)^{1/2} \tag{4.8}$$

The equation was developed with data over a semi-arid shrub-dominated area and provided good estimates of sensible heat flux using Equation (4.6) with T_s used in place of T_o, and r_a' used in place of r_a. The relationship was derived from physical considerations, but the form of Equation (4.7) and the constant 0.17 are empirically derived. Thus, there is a need to evaluate the performance of the relationship over other types of surfaces.

The temperature of a surface measured with remotely sensed data is a combination of the kinetic temperatures and emissivities of the soil and vegetation components. However, it is not feasible to derive from remote sensing measurements, or a combination of remote sensing measurements and models, all of the parameters required to describe these component temperatures, aerodynamic resistance parameters, and the interactions of the soil and plant components in a detailed, physically,based manner. Therefore, it is desirable to examine the relationship between aerodynamic temperature and quantities that can be observed with remotely sensed data, such as surface temperature and soil moisture, for the field data set described here.

Evaluation of Field Data. The values of aerodynamic temperature for the time periods of the helicopter overpasses at most flux stations were computed using Equation (4.6), together with the 30-minute averages of sensible heat flux and T_a estimated from the ground flux station. The r_a term in Equation (4.6) was computed using the canopy height and windspeed data from the ground-based flux measurements and the expression given by Mahrt and Ek (1984):

$$r_a = \{\ln[(z-d + z_o)/z_o]/k\}^2 * (1 + 15Ri)(1 + 5Ri)^{1/2}/u. \tag{4.9}$$

for the stable case $[(T_s-T_a)<0]$, and:

$$r_a = \{\ln[(z-d + z_o)/z_o]/k\}^2 * \{1 - 15Ri)/[1 + C(-Ri)^{1/2}]\}/u \tag{4.10}$$

for the unstable case $[(T_s-T_a)>0]$. Ri is the Richardson number, $[Ri = g(T_a-T_s)(z-d)/T_aU^2]$, g is the acceleration due to gravity (ms^{-2}), u is the windspeed (ms^{-1}), z is the height (m) above the surface at which the windspeed and air temperature are measured, d is the displacement height (m), assumed to be 0.65h, where h is the average canopy height (Brutsaert, 1982), z_0 is the roughness length (m), assumed to be 0.1h, k is von Karman's constant (0.4), and:

$$C = 75k^2 [(z-d + z_o]^{1/2}/\{\ln[(z-d + z_o)/z_o]\}. \tag{4.11}$$

It should be noted that the estimation of T_0 is subject to uncertainty in the estimation of H from the ground-based stations and is also subject to errors in the estimation of r_a. There is even more uncertainty in the estimation of r_a for surfaces with partial vegetation canopy than for surfaces with complete vegetation cover. This is because there is reason to believe that the usual empirical expressions relating canopy height to roughness parameters, which were developed for relatively complete, uniform canopy cover, may not be applicable to surfaces with partial vegetation cover.

The difference between the aerodynamic temperature and the surface temperature (T_s-T_o) estimated from the helicopter-based MMR data was evaluated with respect to surface parameters that would be expected to affect that difference and which could be estimated with remotely sensed data, such as vegetation cover, soil moisture, and the quantity (T_s-T_a). The results of these comparisons for the data periods during IFC 3 are shown in Figures 4.12 through 4.14. In Figure 4.12, (T_s-T_o) is plotted against the SAVI, where the data labels indicate the degree of surface soil moisture saturation. The correlation coefficient between the (T_s-T_o) and the SAVI was not significant (r^2 = 0.62). Further, there does not appear to be a discernible trend in the relationship with soil moisture saturation (plotted as data labels in Figure 4.12). From physical considerations, it would be expected that higher fractions of bare soil exposed at the surface (i.e., lower values of vegetation index) and lower values of soil moisture saturation would both contribute to larger values of (T_s-T_o). A simple empirical function that accounted for both of these effects was developed and tested for a significant relationship with (T_s-T_o). The results of that comparison are shown in Figure 4.13. There was not a significant correlation (r^2 = 0.55) between that function and (T_s-T_o).

Values of (T_s-T_o) are plotted against the value of reflectance in MMR B3 (RED) in Figure 4.14. The labels on the data points in the figure refer to the surface flux station site numbers. There is no indication of a significant relationship between (T_s-T_o) and red reflectance either (r^2 = 0.65), but it is interesting to note

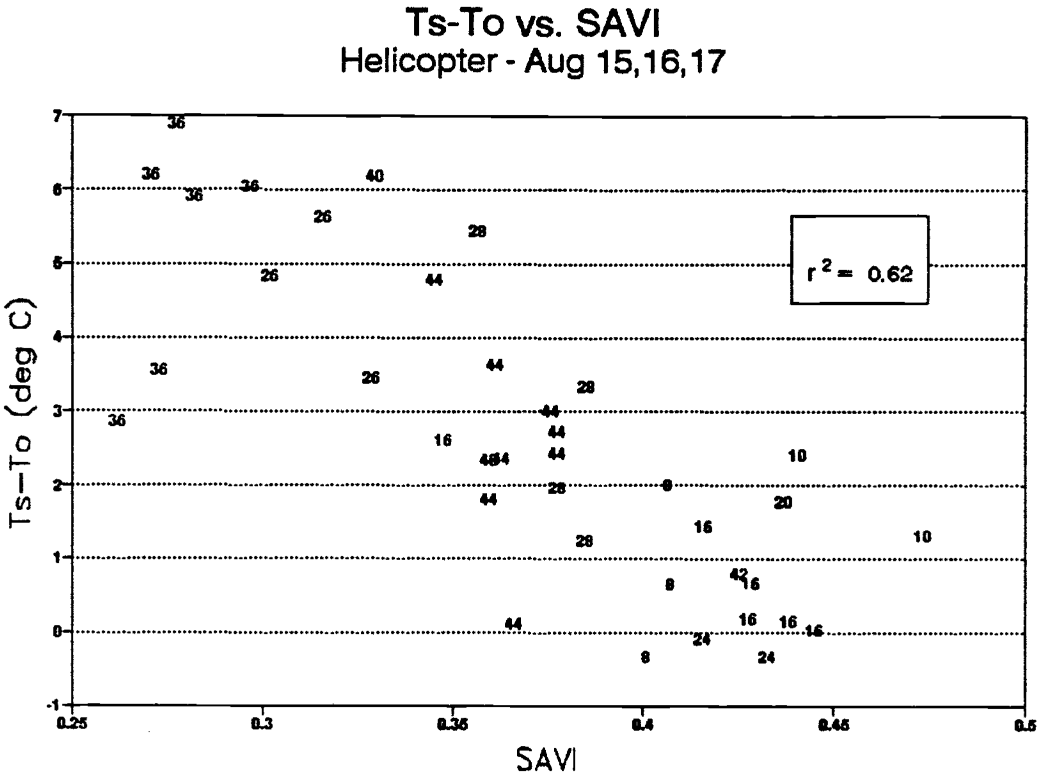

Figure 4.12. The difference between the surface temperature and aerodynamic temperature for various ground flux stations plotted as a function of SAVI estimated from helicopter-based remote sensing data during IFC3. Data labels refer to the relative soil moisture saturation (θ/θ_z).

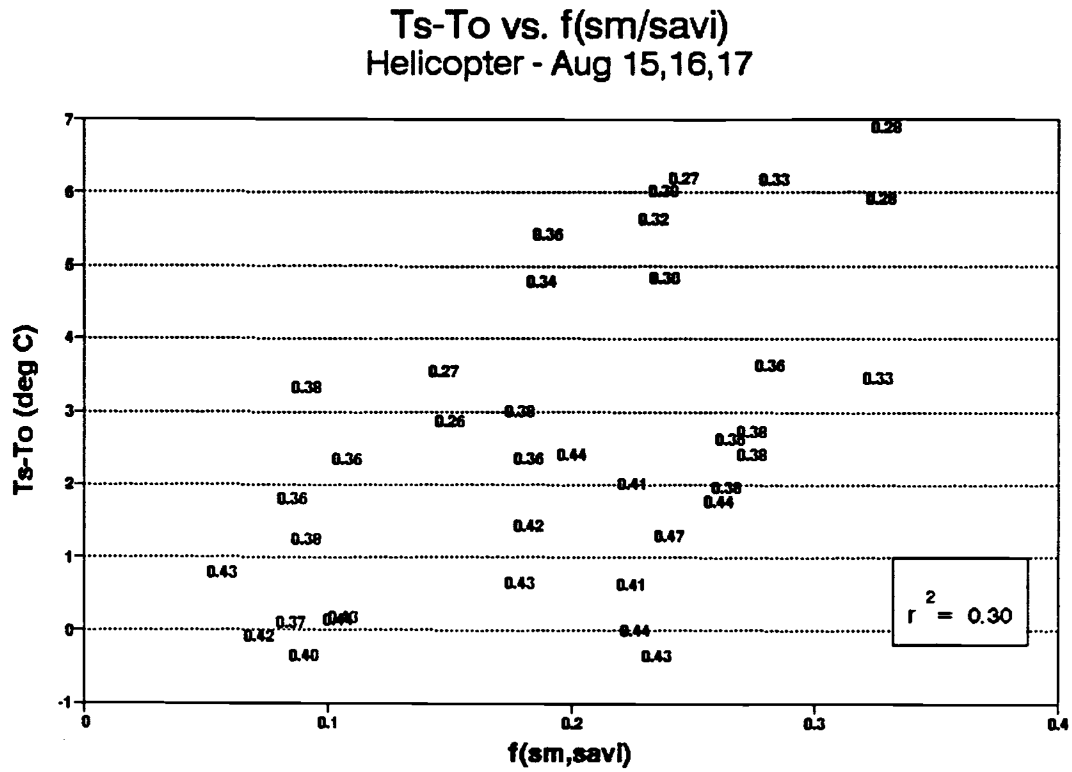

Figure 4.13. The difference between the surface temperature and aerodynamic temperature for various ground flux stations plotted as a function of a combination of relative soil moisture saturation and the SAVI estimated from helicopter-based remote sensing data during IFC3. Data labels refer to the relative soil moisture saturation (θ/θ_z).

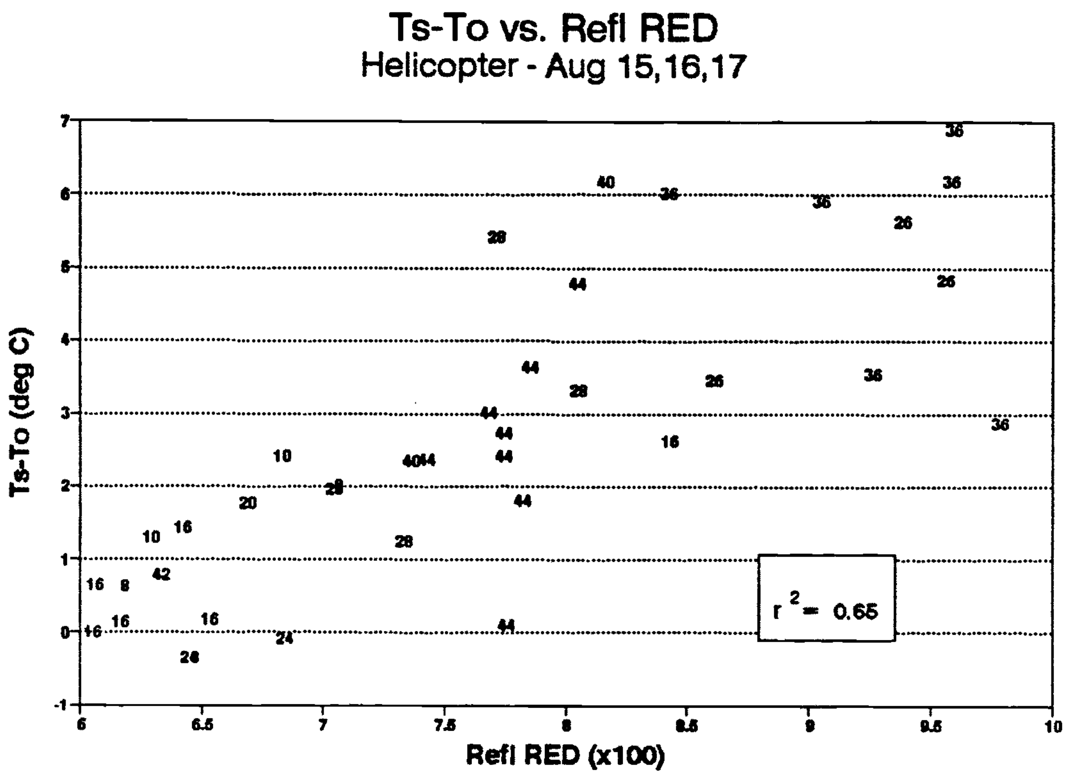

Figure 4.14. The difference between the surface temperature and aerodynamic temperature for various ground flux stations plotted as a function of reflectance in MMR Band 3 (RED) estimated from helicopter-based remote sensing data during IFC3. Data labels refer to the various ground-based flux stations over which the data was acquired.

that the level of the relationship is not significantly better, but is also not significantly worse, than the relationship with the SAVI.

Values of $(T_s\text{-}T_o)$ are plotted against the values of $(T_s\text{-}T_a)$ for the IFC 3 data periods in Figure 4.15. The labels on the data points in the figure refer to the flux station site numbers. The r^2 value for this relationship is 0.94. In order to test this relationship over other data periods, the same variables are plotted in Figure 4.16 for the data from the IFC 1 time period. The relationship between $(T_s\text{-}T_o)$ and $(T_s\text{-}T_a)$ for most of the helicopter overpass data periods in IFC 1, IFC 2, and IFC 3 is shown in Figure 4.17. The solid lines shown in Figures 4.15-4.17 are the regression lines for each of the specified data sets. The regression equations determined with each data set are summarized below:

$$\text{IFC1 (June) data:} \quad (T_s - T_o) = -1.56 + 1.03(T_s - T_a); \tag{4.12}$$

$$\text{IFC2 (August) data:} \quad (T_s - T_o) = -.62 + .80(T_s - T_a); \tag{4.13}$$

$$\text{All (IFC1,2,3) data:} \quad (T_s - T_o) = -.86 + .89(T_s - T_a). \tag{4.14}$$

In summary, it appears that, when considering data from many different flux stations, there is sufficient scatter in the values of $(T_s\text{-}T_o)$ that it is difficult to discern significant relationships between $(T_s\text{-}T_o)$ and variables which should be related to $(T_s\text{-}T_o)$ through physical considerations. However, the remotely sensed surface temperature, which integrates the effect of many of the physical factors that would be expected to influence $(T_s\text{-}T_o)$, such as amount of exposed bare soil, soil moisture,

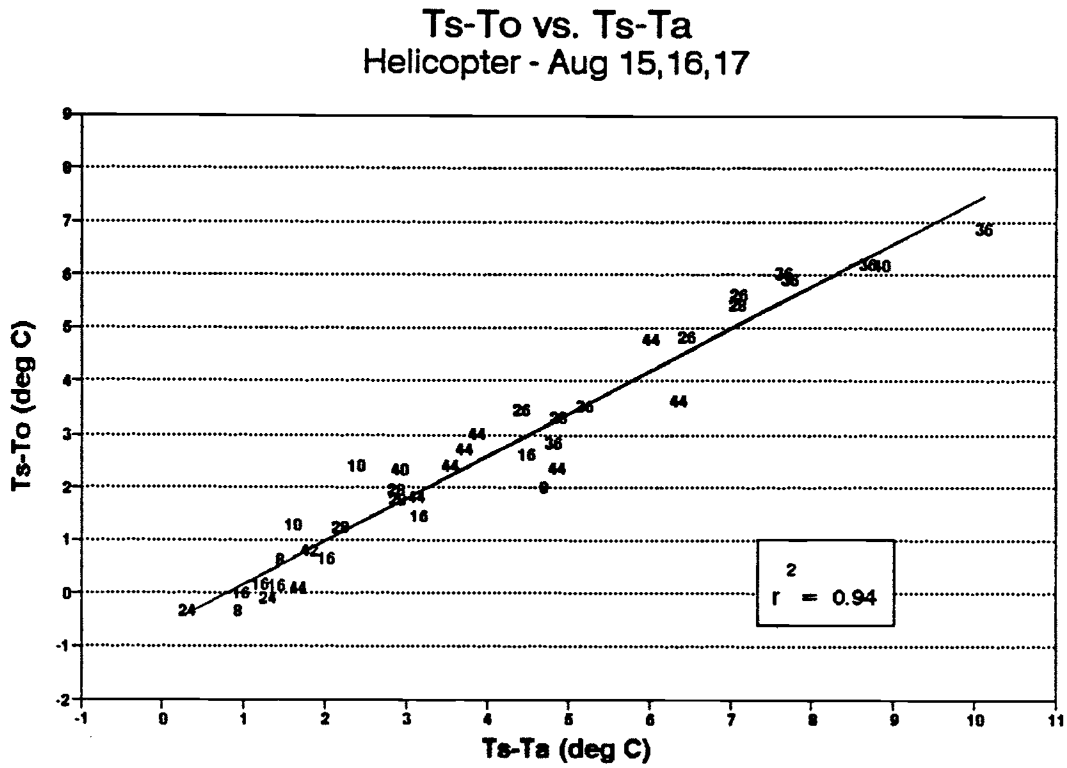

Figure 4.15. The difference between the surface temperature and aerodynamic temperature for various ground flux stations plotted as a function of the surface-air temperature difference estimated from helicopter-based remote sensing data during IFC3. Data labels refer to the various ground-based flux stations over which the data were acquired.

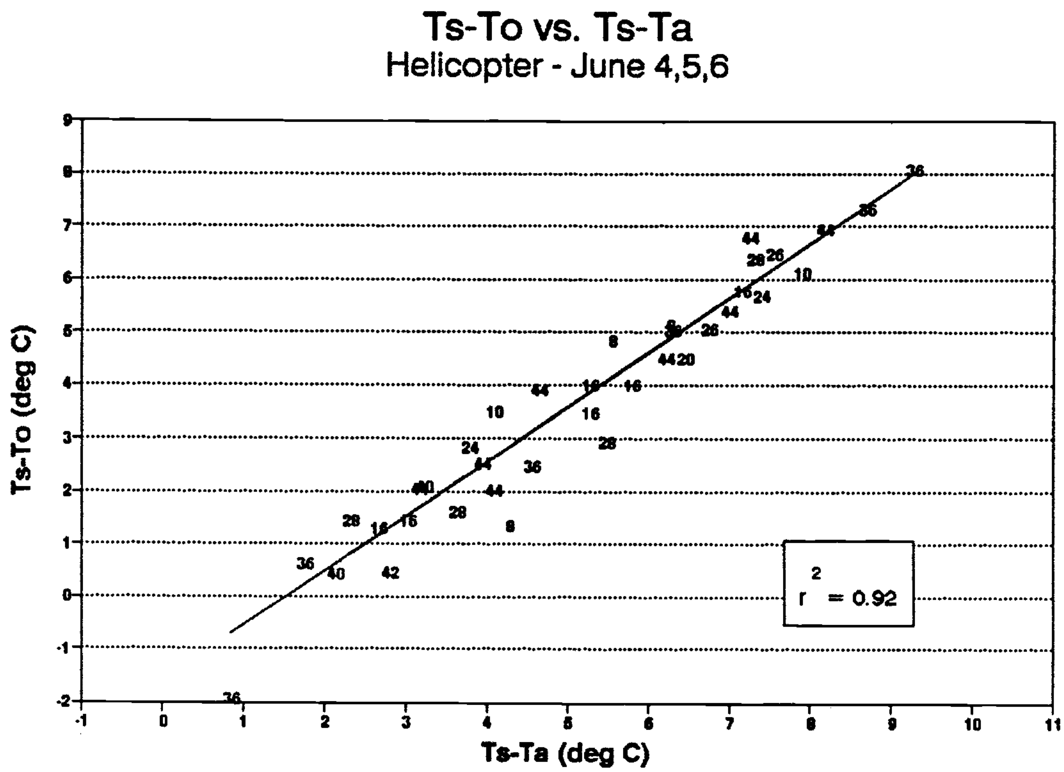

Figure 4.16. The difference between the surface temperature and aerodynamic temperature for various ground flux stations plotted as a function of the surface-air temperature difference estimated from helicopter-based remote sensing data during IFC1. Data labels refer to the various ground-based flux stations over which the data were acquired.

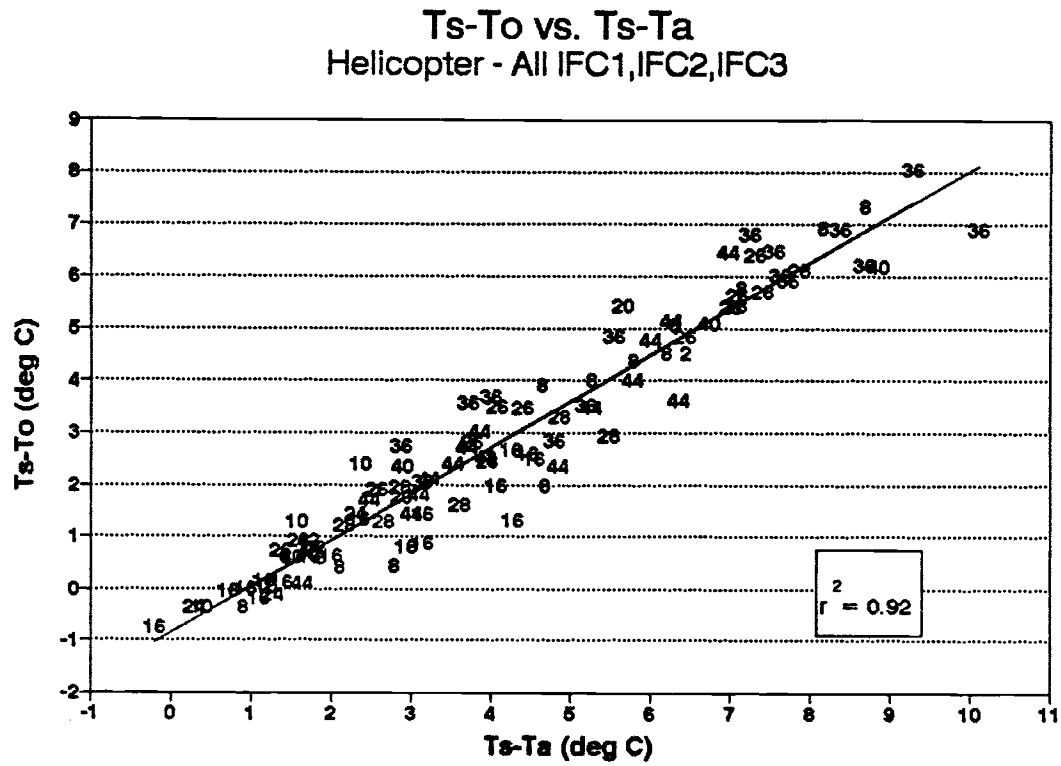

Figure 4.17. The difference between the surface temperature and aerodynamic temperature for various ground flux stations plotted as a function of the surface-air temperature difference estimated from helicopter-based remote sensing data during IFC1, IFC2, and IFC3. Data labels refer to the various ground-based flux stations over which the data were acquired.

canopy, and soil component temperatures, does appear to have a significant correlation with (T_s-T_o). Unfortunately, because the relationship between (T_s-T_o) and (T_s-T_a) is influenced by many factors, it is difficult to derive a rigorous physical relationship between them without knowledge of many surface parameters. It is useful, however, to observe the relationship between (T_s-T_o) and (T_s-T_a) under field conditions such as those in the FIFE experiment and to compare the estimates of sensible heat flux for the site which can be derived from Equations (4.12)-(4.14) with those estimates derived from other techniques. The results of that comparison are given in the next section.

Estimation of Sensible Heat Flux

For the data periods during IFC 3, the sensible heat flux was calculated using the surface temperature from the helicopter-based MMR data and ground estimates of air temperature and windspeed from each flux station. The sensible heat fluxes were estimated with three methods: (1) the method summarized in Chapter 1, which has been shown to work well over mature agricultural crops with ground-based remote sensing data (Reginato et al., 1985), aircraft-based remote sensing data (Jackson et al., 1987), and satellite-based remote sensing data (Moran et al., 1990), referred to as the "traditional" single layer method (given by Equations (4.6) with T_s used in place of T_o; 4.8-4.11), (2) the method described by Kustas et al. (1989a) and summarized above (given by Equations (4.6) with T_s used in place of T_o; 4.7-4.11), and (3) the method described above using the regression equations derived from data from the FIFE field site (Equations (4.6) and (4.14)). The estimates obtained by each of these methods are compared with the ground-based flux station measurements of sensible heat for the 30-minute periods which include the helicopter overpass times for a particular site. The data set includes points from about 10 different flux stations at different times of day, ranging from about 800 hr local time to 1400 hr local time. Most of the observations are in the midday period from about 1000 hr to 1400 hr local time.

The results for the traditional single layer method are shown in Figure 4.18. The solid line on the plot is the 1:1 line which would represent perfect agreement between the observed and the computed flux values. The RMSE for this method was 196 Wm^{-2}. The results for the method described by Kustas et al. (1989a) are shown in Figure 4.19. The RMSE for this method was 111 Wm^{-2}. The results for the method relating (T_s-T_o) to (T_s-T_a) using Equation (4.13) are shown in Figure 4.20. The results shown in Figure 4.20 are not intended to be interpreted as a validation of Equation (4.13) because these fluxes are computed with the same data set from which Equation (4.13) was derived. Rather, this computation is intended to quantify the level of uncertainty present in the estimation of fluxes in this data set with Equation (1.12). The RMSE value for this method was 31.7 Wm^{-2}.

Comparison of Helicopter and Satellite-Based Data

As described in the above section on experimental data, the digital numbers (DNs) for 2-5 pixels covering the area near most of the flux stations were extracted

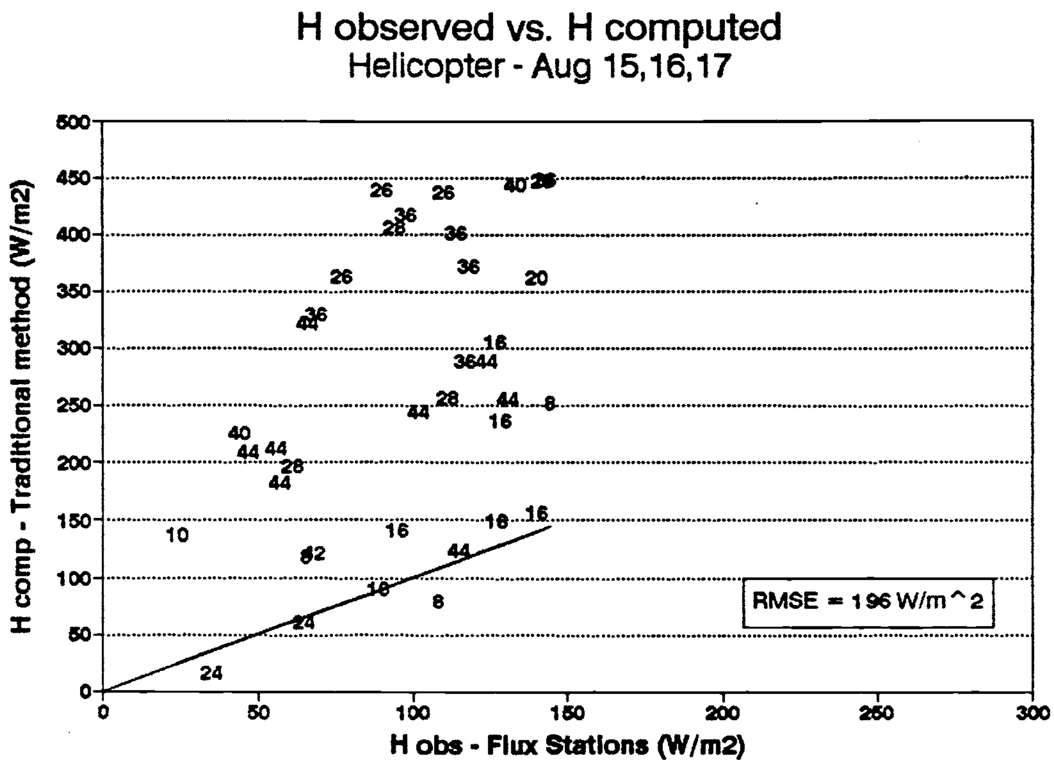

Figure 4.18. Sensible heat flux computed with helicopter remote sensing data using the traditional method developed over complete canopies plotted against the sensible heat flux observed at the ground-based flux stations. The data labels refer to the ground-based site number; the solid line is the 1:1 line.

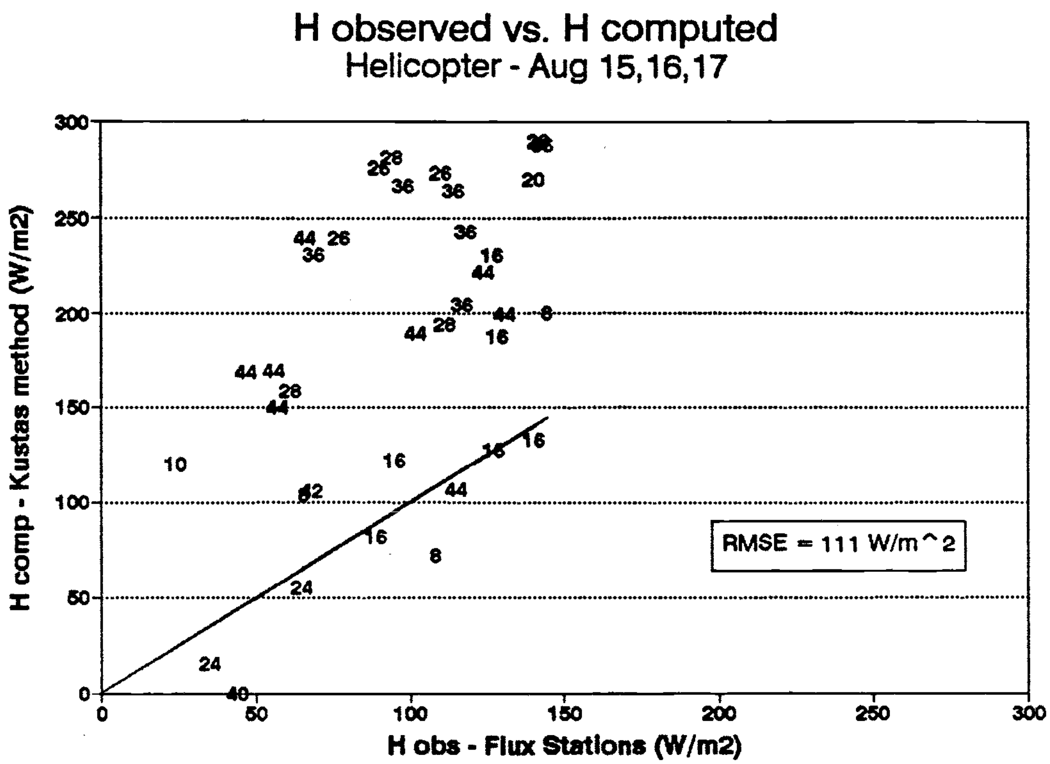

Figure 4.19. Sensible heat flux computed with helicopter remote sensing data using the method described by Kustas et al. (1989) plotted against the sensible heat flux observed at the ground-based flux stations. The data labels refer to the ground-based site number; the solid line is the 1:1 line.

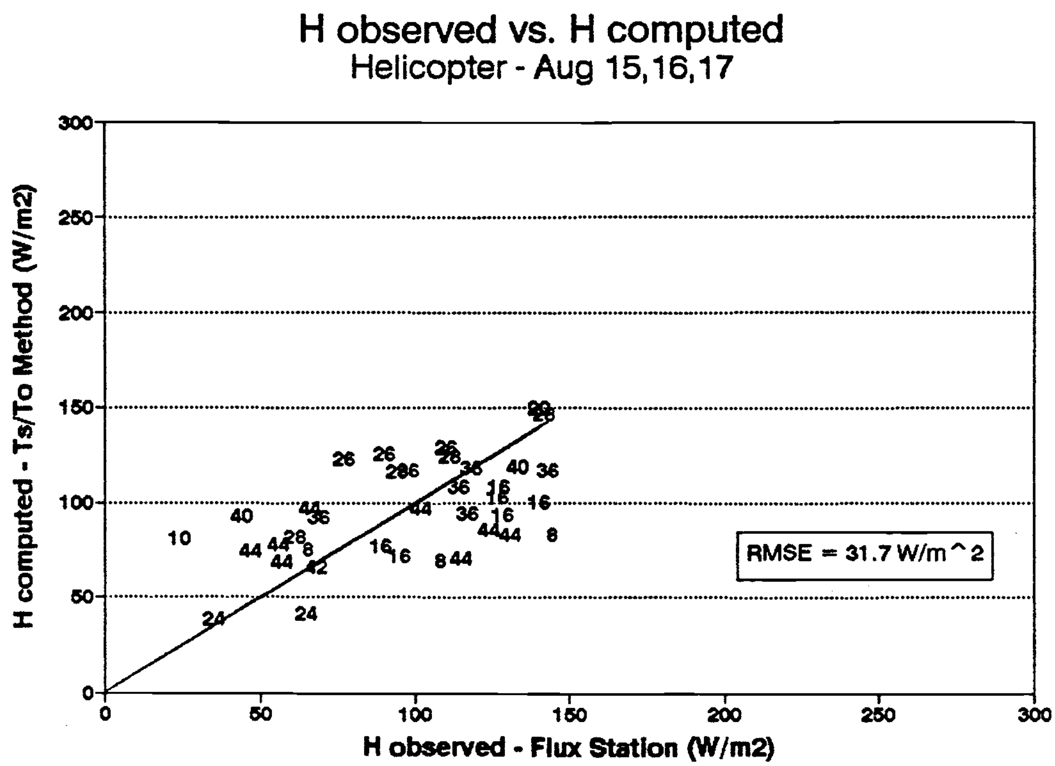

Figure 4.20. Sensible heat flux computed with helicopter remote sensing data using Equation (4.13) to estimate aerodynamic temperature from surface temperature, plotted against the sensible heat flux observed at the ground-based flux stations. The data labels refer to the ground-based site number; the solid line is the 1:1 line.

from each band of the Landsat TM image acquired over the FIFE site on August 15, 1987. The satellite overpass time was approximately 10:34 local time (Central Daylight Time). Sensor calibration coefficients and atmospheric corrections were applied to the satellite extract data by FIFE Information System personnel, but the procedures and results were carefully reviewed by this author in an attempt to understand sources of error in the differences between helicopter- and satellite-based reflectances and temperatures and to assure that identical corrections could be applied to the 512 x 512 pixel image used in the analysis presented in the next chapter. Because the results of the analysis in this chapter and in Chapter 5 are more dependent on the quantitative integrity of the satellite data in the thermal band than in the reflective bands, the corrections applied to the thermal data will be discussed in more detail than those applied to the data in TM1-TM4.

Calibration and Atmospheric Corrections to Thermal Band

The calibration coefficients given by Markham and Barker (1986) were applied to the DNs from the satellite extract data to convert the DNs to at-satellite spectral radiance, L_s, given by:

$$L_s = 5.6322 \times 10^{-3}(DN) + 0.1238, \tag{4.15}$$

where L_s is in units of mW cm^{-2} sr^{-1} μm^{-1} and is multiplied by a factor of 10 in order to convert to units of Wm^{-2} sr^{-1} μm^{-1}. Next, the values of apparent at-satellite radiance were converted to surface radiance by correcting for the atmospheric effects of the intervening atmosphere. For data in the thermal band, the primary effects of the atmosphere are due to water vapor. There are two major effects: (1) the additional radiance (usually called path radiance) put into the path between the surface and the sensor due to emission by water vapor in the atmosphere, and (2) the absorption of the radiant energy from the surface by the water vapor present along the path. The amount of path radiance and the transmission of radiant energy through the atmosphere in the TM thermal waveband can be estimated in a number of ways. Standard surface models of atmospheric humidity and temperature profiles can be used in conjunction with atmospheric radiative transfer codes to compute standard values for path radiance and transmission, or measurements of the profile or columnar water vapor content on the day of interest can be used as input to a radiative transfer code to obtain special coefficients for the day of the overpass. The correct surface radiance, L_g, can be expressed as:

$$L_g = (L_s - (L_p/NB))/\tau, \qquad (4.16)$$

where L_p is the path radiance computed by one of the methods described above, NB is the normalized bandpass for the sensor, which corrects the upwelling radiance for the instrument response, (NB = 1.8481 for Landsat 5), and τ is the atmospheric transmittance computed by one of the methods described above. The expression described above neglects the effect of reflected downwelling radiation in the thermal band, which is usually small compared to the other terms in Equation (4.16) and the uncertainty in the atmospheric parameters.

The corrected surface radiance is then converted to surface temperature by inverting the integration of the Planck function over the wavelength interval of the TM bandpass. This process can be approximated by the expression:

$$Ts' = K2/\ln\left((K1/L_g) + 1\right). \tag{4.17}$$

T_s is the surface temperature uncorrected for emissivity (°K), and K1 are constants dependent on the instrument bandpass. For Landsat 5 TM, those coefficients are: K1 = 607.76 $Wm^{-2}\ sr^{-1}\ \mu m^{-1}$ and K2 = 1260.56°K. Last, the surface temperature was corrected for surface emissivity with the expression:

$$T_s = T_s'/(\epsilon^{1/4}). \tag{4.18}$$

Equation (4.18) implicitly assumes the Stefan-Boltzman relationship between radiance and surface temperature, $L_g = \epsilon_s \sigma T_s^4$, where σ is the Stefan-Boltzman constant ($5.674 \times 10^{-8} W\ m^{-2}\ {}^{\circ}K^{-4}$). The Stefan-Boltzman relationship was derived by integrating the Planck function from wavelength intervals 0 to ∞ and is thus only an approximation when applied to finite wavelength intervals. However, Slater (1980) showed that, for the TM bandpass over the range of surface temperatures for mid-summer mid-latitude land surfaces, the Stefan-Boltzman relationship is a reasonably good approximation to the Planck function. Because Equation (4.17) was used to convert the ground radiance to surface temperature, the Stefan-Boltzman relationship was only used to correct that temperature for the effects of surface emissivity.

In order to obtain the path radiance and transmittance values for August 15, 1987, FIFE Information System staff reduced the on-site radiosonde data available for that day and used them as input into the Lowtran7 radiative transfer code. They also computed the path radiance and transmission by running the Lowtran7 midlatitude summer model for the specific observing geometry on August 15, 1987. It was decided (Goetz, Personal Communication, 1991) that the path radiance and transmission values computed for that day with the Lowtran7 midlatitude summer model were superior to the values computed using the radiosonde data as input. This is unusual because on-site atmospheric profile data generally give more accurate estimates of the path radiance and transmittance for particular conditions on a particular day than does the standard model. The value of path radiance computed from the midlatitude summer model was 4.23 $Wm^{-2}\ sr^{-1}\ \mu m^{-1}$. The atmospheric transmittance was computed to be 0.682.

To test the quality of the atmospheric correction provided by the midlatitude summer model, the surface temperatures from the few helicopter MMR observations (6 sites) which were within approximately +/- 15 minutes of the satellite overpass on August 15, 1987 were compared with the surface temperatures estimated from the satellite extract data. The satellite surface temperatures obtained by applying the path radiance and transmission from the midlatitude summer model were all biased approximately 6 degrees higher than the helicopter-based surface temperatures. The values of path radiance and atmospheric transmittance were reduced and increased, respectively, by equal percentages until the differences in the satellite-derived surface temperatures and the helicopter-based surface temperatures for all 6 sites were minimized. This yielded a new path radiance of 3.47 $Wm^{-2}\ sr^{-1}\ \mu m^{-1}$ and a transmittance value of 0.805. The results of the comparison in surface temperatures after that optimization are shown in Figure 4.21. The data points in the figure are labeled with the site number designations for the flux stations over which helicopter-based data were acquired nearly simultaneously with the satellite overpass. There is an RMSE between the satellite- and helicopter-based temperatures of 1.2°K.

Calibration and Atmospheric Corrections for Reflectance Bands

As discussed in the experimental data section above, the conversion of the Landsat TM DNs in Bands 1-5 and 7 to apparent at-satellite radiance (L_s) was done with gain and offset coefficients provided by EOSAT, as opposed to using the absolute radiometric calibration reported by Slater et al. (1986), which would require that the CCT format radiometric corrections be reversed. Next, the apparent at-satellite radiance is converted to exoatmospheric reflectance, ρ_{exo}, with the following expression given by Markham and Barker (1986):

$$\rho_{exo} = (\pi * L_s)/F_o' * \cos(\theta_z). \tag{4.19}$$

$F'_o = F_o/R^2$, where F_o is the extraterrestrial solar irradiance in the TM bandpass (W m^{-2} sr^{-1} μm-1), R = d/d', where d = the Earth-sun distance in astronomical units, and d' is the average Earth-sun distance in astronomical units. The values of F_o for the Landsat 5 TM1, TM2, TM3, TM4, TM5, and TM7 bandpasses are given in Markham and Barker (1986). θ_z is the solar zenith angle at the time of the observation.

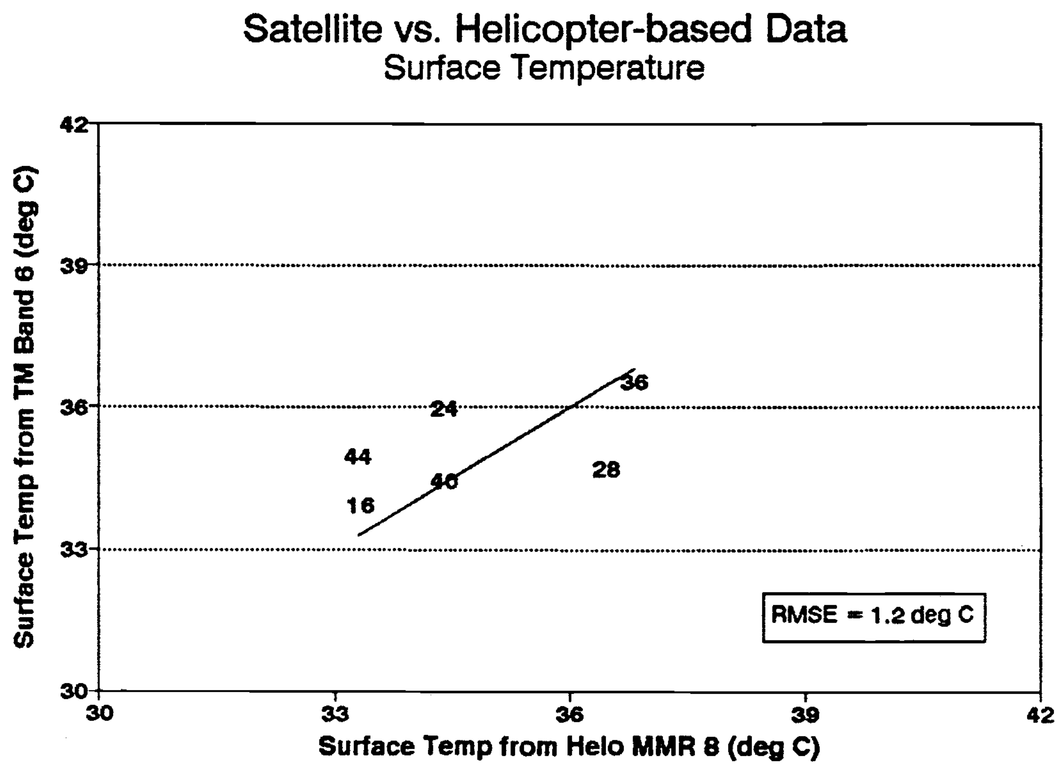

Figure 4.21. Surface temperature estimated from atmospherically corrected TM Band 6 pixels near ground flux stations plotted against surface temperature measured near-simultaneously with the helicopter based MMR. The atmospheric corrections were adjusted to minimize the error between the helicopter and satellite-based surface temperatures. Data labels refer to ground-based flux site numbers.

The FIFE Information System personnel evaluated various measurements of optical depth available over the FIFE site on August 15, 1987 and calculated the aerosol optical thickness for the TM bandpasses. Optical thickness measurements were interpolated to the TM bandpasses using a linear fit of the log of wavelength regressed against the log of optical thickness. TM bandpass model wavelengths were calculated as described in Fraser et al. (1989). The total column water vapor and gaseous absorption profiles were calculated using the Lowtran7 midlatitude summer model. The ground-level downward irradiance, upward radiance, and surface reflectance in the TM bandpasses were computed using the algorithm described in Fraser et al. (1989). The normalized surface irradiance and backscattering ratio computed by the algorithm were output and provided as coefficients for correcting other image pixels (FIFE Information System, Landsat TM Reflectance, Level 2 Description and Documentation).

Comparisons of the satellite-derived surface reflectances computed by the procedure summarized above with the helicopter-based MMR surface reflectances for TM/MMR Band 3 and TM/MMR Band 4 are shown in Figures 4.22 and 4.23, respectively. The solid lines on both plots are the 1:1 lines. The Band 3 satellite reflectances appear to be slightly biased to be lower than the helicopter-derived surface reflectances, but the absolute difference in reflectance is quite small. The comparison of satellite-derived and helicopter-derived reflectances for Band 4 do not agree as well as those in Band 3. This is somewhat surprising because atmospheric effects on the satellite data in Band 4 should be less than those in Band 3. Given

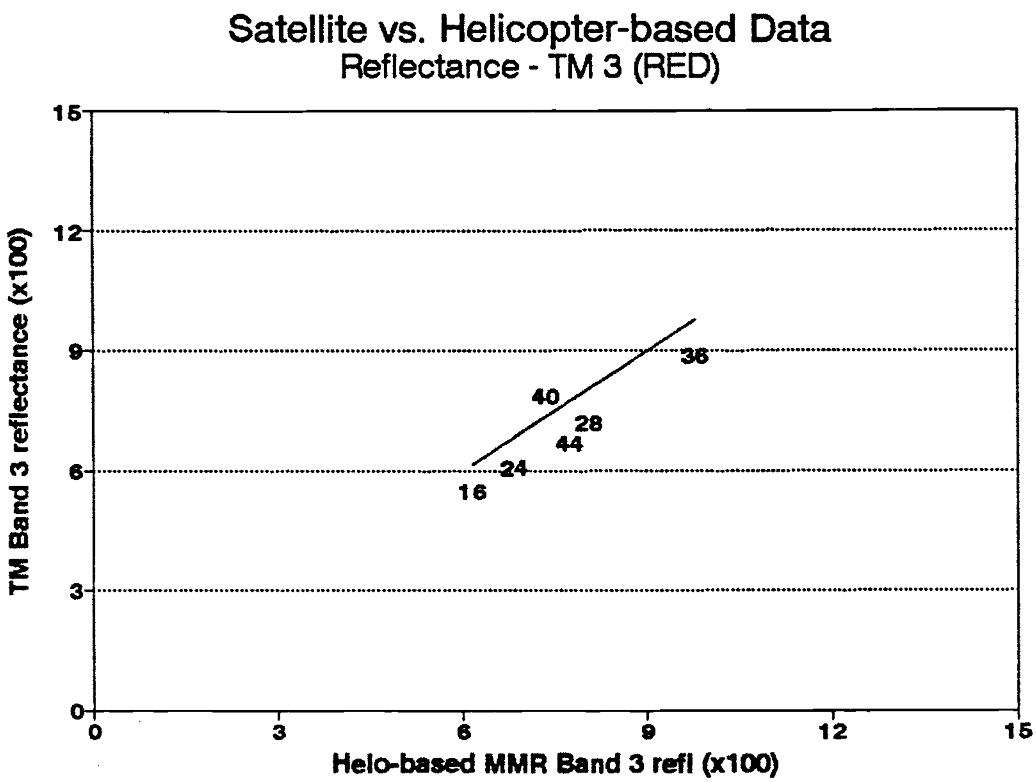

Figure 4.22. Surface reflectance computed from atmospherically corrected TM Band 3 (RED) pixels near ground flux stations, plotted against surface reflectance derived from nearly simultaneous helicopter-based MMR measurements. Data labels refer to the ground-based flux site numbers.

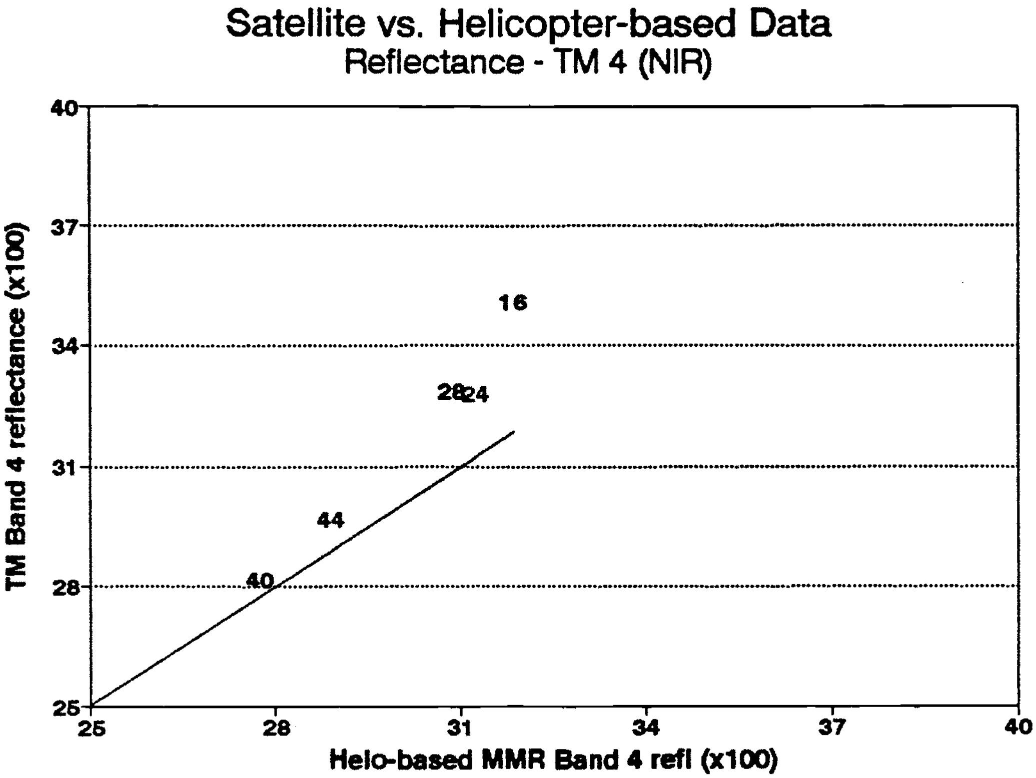

Figure 4.23. Surface reflectance computed from atmospherically corrected TM Band 4 (NIR) pixels near ground flux stations, plotted against surface reflectance derived from nearly-simultaneous helicopter-based MMR measurements. Data labels refer to the ground-based flux site numbers.

the uncertainty and scatter in the relationships between vegetation indices and fluxes for which these reflectance values will be used in this analysis, the disagreement shown by the data in Figure 4.23 is not likely to be a significant source of error.

Estimation of Fluxes with Satellite-based Data

The values of the surface energy-balance components and meteorological data from the flux stations operating during the time of the Landsat overpass at 10:34 (CDT) and used for comparison to satellite-derived fluxes are summarized in Table 4.2. The fluxes and meteorological data represent 30-minute averages at the ground-based sites. Daily soil moisture values and weekly vegetation parameter estimates are also included in Table 4.2.

Soil Heat Flux

The values of $G/R_{net,total}$ from the 13 ground-based stations for which flux values are reported during the TM overpass time are plotted versus the NDVI computed from the satellite-derived reflectances shown in Figure 4.24. The labels on the data points refer to ground station site numbers. The upper solid line is the regression line computed from the satellite data shown; the lower solid line is the regression line calculated for the IFC 3 data from the helicopter data presented in the previous section. The two regression lines have very similar slopes but appear to be offset from each other. This is most likely due to slightly higher values of NDVI for the satellite-derived data which may result from uncertainties in the

Table 4.2. Half-hourly Flux Station Data Near TM Overpass Time on 8/15/87. Daily values for soil moisture and weekly vegetation parameters.

Site	R_{net}	G (W/m^2)	H (W/m^2)	LE (W/m^2)	T_{air} (W/m^2)	Vap Pres (C)	Wind (kPa)	LAI (m/s)	Canopy Ht (m)	Soil Moisture Frac.*
8	541	-54	-144	-343	32.3	2.59	4.5	0.8	0.47	0.84
14	550	-26	-187	-337	32.8	2.57	4.3	1.0	0.50	0.69
16	529	-55	-140	-334	32.1	2.71	6.0	1.4	0.56	0.82
20	566	-48	-209	-309	32.1	2.58	4.0	0.9	0.78	0.74
22	530	-72	-117	-351	31.8	2.56	4.9	0.6	0.30	0.80
24	596	-103	-65	-427	33.3	2.72	4.3	0.4	0.18	0.88
26	564	---	-131	-332	31.4	2.62	7.1	0.3	0.24	0.79
28	521	-69	-142	-241	31.6	---	5.5	0.6	0.40	0.85
34	536	-113	-150	-273	32.2	1.78	4.2	0.9	0.40	0.86
36	558	-118	-117	-324	32.2	2.54	4.8	0.3	0.20	0.80
38	593	-129	-97	-368	31.9	2.97	5.0	0.4	0.28	0.80
40	539	-64	-25	-450	32.6	2.90	4.8	0.5	0.32	0.83
42	543	-53	-98	-393	31.6	2.68	2.7	1.1	0.40	0.97
44	553	-64	-120	-351	32.3	1.21	3.5	0.5	0.38	0.87

* Soil Moisture Frac. is computed as the observed gravimetric soil moisture divided by the value of soil moisture at saturation.

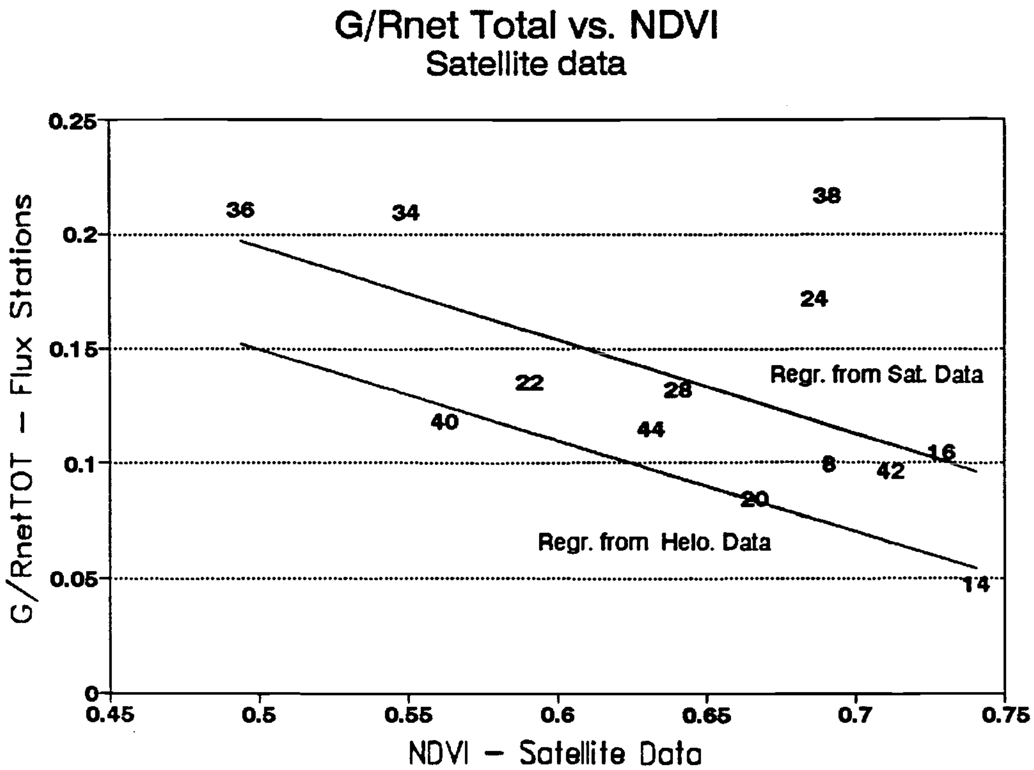

Figure 4.24. Ratio of G/Rnet,total measured at ground flux sites plotted against NDVI values derived from the satellite pixels near the ground-based flux sites. The data labels refer to the ground-based site number. The upper solid line represents the regression line for the data shown; the lower solid line represents the regression equation for these same quantities derived from helicopter-based NDVI values.

atmospheric correction of the TM Band 4 data. Furthermore, there is considerable scatter in the relationship between the ratio of $G/R_{net,total}$ from the flux stations and the NDVI, due primarily to the data at one or two flux stations. The relationship derived from the satellite-based data is:

$$G/R_{net,total} = 0.40 - 0.41*(NDVI). \tag{4.20}$$

The same data and the regression line computed with these data points are shown again in Figure 4.25, but the upper solid line shown in this figure is the regression equation derived by Kustas and Daughtry (1990) over bare soil, cotton, and alfalfa fields with ground-based remote sensing data. The slope of the equations appears to be substantially different. This is probably due to significant differences in the structure and density of the grassland vegetation and the agricultural crops for which the Kustas and Daughtry relationship was developed. These relationships need to be further evaluated over various surface types to determine how much the relationship varies between different vegetation types under different conditions.

Surface Temperature and Aerodynamic Temperature

The relationship between $(T_s\text{-}T_o)$ and $(T_s\text{-}T_a)$ was evaluated using data from the ground-based surface flux stations and the satellite-derived surface temperatures. The results are shown in Figure 4.26. The correlation between $(T_s\text{-}T_o)$ and $(T_s\text{-}T_a)$ using the satellite-derived surface temperatures is quite good, with the exception of

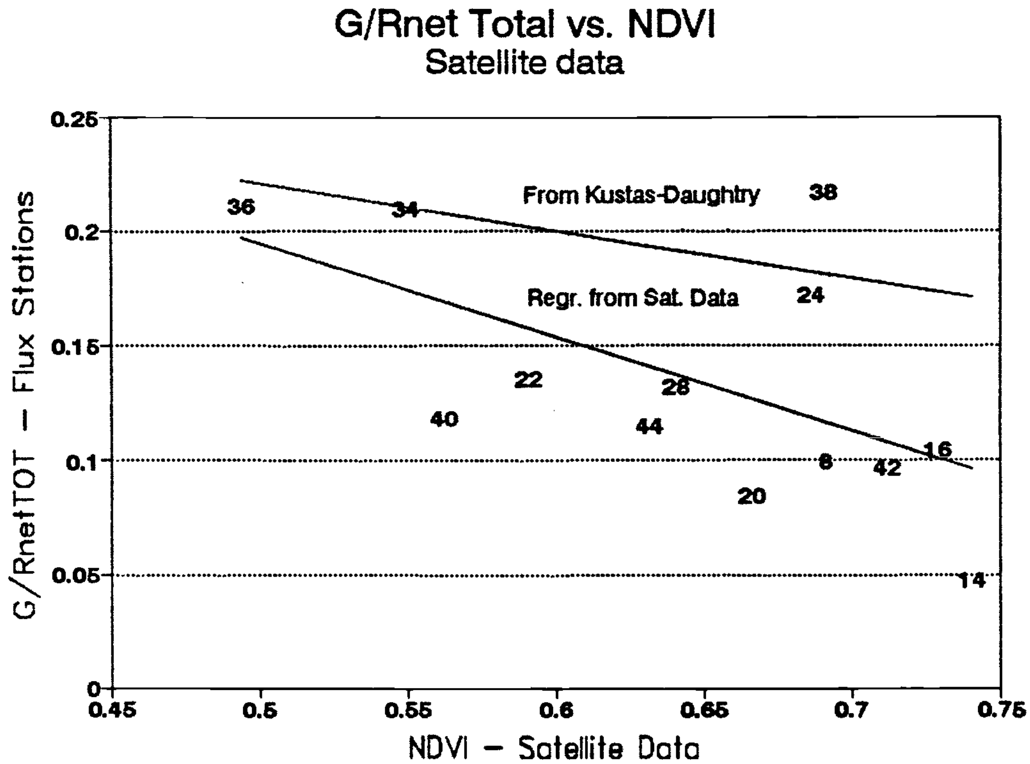

Figure 4.25. Ratio of G/Rnet,total measured at ground flux sites plotted against NDVI values derived from the satellite pixels near the ground-based flux sites. The data labels refer to the ground-based site number. The upper solid line represents the regression equation for these same quantities derived by Kustas and Daughtery (1990) over cotton and alfalfa; the lower solid line represents the regression equation for the data shown.

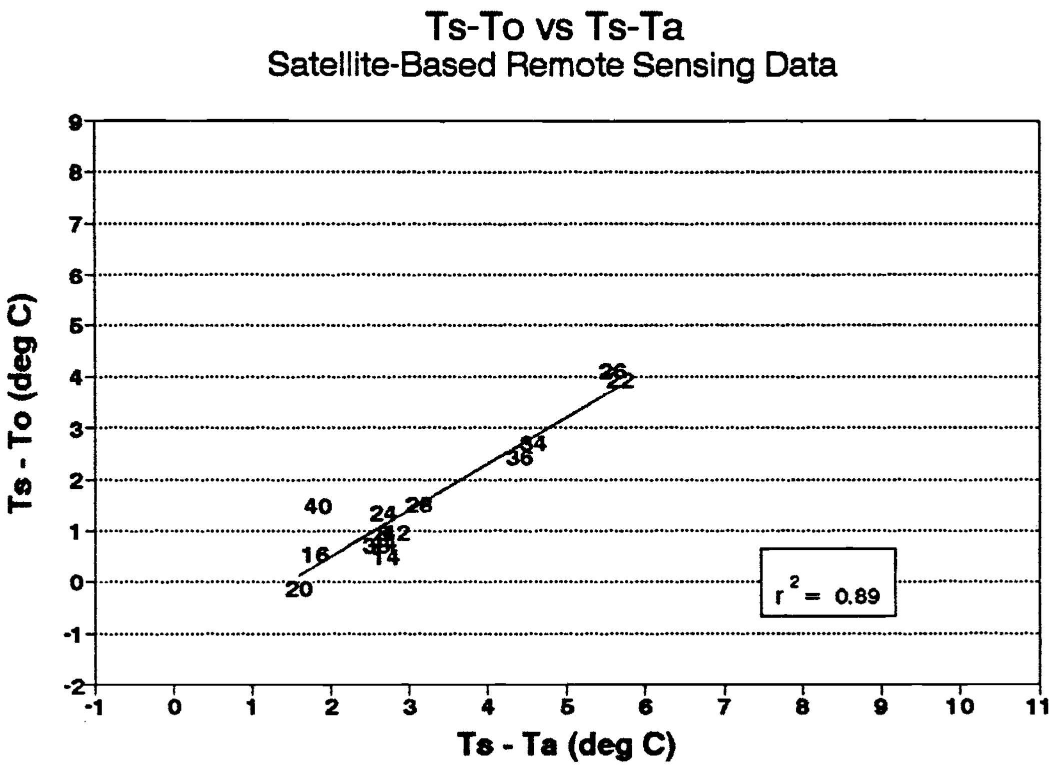

Figure 4.26. The difference between the surface temperature and aerodynamic temperature for various ground flux stations plotted as a function of the surface-air temperature difference estimated from satellite pixels over various ground sites for the August 15 TM overpass. The regression lines derived for these quantities from both the satellite and helicopter-based data are also shown.

one outlying point (Site 40). The regression equation between $(T_s\text{-}T_o)$ and $(T_s\text{-}T_a)$ is slightly different from that derived from the helicopter-based data:

$$(T_s - T_o) = -1.29 + 0.90\,(T_s - T_a). \tag{4.21}$$

Sensible Heat Flux

The same three techniques described above used to estimate sensible heat flux from the helicopter-based surface temperatures were used to estimate sensible heat flux with the satellite-based surface temperatures. The results of the three methods were compared with sensible heat fluxes measured at the ground-based flux sites and are shown in Figures 4.27, 4.28, and 4.29. The results for the traditional method developed and validated over nearly full cover agricultural crops are shown in Figure 4.27. The solid line is the 1:1 line representing perfect agreement between the satellite-derived estimates of sensible heat flux and the sensible heat flux estimates observed from the ground-based flux stations. The RMSE between the flux station estimates and the satellite-derived estimates for this method was 159 Wm^{-2}. The results for the method described by Kustas et al. (1989a) are shown in Figure 4.28. The RMSE for this method was 79.1 Wm^{-2}. The results for the method in which the $(T_s\text{-}T_o)$ difference is estimated from the observed $(T_s\text{-}T_a)$ and Equation (4.21) are shown in Figure 4.29. The RMSE between the ground station fluxes and the satellite-derived fluxes for this method was 33.3 Wm^{-2}. As before, the results shown in Figure 4.29 do not represent a validation of Equation (4.21) but rather an

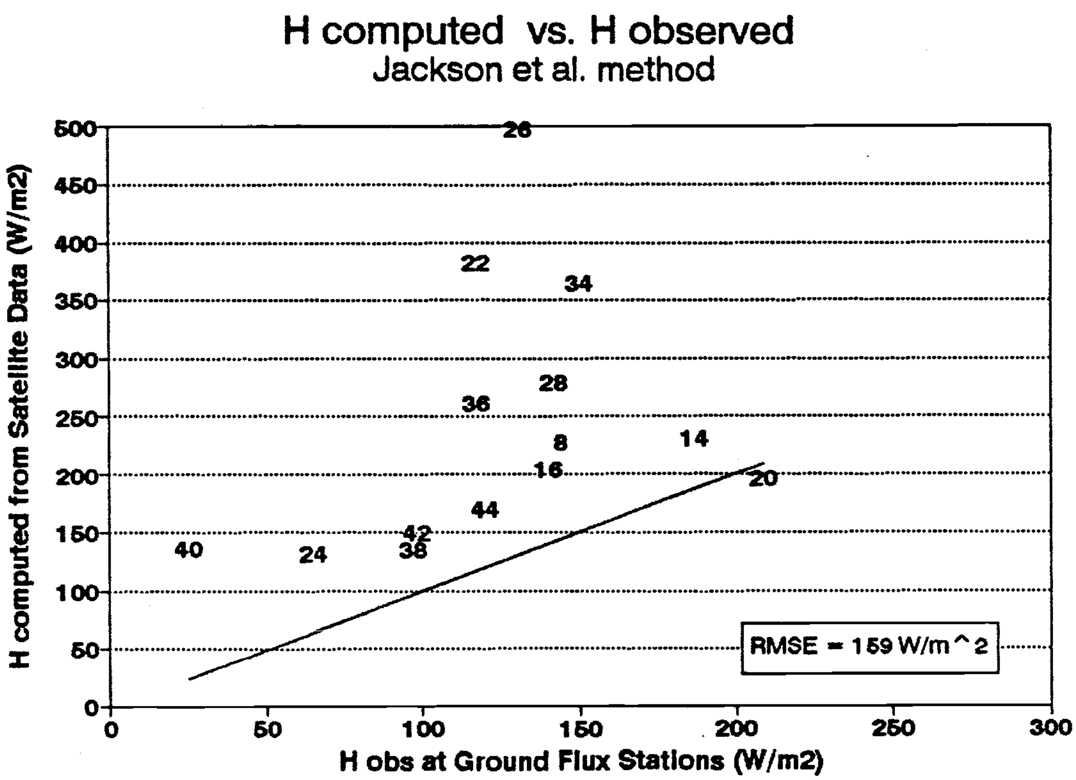

Figure 4.27. Sensible heat flux computed with satellite-derived surface temperatures using the traditional method developed over complete canopies, plotted against the sensible heat flux observed at the ground-based flux stations. The data labels refer to the ground-based site number; the solid line is the 1:1 line.

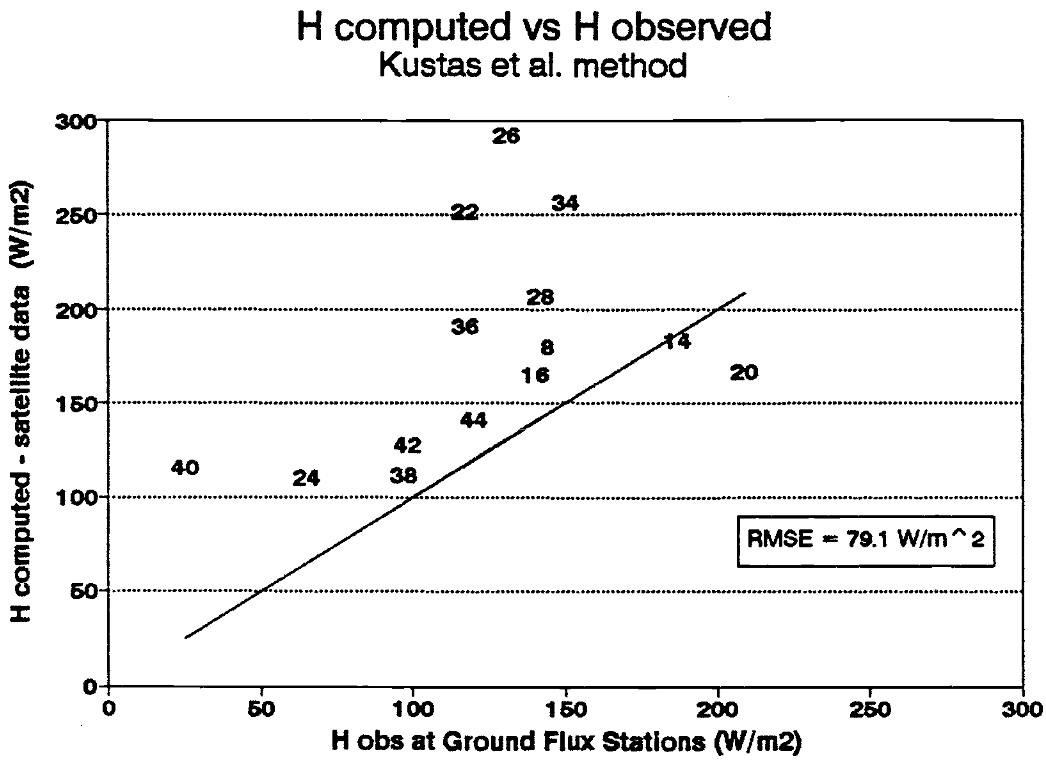

Figure 4.28. Sensible heat flux computed with satellite-derived surface temperatures using the method described by Kustas et al. (1989) plotted against the sensible heat flux observed at the ground-based flux stations. The data labels refer to the ground-based site number; the solid line is the 1:1 line.

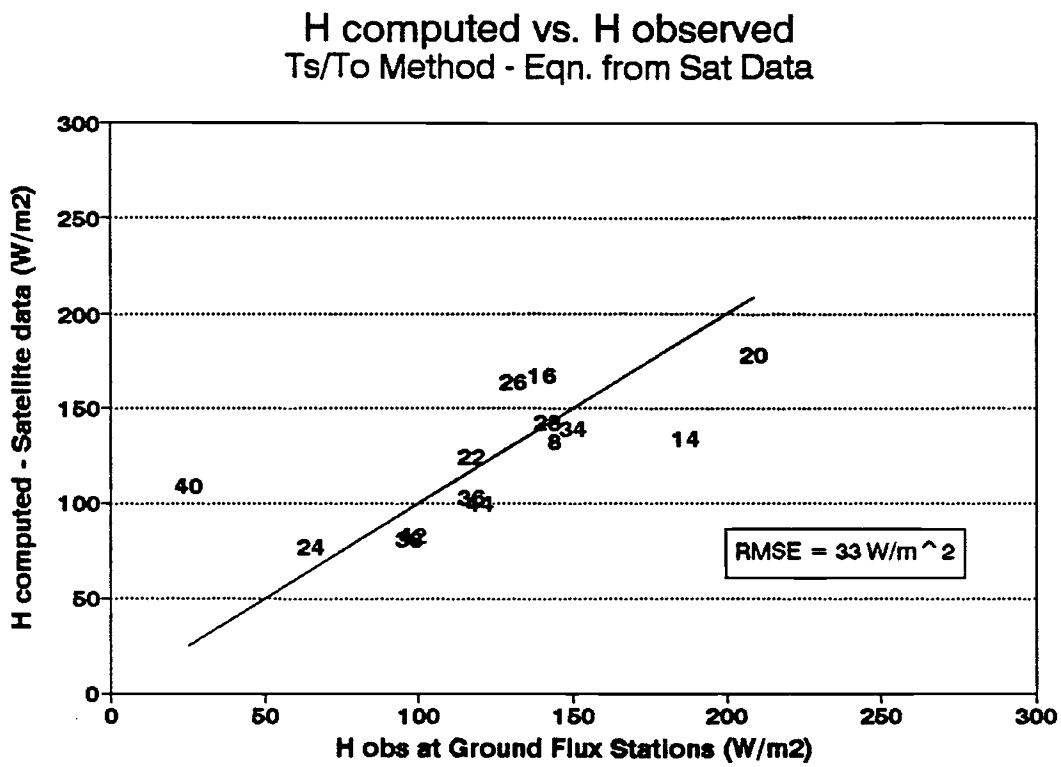

Figure 4.29. Sensible heat flux computed with satellite-derived surface temperatures and Equation (4.21) to estimate aerodynamic temperature from surface temperature, plotted against the sensible heat flux observed at the ground-based flux stations. The data labels refer to the ground-based site number; the solid line is the 1:1 line.

assessment of the level of error with which the equation provides estimates of sensible heat flux for the site.

Summary

Values of reflectance and temperature measured with a helicopter-based MMR compared very favorably with ground-based measurements of reflectance and temperature taken nearly simultaneously at several FIFE ground stations over a range of dates and times during the FIFE 1987 IFCs. The values of reflectance and temperature estimated with atmospherically corrected extracts from a Landsat TM scene for August 15, 1987 compared well with nearly simultaneous data acquired with helicopter- and ground-based sensors only after a significant adjustment was made to atmospheric correction for the data in the thermal band. Regression equations were developed which related the ratio $G/R_{net,total}$ measured at the ground-based flux stations with remotely sensed vegetation indices. Using the values of sensible heat flux measured at 12 ground-based flux stations over the FIFE site, together with helicopter- and satellite-based surface temperatures, regression equations were also developed which described the relationship between the surface-air temperature difference (T_s-T_a) and the difference between surface temperature and aerodynamic temperature (T_s-T_o). The values of sensible heat flux computed with the regression equations described above yielded significantly better estimates of sensible heat flux than standard techniques described by Jackson et al. (1985) for complete vegetation cover.

Conclusions

In conclusion, it is somewhat discouraging that attempts to define relationships between the aerodynamic temperature, surface temperature measured with remotely sensed instruments, and physical surface parameters that would be expected to influence the difference between these two temperatures were not very successful. Realistically, however, it should not be surprising that the complex physical processes and many factors which influence the aerodynamic temperature of a partially vegetated surface could not be captured with the multispectral response acquired in a single remote sensing observation of a particular surface. Future sensors which provide near-simultaneous observations of the surface in optical and thermal wavebands at various view angles possibly will provide enough information to allow for inverse modeling solutions to more physical surface parameters. From a pragmatic standpoint, however, the data that will be available from most satellite-based sensors in the near future will provide optical and thermal observations at only one view angle.

For the immediate objectives of the research described in this dissertation, the analysis described here was successful in identifying expressions with which to describe the soil heat flux and sensible heat flux for the FIFE site using a combination of ground-based data and remotely sensed satellite data. These expressions will be used in the next chapter to generate a spatially distributed map of surface fluxes for the entire FIFE experimental site.

CHAPTER 5

PRODUCTION OF SPATIALLY DISTRIBUTED MAPS OF SENSIBLE AND LATENT HEAT FLUX OVER THE FIFE SITE

Introduction

Estimates of the spatially distributed fluxes of moisture and energy from the land surface are a useful tool for better understanding the spatial variability of the water balance as well as the interactions between the land surface and the atmospheric boundary layer. Such surface flux estimates can be used as spatially distributed boundary conditions for coupled surface/atmosphere models. A Landsat 5 TM image from August 15, 1987 (overpass time of 11:34 a.m. Central Daylight Time) was used in combination with ground-based measurements of near-surface temperature, windspeed, and vapor pressure to create a spatially distributed map of soil heat flux, sensible heat flux, and latent heat flux for the FIFE experimental site.

Strategy

The components of the surface energy balance are related by the energy-balance equation, which can be written as:

$$R_{net} = G + H + LE, \tag{5.1}$$

where R_{net} is the net radiation at the surface, G is the soil heat flux, H is the sensible heat flux, and LE is the latent heat flux, all in units Wm^{-2}. As described in Chapter 1, the overall strategy employed in estimating the components of the surface energy balance with remotely sensed data is to estimate the R_{net}, G, and H terms with a combination of ground-based and remotely sensed data. The latent heat flux component is then estimated as the residual quantity in Equation (5.1). The methodology for computing the magnitude of the R_{net}, G, and H terms in Equation (5.1) for the time of the Landsat TM overpass on August 15, 1987 is summarized below.

Net Radiation

The net radiation, R_{net}, is estimated with a combination of ground-based and remotely sensed data by considering the four major components of net radiation, given by:

$$R_n = R_{s\downarrow} - R_{s\uparrow} + R_{l\downarrow} - R_{l\uparrow}, \tag{5.2}$$

where $R_{s\downarrow}$ is incoming solar (from approximately 0.15 to 4 μm) radiation, $R_{s\uparrow}$ is the outgoing (reflected) solar radiation, $R_{l\downarrow}$ is the incoming emitted long-wave (approximately 4 μm to 1000 μm) radiation from the sky, and $R_{l\uparrow}$ is the outgoing terrestrially emitted long-wave radiation, all in units of Wm^{-1}.

Dubayah et al. (1990) computed $R_{s\downarrow}$ for each pixel in the Landsat TM image by using ground-based estimates of solar irradiance together with digital elevation data. The data were used as input into an algorithm which searches the horizon at each pixel to determine any shadowing effects on each pixel in the image at the solar zenith and azimuth angle of the TM overpass time. Using this information, together with the slope of each pixel, the value for $R_{s\downarrow}$ was estimated for each pixel. The outgoing solar radiation was computed with atmospherically corrected data from TM bands 1-5 and 7, using a modification of the method described by Jackson (1984). The remotely sensed estimates of net solar radiation were validated by comparison with the ground-based flux station estimates. The difference in $R_{s\downarrow}$ and $R_{s\uparrow}$ is referred to as $R_{net,solar}$.

The $R_{net,solar}$ image provided by Dubayah et al. (1990) was corrected for the effects of incoming and outgoing long-wave radiation. The incoming long-wave radiation was estimated from ground-based measurements of air temperature and vapor pressure, using the expression:

$$R_{l\downarrow} = \epsilon_a \sigma T_a^4, \tag{5.3}$$

where ϵ_a is the emissivity of the air, given by $\epsilon_a = 1.24(e_a/T_a)^{1/7}$ (Brutsaert, 1975), σ is the Stefan-Boltzman constant ($Wm^{-2}K^{-4}$), T_a is the air temperature, and e_a is the vapor pressure (mb). The outgoing long-wave radiance, $R_{l\uparrow}$, is estimated from the expression:

$$R_{l\uparrow} = \epsilon_s \sigma T_s^4, \tag{5.4}$$

where T_s is the remotely sensed surface temperature, and ϵ_s is the emissivity of the surface used to compute the surface temperature from the satellite data.

Soil Heat Flux

From the analysis of ground-based data from flux stations and extracts of the Landsat TM image described in the previous chapter, a relationship between the soil heat flux and net radiation was evaluated in terms of a vegetation index. That relationship was found to be given by the expression:

$$G/R_{net,total} = 0.40 - 0.41*(NDVI), \tag{5.5}$$

where NDVI is the Normalized Difference Vegetation Index given by Equation (4.2).

Sensible Heat Flux

From analysis of data from ground flux stations and satellite extracts described in the previous chapter, the difference between the aerodynamic temperature and the surface temperature was found to be related to the surface-air temperature difference. That relationship was described by the expression:

$$T_o = T_s - 1.29 + 0.90*(T_s - T_a). \quad (5.6)$$

T_s is the surface temperature estimated from the satellite data, T_a is the air temperature near the surface, and T_o is the aerodynamic temperature. The relationship between aerodynamic temperature and sensible heat flux is given by:

$$H = \rho C_p (T_o - T_a)/r_a, \quad (5.7)$$

where H is the sensible heat flux (W/m^{-2}), ρC_p is the heat capacity of air ($Jm^{-3}C^{-1}$), T_o is the aerodynamic temperature, T_a is the air temperature at a reference height above the canopy, and r_a (sm^{-1}) is the aerodynamic resistance to heat transfer. The stability corrected aerodynamic resistance is computed as a function of canopy height and windspeed at a reference height above the surface, as described by Equations (4.9) and (4.10).

Ground-Based Inputs

Air Temperature

The near-surface air temperature is used in the calculation of the incoming long-wave radiation term in the net radiation flux and the estimation of the sensible heat flux. The values of air temperature reported at the ground-based flux stations and automatic meteorological stations for the half-hourly time period which included the TM overpass are shown in Figure 5.1. The x and y coordinates in Figure 5.1 represent the UTM coordinate positions of the ground-based stations within the FIFE experimental site. The labels on the data points represent the air temperature

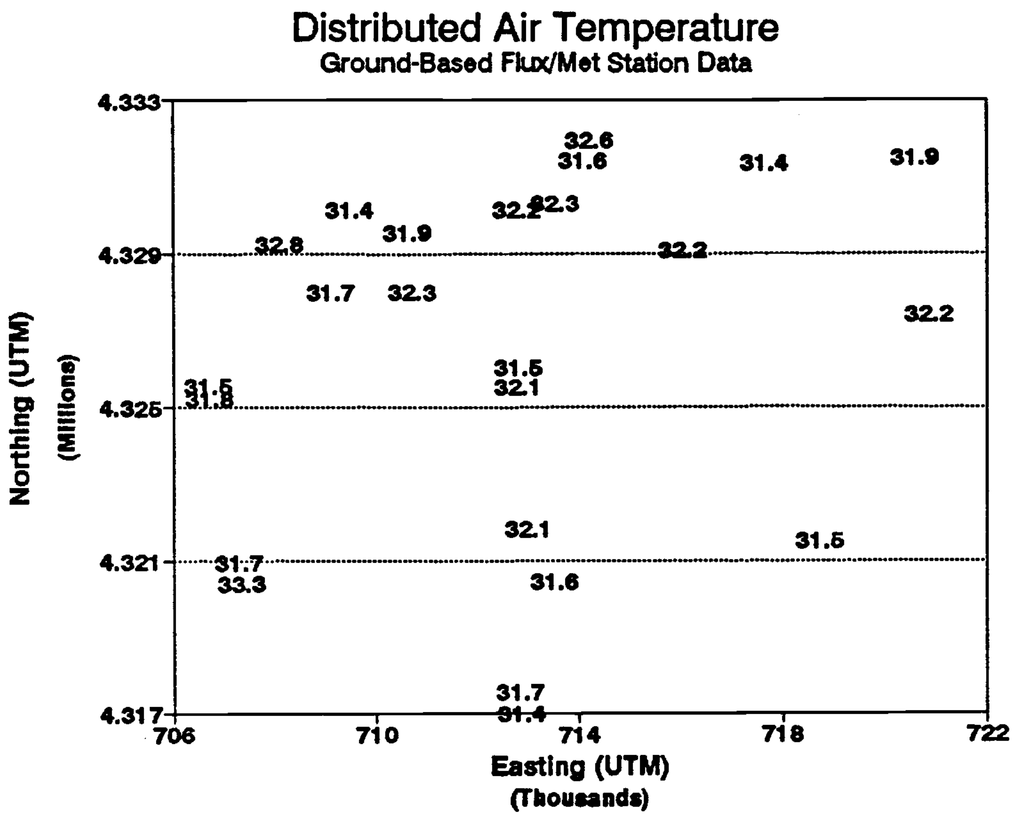

Figure 5.1. The values of air temperature reported at the ground-based flux stations and meteorological stations plotted at the approximate spatial location of the station on the FIFE experimental site. The temperatures are given in °C and most measurements were taken at a height of approximately 2 meters above the surface.

measured at the ground sites. The instrument height above the surface was not the same for all stations, but at most stations the instruments were positioned approximately at 1.8-2.25 meters above the surface. At a few of the ground locations, both a flux station and an automatic meteorological station were located within approximately 50 meters of one another. These are the locations for which there are two values shown in Figure 5.1 just adjacent to each other.

The mean of the air temperature values over the site was 31.9°C. The standard deviation of the values was 0.48°C. It can be seen from the values plotted in Figure 5.1 that some of the co-located stations reported values that were as different from each other as the standard deviation for the entire site. It is reasonable that variations in air temperature would occur across the site as a result of topography, soil moisture, vegetation cover, and all other factors influencing microclimate. However, it is not possible to predict those variations with a level of certainty better than 0.5°C, which is approximately the standard deviation of the mean of the reported values. It is likely that spatial interpolation of air temperature in the regions between the reported values, whether by simple arithmatical interpolation or by physical modeling, would add more uncertainty to the temperature values. Thus, for this analysis, the value of air temperature was assumed to be constant and assigned the value of the mean air temperature for all the sites.

Vapor Pressure

The near-surface vapor pressure is used in the calculation of incoming long-wave radiation term of the net radiation. The values of vapor pressure reported at the ground flux stations and meteorological sites are shown in Figure 5.2. As in Figure 5.1, the axes of Figure 5.2 correspond to the UTM coordinates of the FIFE experimental site, and the data labels represent the value of vapor pressure (kPa) measured at each location. The mean was 2.73 kPa, and the standard deviation was 0.44 kPa of the reported values. As was the case for the air temperature values, there were differences in values measured by different instruments at co-located stations that exceed the standard deviation of the mean value. As was the case for the air temperature, it would seem that interpolating between spatially distributed values would introduce more error than would the assumption of constant vapor pressure over the site. Hence, the vapor pressure was also assumed to be constant over the site and assigned the value of the mean vapor pressure for all the sites.

Windspeed

The near-surface windspeed is used in the estimation of the stability correction to the aerodynamic resistance term in the equation for sensible heat flux. The values of horizontal windspeed (ms^{-1}) reported at the ground flux stations and meteorological sites are shown in Figure 5.3. Because windspeed is more sensitive to instrument height than air temperature or vapor pressure, only those stations for which there was explicit documentation about instrument height, and for which that height was

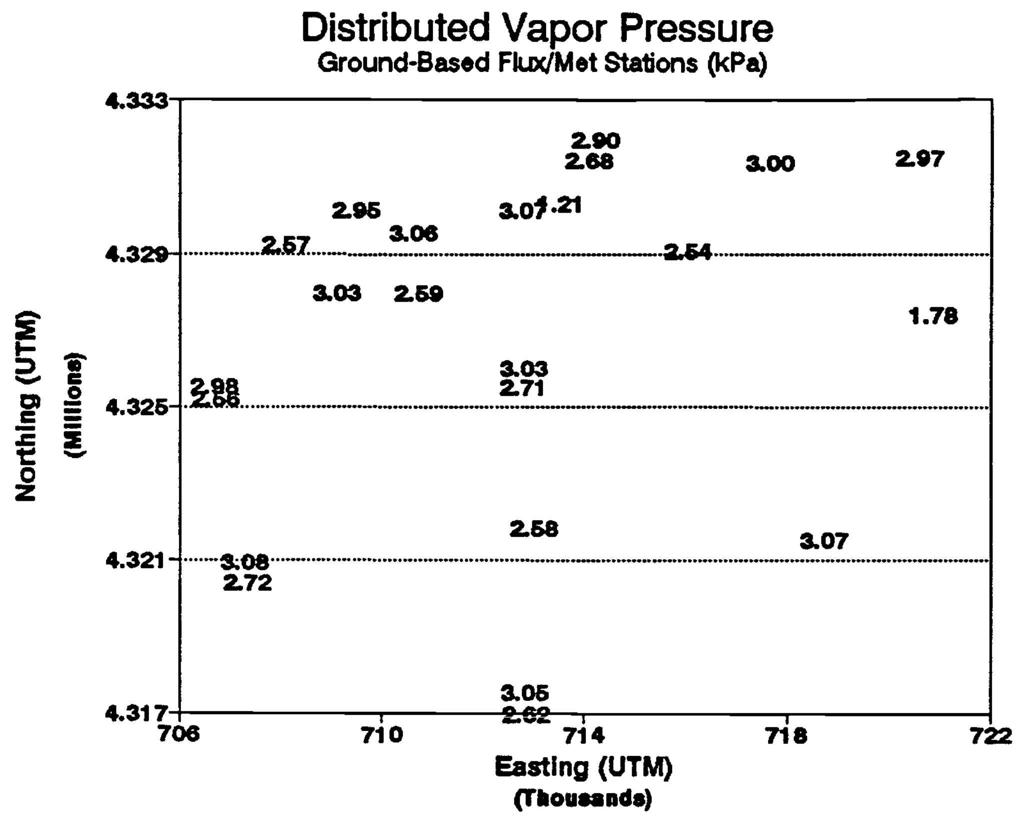

Figure 5.2. The values of vapor pressure (kPa) reported at the ground-based flux stations and meteorological stations plotted at the approximate spatial location of the station on the FIFE experimental site. The temperatures are given in °C and most measurements were taken at a height of approximately 2 meters above the surface.

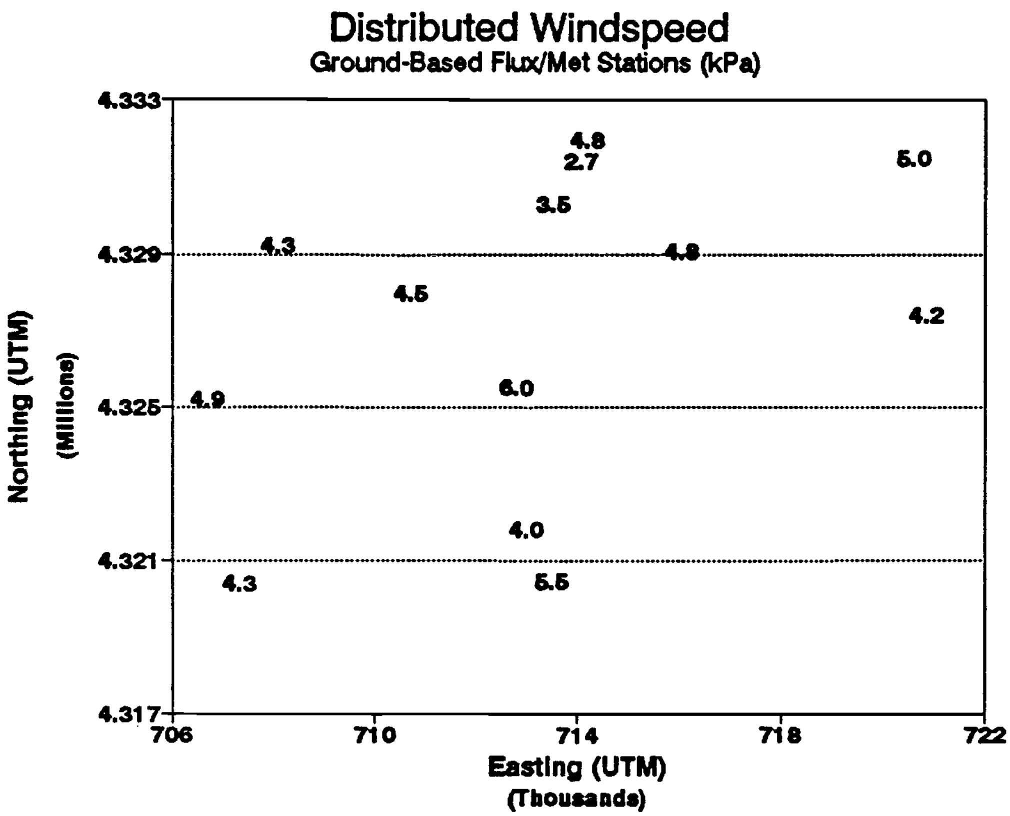

Figure 5.3. The values of windspeed (ms^{-1}) reported at the ground-based flux stations and meteorological stations plotted at the approximate spatial location of the station on the FIFE experimental site. The temperatures are given in °C and most measurements were taken at a height of approximately 2 meters above the surface.

2 meters +/- 0.2 meters, are shown in Figure 5.3. The mean and standard deviation of the reported values were 4.5 and 0.84 m/s, respectively. The actual windspeed near the surface is likely to be dependent on topography. However, the level of uncertainty with which that effect could be predicted is rather large and, again, an arithmatical or physically based interpolation scheme would likely introduce more error than the assumption of a constant value over the site. Thus, the windspeed was assumed to be constant over the site and assigned the value of the mean windspeed for all the sites.

Canopy Height

The aerodynamic resistance term in Equation (5.7) is affected by roughness length, z_o, and displacement height, d, as given in Equations (4.9) and (4.10). These quantities can be estimated with wind profile measurements. For the case of nearly full homogeneous canopies, empirical relationships have been developed which relate z_o and d to average canopy height (h), (e.g., d = 0.65h and z_o = 0.13h, where h is the average canopy height in meters (Brutsaert, 1982)). These relationships are not necessarily valid over partial vegetation cover, and it is difficult to develop generalized expressions which are valid over various vegetation types and densities. The estimation of these parameters over partial vegetation cover remains an active research issue (Verma and Barfield, 1979; Hatfield, 1989; Kustas et al.,1989a). However, for lack of alternatives at this time, the above relationships were used.

Even with the assumption that a reliable relationship exists between canopy height and these aerodynamic parameters, canopy height is not a quantity that is readily derived from remote sensing measurements. Several empirical, crop-specific relationships have been developed between vegetation indices and aerodynamic resistance (Hatfield, 1989; Moran, 1990).

For the FIFE site, these parameters are particularly challenging to assess with the desired level of accuracy because of the diversity of the vegetation present. The site includes areas of grazed and ungrazed grassland, small areas of agricultural crops and bare fields, and drainage areas with woody vegetation communities which have canopy heights that sometimes exceed 3 meters. The cropland and woody vegetation represent a fairly small fractional area of the site, but there were no ground data acquired in those areas.

At the flux stations, which were all located in grazed or ungrazed grassland areas, canopy density and height measurements were made approximately every 5-7 days. Using the canopy height data for the time periods that included the August 15 overpass and the reflectance estimates from the pixels extracted from the TM data which cover particular flux stations, the relationship between canopy height and NDVI was evaluated. The results are shown in Figure 5.4. There is not a simple theoretical relationship between canopy height and NDVI. The correlation between canopy height and NDVI for the grassland areas is likely due to the correlation between canopy height and canopy density for the grassland portions of the FIFE site. The regression equation shown as the solid line in Figure 5.4 is:

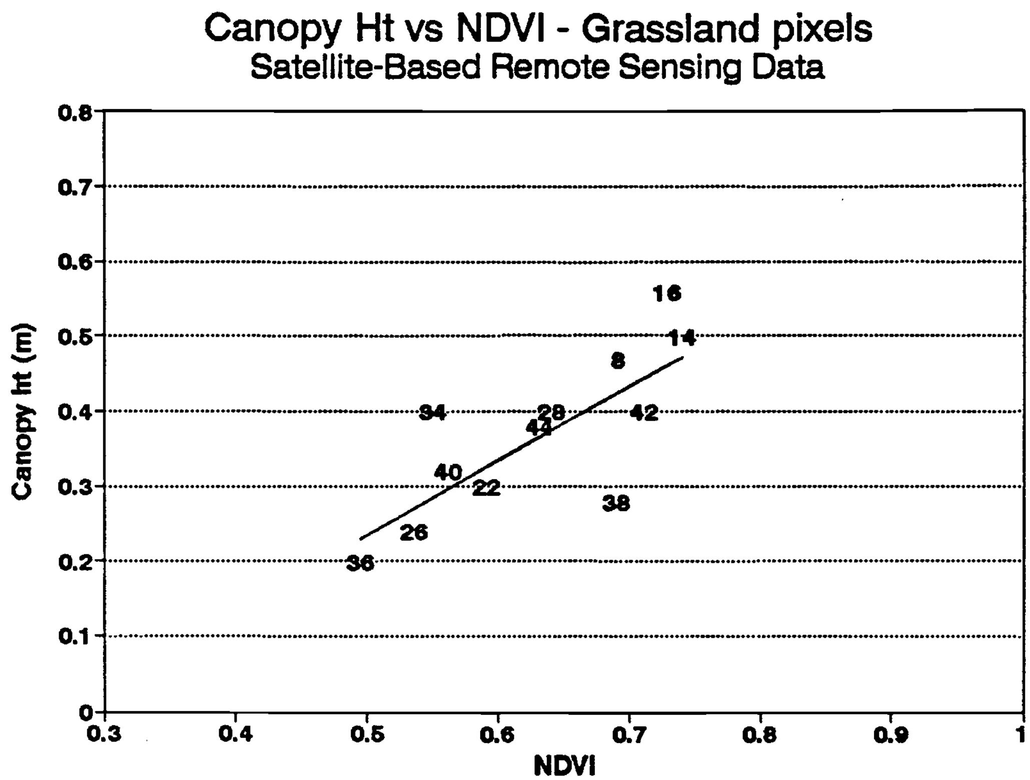

Figure 5.4. Mean canopy height values measured at the ground-based flux stations plotted against NDVI computed from the atmospherically corrected surface reflectances in TM Bands 3 and 4. The data labels refer to the ground site number of the flux station.

$$h = -0.26 + 0.99 * (NDVI). \tag{5.8}$$

It should be stressed that the derived relationship is likely to be valid only over the grassland areas of the FIFE experimental site.

By comparison of the NDVI image derived from the August 15, 1987 TM image with a site stratification image developed by Davis et al. (1990) using a combination of ground and satellite data from spring and summer 1987, it was observed that the woody vegetation areas generally had an NDVI value in the August image which exceeded 0.82. Additionally, in some of the areas classified as cropland in the stratification image, the NDVI values on the August 15 TM image were generally less than 0.35 and appeared to be those pixels corresponding to fallow fields. For this analysis then, canopy height was estimated for each pixel from the NDVI values derived from the August 15 TM image. For NDVI values between 0.3 and 0.82, Equation (5.8) was applied. Pixels with NDVI values above 0.82 were assumed to be woody vegetation, and an average value of 1.5 meters was assigned for the canopy height. Pixels with NDVI values below 0.3 were assumed to be bare soil, and a roughness length of 0.5 cm was assigned.

Sensitivity of Flux Calculations to Ground-Based Parameters

In order to estimate the sensitivity of the sensible heat flux calculations to several of these ground-based parameters, the value of the sensible heat flux computed with Equation (5.7) is plotted against canopy height for several different values for aerodynamic temperature-air temperature difference in Figure 5.5. When (T_o-T_a) is about 2°C, a difference in canopy height of 0.2 meters accounts for about 50 Wm^{-2} difference in sensible heat flux. For larger values of (T_o-T_a), the value of sensible heat flux is more sensitive to canopy height. Given the difficulty in estimating canopy height for all pixels in an extended area (and thus the uncertainty in roughness parameters), this appears to be a potential source of significant error in the estimation of sensible heat flux with a combination of ground-based and remotely sensed data.

In order to evaluate the sensitivity of sensible heat flux estimates to uncertainties in air temperatures (or surface temperature), the values of sensible heat computed with Equation (5.7) are plotted as a function of (T_s-T_o) in Figure 5.6. Under conditions of moderate windspeed and roughness parameters corresponding to a canopy height of 0.3 meters (approximately the median value of the canopy heights measured over the ground stations used in this analysis), a one-degree error in either of the temperatures used in Equation (5.7) corresponds to approximately 70 Wm^{-2} of sensible heat flux. For taller vegetation (e.g., canopy height approximately 0.9 meters, which is taller than vegetation in the grassland pixels but smaller than the height of most of the woody vegetation), the curves shown in Figure 5.6 show that a one-degree error in surface temperature corresponds to approximately 150 Wm^{-2} of sensible heat flux. Thus, typical levels of uncertainty in surface temperature lead to significant errors in the estimation of sensible heat flux, particularly for taller vegetation types.

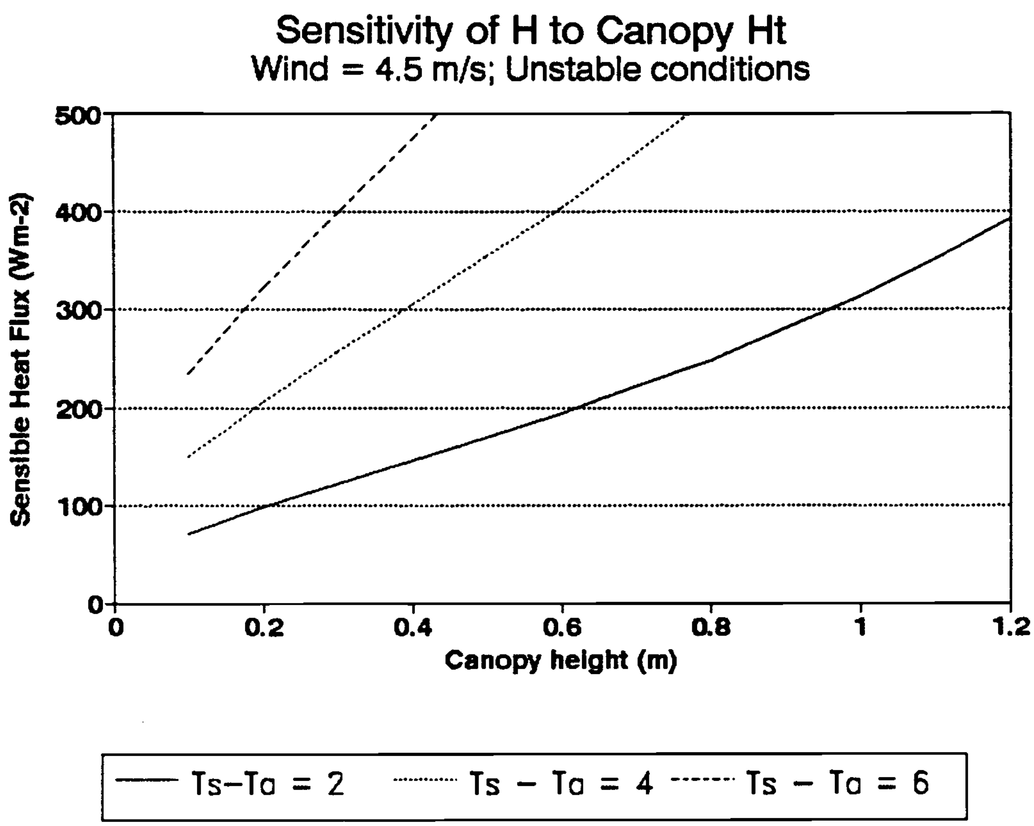

Figure 5.5. The computed relationship between sensible heat flux (Wm^{-2}) and canopy height, with windspeed held constant at 4.5 m/s and for different values of surface air temperature difference. Values of sensible heat are computed from Equation (5.8).

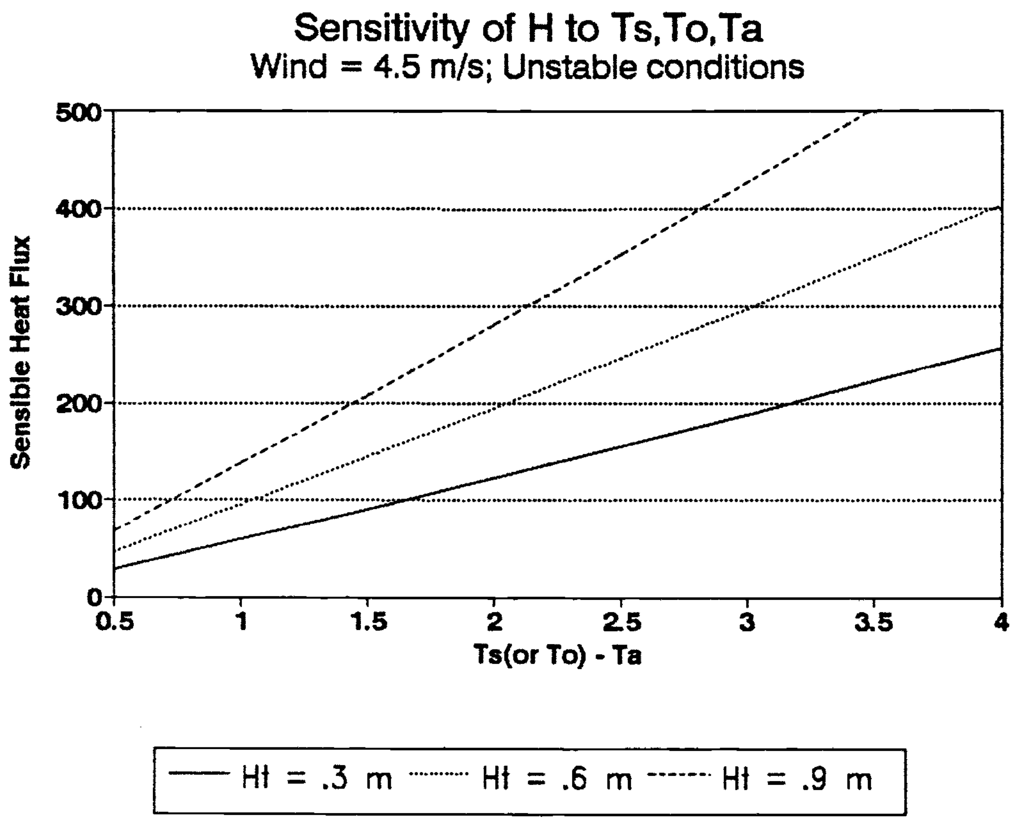

Figure 5.6. The computed relationship between sensible heat flux (Wm^{-2}) and surface-air temperature difference, with windspeed held constant at 4.5 m/s and for different values of canopy height. temperature difference. Values of sensible heat are computed from Equation (5.7).

Satellite-Based Input Data

Surface Temperature

The atmospherically corrected surface temperature over the FIFE site derived from Band 6 of the TM image acquired on August 15, 1987 is shown in Figure 5.7. The algorithms described in Chapter 4 that were applied to the satellite pixel extracts to convert the TM digital number to at-satellite radiance and to correct for atmospheric effects were applied to each pixel in the image to calculate corrected surface temperatures for the whole site. An emissivity value of 0.98 was assumed for all pixels. The darkest pixels in Figure 5.7 correspond to a surface temperature of approximately 29°C, and the lightest pixels correspond to a surface temperature of approximately 38°C. The spatial resolution of surface temperature data is 120 meters.

Net Solar Radiation

The spatially distributed net solar radiation (referred to as $R_{net,solar}$) calculated by Dubayah et al. (1990) for the FIFE site at TM overpass time on August 15, 1987 is shown in Figure 5.8. The incoming solar radiation for each pixel was computed from a combination of ground-based solar irradiance measurements and digital elevation data. The outgoing shortwave radiation was computed using atmospherically corrected data in TM Bands 1-5;7. The darkest pixels represent a value of $R_{net,solar}$ of about 480 Wm^{-2}, and the lightest pixels represent a value of $R_{net,solar}$ of about 680 Wm^{-2}.

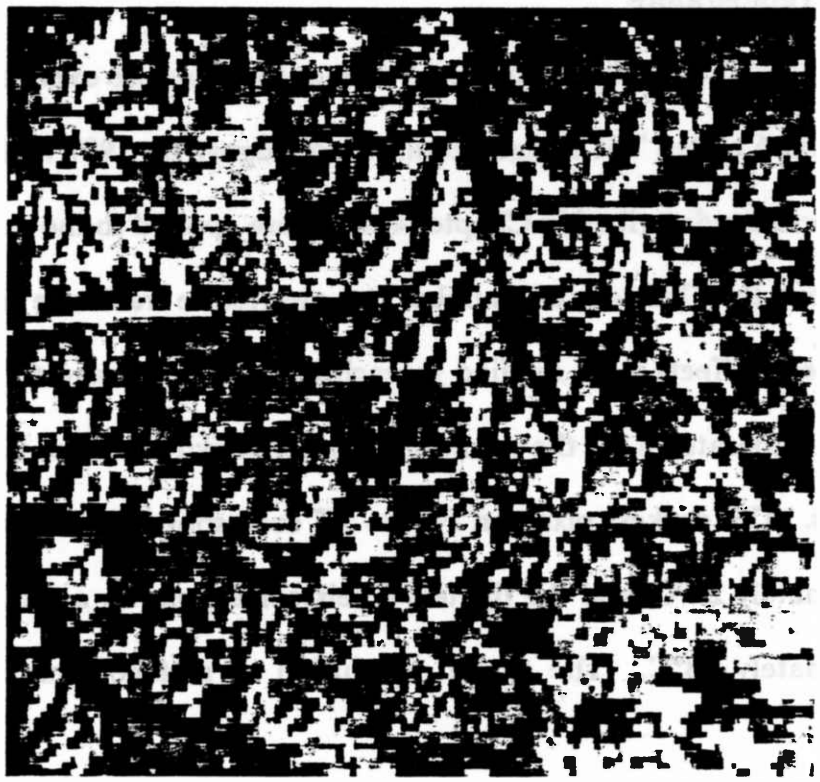

Figure 5.7. Atmospherically corrected surface temperature image of the FIFE site from TM Band 6, August 15, 1987. The darkest pixels correspond to a surface temperature of approximately 29°C and the lightest pixels correspond to a surface temperature of approximately 38°C. Spatial resolution of surface temperature data is 120 meters.

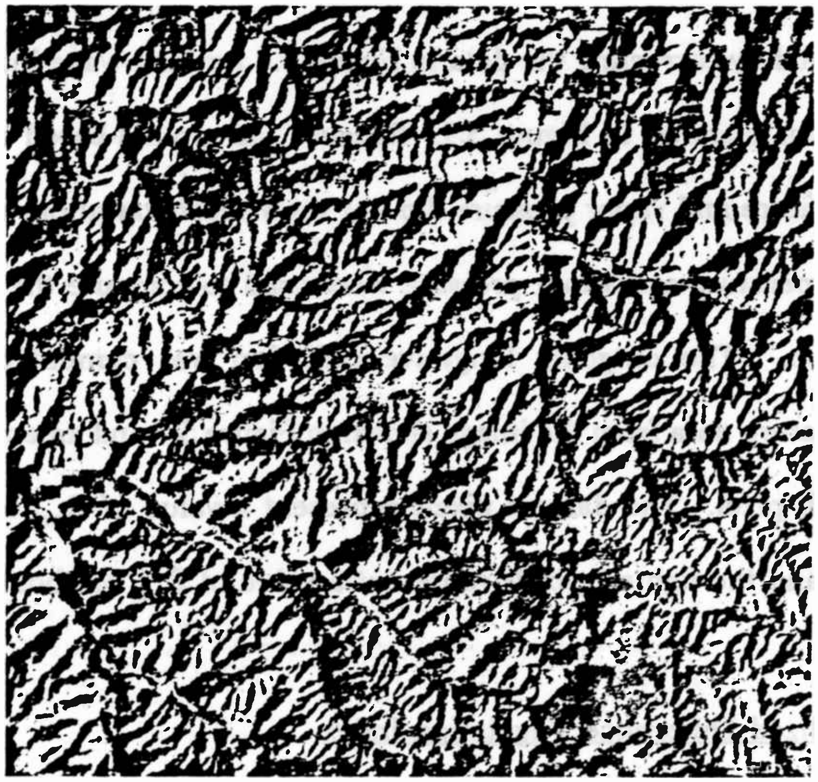

Figure 5.8. Spatially distributed net solar radiation for the FIFE site at TM overpass time calculated by Dubayah et al. (1990) from a combination of ground data and data in TM Bands 1-5;7 for August 15, 1987. The darkest pixels represent a value of Rnet,total of about 480 Wm^{-2} and the lightest pixels represent a value of $R_{net,total}$ of about 680 Wm^{-2}.

Net Radiation

The spatially distributed net radiation for the FIFE site at TM overpass time, calculated by correcting the data in Figure 5.8 for long-wave incoming and outgoing radiation, is shown in Figure 5.9. Because the ground-based measurements of air temperature and vapor pressure did not show much variation, site-wide averages of air temperature and vapor pressure were used to compute the incoming long-wave radiation. The outgoing longwave radiation was computed using the surface temperature data from the image shown in Figure 5.7 and an emissivity value of 0.98 for each pixel. The darkest pixels represent a value of R_{net} of approximately 380 Wm^{-2}, and the lightest pixels represent a value of R_{net} of about 580 Wm^{-2}.

Normalized Difference Vegetation Index

The NDVI image for the FIFE site computed from atmospherically corrected surface reflectance values from TM Bands 3 and 4, August 15, 1987 is shown in Figure 5.10. The darkest pixels represent a value for NDVI of about 0.2, and the lightest pixels represent a value for NDVI of about 0.82. The highest values of NDVI correspond to the areas of dense woody vegetation near the drainage areas. The lowest values of NDVI correspond to fallow agricultural fields.

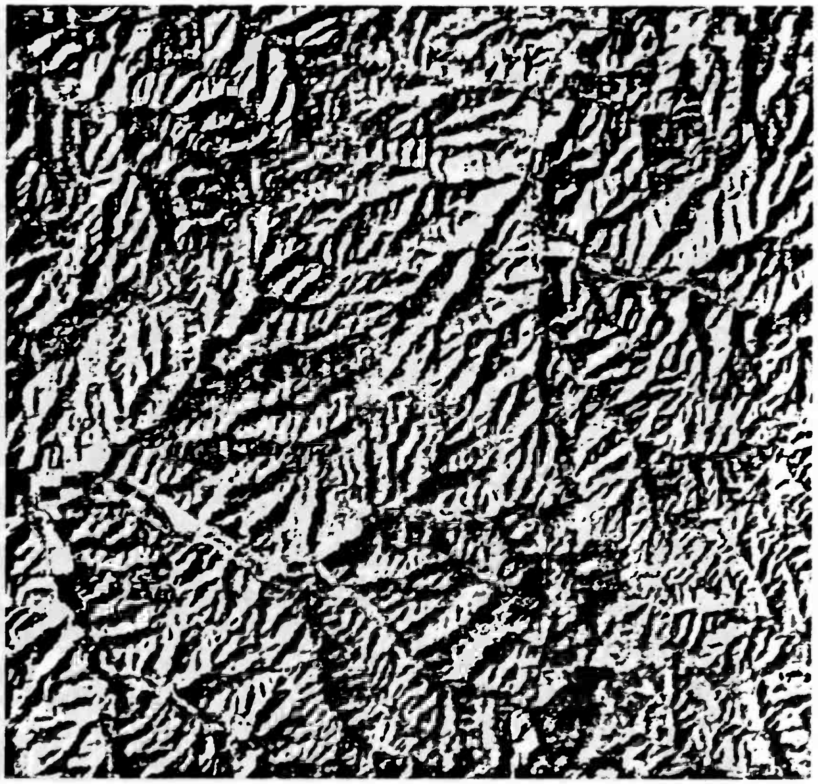

Figure 5.9. Spatially distributed net radiation for the FIFE site at TM overpass time, calculated by correcting the data in Figure 5.8 for longwave incoming and outgoing radiation. The darkest pixels represent a value of $R_{net,total}$ of about 380 Wm^{-2} and the lightest pixels represent a value of Rnet,total of about 580 Wm^{-2}.

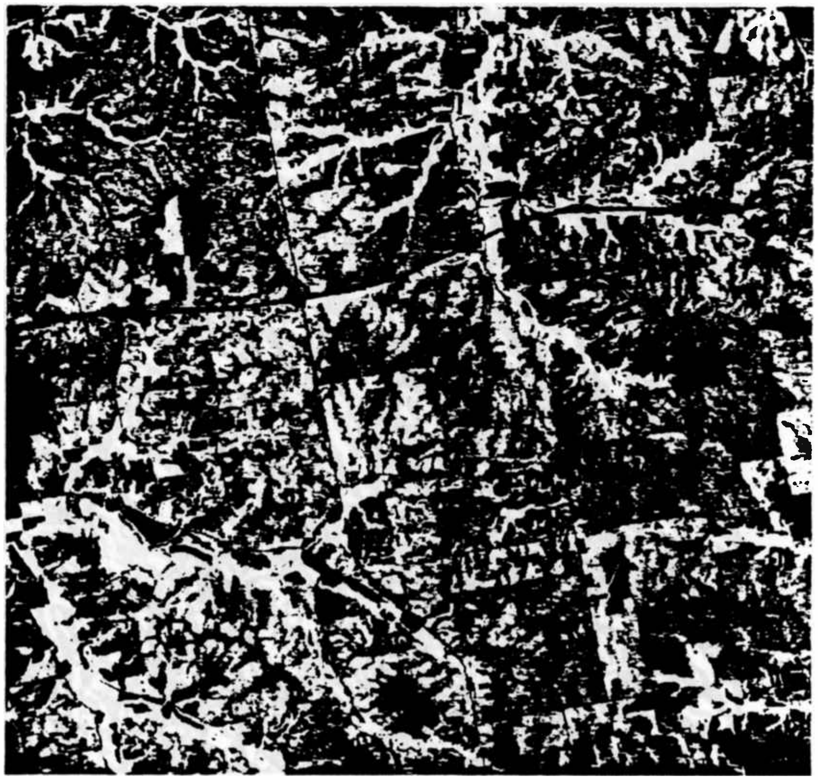

Figure 5.10. NDVI image for the FIFE site computed from atmospherically corrected surface reflectance values from TM Bands 3 and 4, August 15, 1987. The darkest pixels represent a value for NDVI of about 0.2 and the lightest pixels represent a value for NDVI of about 0.86.

Fluxes and Related Parameters

Soil Heat Flux

The values of the soil heat flux (G) term of the energy balance were computed for every pixel using the values of R_{net} represented in Figure 5.9 and Equation (5.5). The results are shown in Figure 5.11. The darkest pixels in Figure 5.11 represent values of G of about 20 Wm^{-2}, and the lightest pixels represent a value of G of approximately 120 Wm^{-2}. Because the soil heat flux is inversely proportional to the value of NDVI, the pixels with high NDVI values have low (darker) values of G. These areas are primarily the agricultural areas in the bottomlands and the areas of woody vegetation in drainage areas. The light patches in the agricultural areas correspond to areas with very low NDVI values which are most likely fallow fields.

Aerodynamic Resistance

The aerodynamic resistance parameter used in the estimation of the sensible heat flux was computed using the strategy described above. For the grassland pixels, a value of canopy height was estimated from the NDVI value and Equation (5.8). The roughness parameters were assumed to be proportional to canopy height. For the areas of woody vegetation, a canopy height of 1.5 meters was assumed. For the agricultural areas with very low NDVI values, most likely fallow fields, a roughness length of 0.5 was assumed (corresponding to values reported in the vegetation descriptions in the FIFE Information System). The spatially distributed estimates of aerodynamic resistance are shown in Figure 5.12. The darkest pixels correspond to

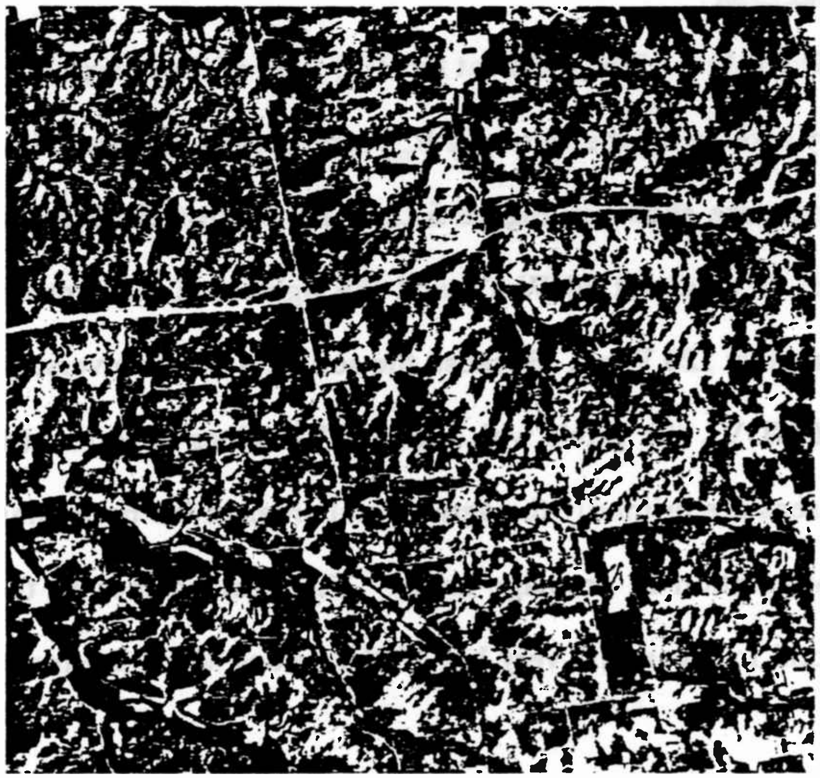

Figure 5.11. Spatially distributed soil heat flux for the FIFE site at TM overpass time on August 15, 1987. Values are computed from the data shown in Figure 5.9 (Rnet,total) and Figure 5.10 (NDVI) and Equation (5.5). The darkest pixels represent a value for G of about 20 Wm^{-2} and the lightest pixels represent a value for G of about 120 Wm^{-2}.

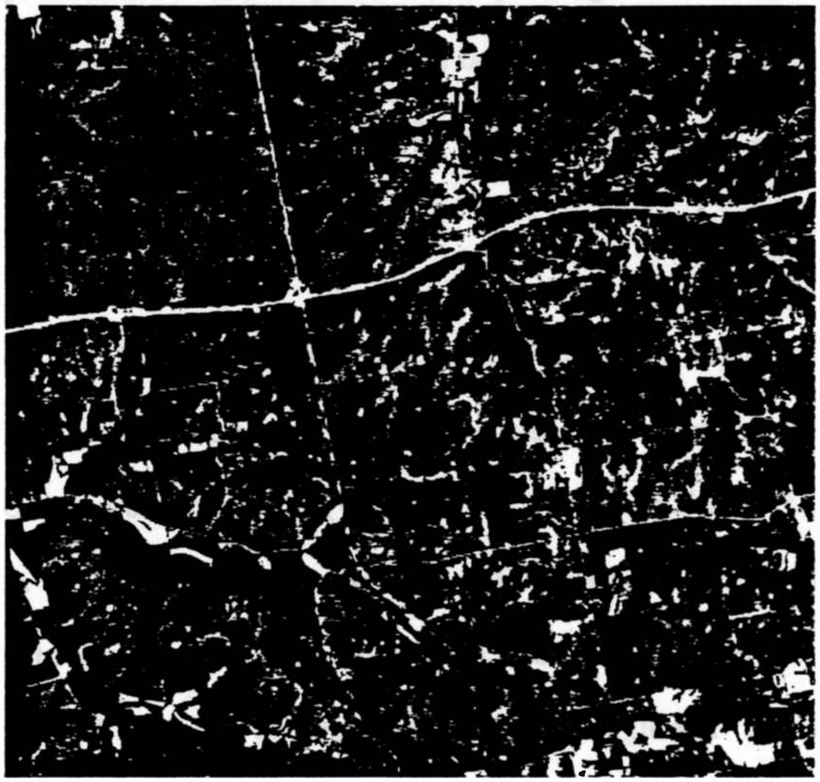

Figure 5.12. Spatially distributed values for aerodynamic resistance over the FIFE site at TM overpass time on August 15, 1987. Values are computed with a constant value for windspeed over the entire site, assumed to be 4.5 ms^{-1} at a reference height of 2 meters. Estimates of canopy height, from which roughness length and displacement height were computed, were derived from the NDVI data shown in Figure 5.10 and the strategy described in the text. The darkest pixels correspond to the woody vegetation along the drainage areas, where r_a was calculated to be approximately 6 sm^{-1}. The lightest areas correspond to the bare soil pixels and roads, where ra was calculated to be approximately 50 sm^{-1}. Most of the grassland areas in the image have an r_a of approximately 15-25 sm^{-1}.

values of r_a of about 6 sm^{-1}, which are the areas of woody vegetation along the drainage areas. The lightest pixels correspond to a value of r_a of about 50 sm^{-1}, which are primarily the pixels that are roads and fallow fields. Most of the grassland pixels have r_a values within about 15-25 sm^{-1}.

Sensible Heat Flux

The values of sensible heat flux were computed for each pixel using the surface temperature data represented in Figure 5.7, the r_a values represented in Figure 5.13, and Equations (5.6) and (5.7). The results are shown in Figure 5.13. The darkest pixels correspond to values of sensible heat of about 40 Wm^{-2} and correspond primarily to those areas with very high values of r_a described in the section above. The lightest pixels correspond to values of H of about 200 Wm^{-2} and are those pixels with very low values of r_a, primarily the areas of woody vegetation. Most of the grassland pixels have pixel values corresponding to about 80-160 Wm^{-2}.

Latent Heat Flux

The values of latent heat flux were computed for each pixel as the residual quantity in Equation (5.1) after the R_{net}, G, and H terms were estimated. The results are shown in Figure 5.14. The spatially distributed values of latent heat flux calculated by this method correspond very closely to the net radiation. This is expected to some degree because most portions of the experimental site received significant precipitation on August 13, and the evapotranspiration in most areas of

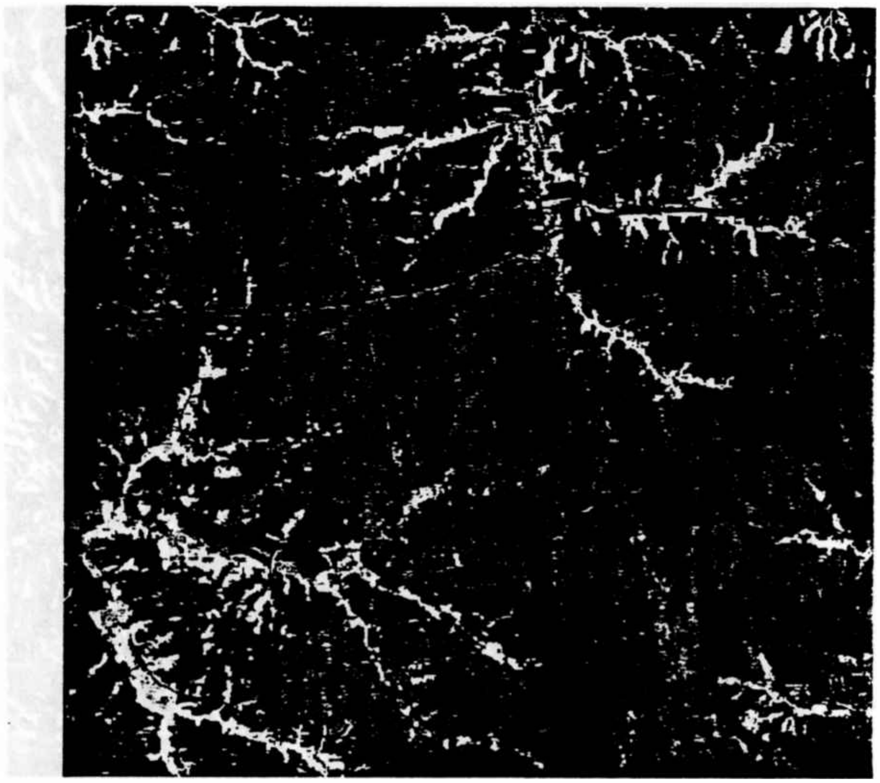

Figure 5.13. Spatially distributed values for sensible heat flux over the FIFE site at TM overpass time on August 16, 1987. Values of H were computed with data from Figure 5.7 (surface temperature), Figure 5.12 (r_a) and Equation (5.7). The darkest pixels correspond to areas with values of H of about 40 Wm-2, which also correspond to the areas with very high values of r_a, such as bare soil and roads. The lightest pixels correspond to values of H of about 200 Wm^{-2}, which also correspond to areas with very low values for r_a, such as the woody vegetation along the drainage areas. Most of the grassland areas have pixel values corresponding to about 80-160 Wm^{-2}.

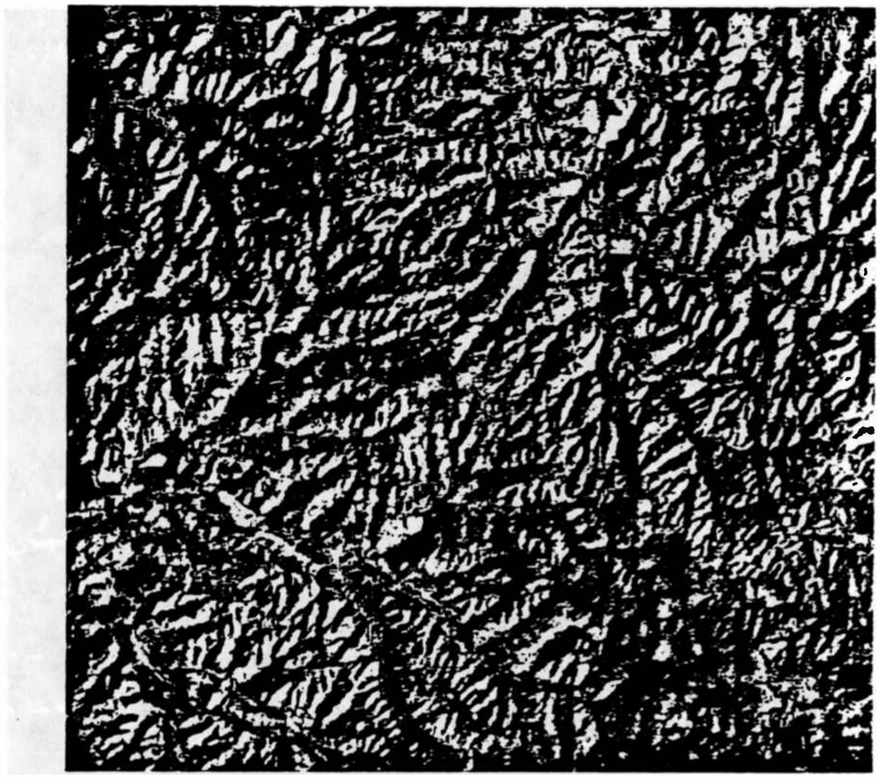

Figure 5.14. Spatially distributed values for latent heat flux over the FIFE site at TM overpass time August 15, 1987. The values of LE were computed using the data shown Figure 5.9 ($R_{net,total}$), Figure 5.11 (G), Figure 5.13 (H), and Equation (5.1).

the site was likely to be energy-limited at mid-morning on August 15. It is likely, however, that the spatially distributed map of net radiation and the spatially distributed latent heat flux map correspond even more closely than one might expect because of the method by which G and H are computed. Both quantities (H and G) are related to the value of NDVI, but in opposite directions. The value of soil heat flux, G, is inversely proportional to the NDVI as described in Equation (5.5). The sensible heat flux is influenced by the NDVI through the aerodynamic resistance parameter. When NDVI is large, r_a is smaller, and H is therefore larger. Thus, because G and H are related to NDVI in opposite ways, they will tend to offset one another, leading to values of LE which are strongly dependent on the net radiation.

Discussion of Error Sources

The largest sources of error in estimating the fluxes described above are likely to be: (1) estimation of the roughness parameters which influences the value of aerodynamic resistance that impacts the sensible heat flux proportionally, (2) problems with the atmospheric correction of satellite data to obtain accurate estimates of surface temperature, and (3) the spatial scale to which the ground-based near-surface air temperature, windspeed, and vapor pressure can be extended. The first source of error is likely to be considerably more significant over the non-grassland areas of the site than it is over the grassland portions of the site. Thus, the magnitude of the uncertainty in the sensible and latent heat flux values for the non-grassland portions of the spatially distributed map is likely to be considerably larger than the uncertainty in the fluxes for the grassland pixels. It can be seen from Equation (5.7) that a certain percentage error in the estimation of r_a gives rise to that same percentage error in the estimate of sensible heat flux.

Summary and Conclusions

Spatially distributed values of soil heat flux, sensible heat flux, and latent heat flux were computed for the FIFE site using a combination of ground-based data and the August 15 Landsat TM image. The algorithm used to estimate the fluxes was developed and validated with ground-based flux station data in the previous chapter. The surface fluxes at the mid-morning overpass time (10:34 a.m. CDT) for the grassland pixels were consistent with those measured at ground-based flux stations. Due to considerable differences in surface roughness parameters, and in part to differences in surface temperature, the pixels corresponding to agricultural areas and areas of woody vegetation showed the most variation in surface fluxes. Because of particular large uncertainties in surface roughness parameters for areas of woody vegetation, the uncertainty associated with the surface fluxes for those areas is considerably larger than the uncertainty associated with the fluxes estimated for the grassland pixels. Unfortunately, there were no ground-based data available with which to compare the remotely sensed flux estimates for the non-grassland pixels.

The values of sensible heat flux, and thus values of latent heat flux, were very sensitive to surface roughness parameters, which cannot be well quantified with current remote sensing techniques. An important area of future research would be to investigate methods to quantify roughness parameters with remotely sensed data, such as near-simultaneous measurements with a laser altimeter or a radar system or improved classification schemes using visible and near-infrared data which will provide better information about species type, such as those that might be available with high spectral resolution visible and near-infrared data.

CHAPTER 6

RELATING THE SPATIAL VARIABILITY OF REMOTE SENSING OBSERVATIONS TO DERIVED PRODUCTS AT VARIOUS SPATIAL SCALES

Introduction

Most satellite-based sensors providing remotely sensed data over land surfaces operate with a spatial resolution larger than that of the TM sensor (30m in the visible and near-infrared bands and 120m in the thermal bands). For satellite-based sensors, instrument design and orbital consideration necessitate a trade-off between spatial and temporal resolution. Sensors which provide more frequent temporal coverage of an area, as is desirable for monitoring fluxes of moisture and energy, generally have lower spatial resolution. For example, the Advanced High-Resolution Radiometer (AVHRR) (currently on board several NOAA satellites), which is widely used for regional monitoring of land surface processes has a spatial resolution of 1 km in Local Area Coverage (LAC) mode and 5 km in Global Area Coverage (GAC) mode. One of the primary sensors planned for the Earth Observing System (EOS) payload designed to provide remotely sensed data for monitoring land-surface processes is the MODIS-N sensor, which will have a spatial resolution of 500 meters.

It is important that we better understand how surface parameters and fluxes estimated with remotely sensed data vary with spatial scale. There are two distinctly different areas of research related to the spatial scaling of surface parameters and fluxes. The first issue relates to how the procedures and the spatial scale of the remotely sensed data influence the estimated values of surface parameters and fluxes. The second issue relates to how these spatially-variable surface fluxes interact with the atmospheric boundary layer (ABL) and are integrated by the ABL, which provides an understanding of the level of significance of surface heterogeneities. The first topic is addressed here; the second topic is an important area of future research.

Remote sensing instruments measure an integrated response over heterogeneous areas. The surface parameters estimated with remotely sensed data are spatially integrated averages of parameters which are actually spatially variable. The surface characteristics or fluxes are usually related to the remotely sensed observables in a non-linear manner. If the functions relating the remotely sensed observables to surface characteristics were linear, then the spatially integrated surface characteristics at any scale would simply be equal to the value of the linear relationship evaluated at the integrated mean value of the remotely sensed observables. However, when the functions relating input parameters to surface characteristics or fluxes are non-linear, then the mean spatially integrated response is not equal to the output of the function evaluated at the mean parameter values. A method is proposed to quantify the values of the spatially integrated response at increasing spatial scales in terms of the variability of the observables at smaller spatial scales.

Theory

Given a non-linear function, f, which relates several input parameters (x_k) to an output y, i.e.:

$$y = f\{x_1, x_2 \cdots x_k\}, \qquad (6.1)$$

the relationship between the output of the function and the mean values of the parameters can be obtained by expanding the output y in a Taylor series around the set of mean parameter values, $\overline{x_k}$. This expansion yields the expression:

$$y = f\{x_k\} = f(\bar{x}_k) + \sum_{n=1}^{\infty} \frac{1}{n} \left[(x_k - \bar{x}_k) \cdot \frac{\partial f}{\partial x_k}\right]^n f(\bar{x}_k). \qquad (6.2)$$

Taking the expected value of both sides and neglecting terms for which n is 3 or greater, one obtains:

$$y = f(\bar{x}_k) + 1/2 \sum_{i=1}^{k} \sum_{j=1}^{k} \frac{\partial^2 f}{\partial x_i \partial x_j} \left[\sigma_i \sigma_j \rho_{ij}\right], \qquad (6.3)$$

where σ_i is the standard deviation of the ith parameter, and ρ_{ij} is the correlation coefficient between the ith and jth parameters.

For example, if y is a function of two variables, then Equation (6.3) becomes:

$$y = f(\bar{x}_1, \bar{x}_2) + [\frac{1}{2} (\sigma_1^2 \frac{\partial^2 f}{\partial x_1^2} + \sigma_2^2 \frac{\partial^2 f}{\partial x_2^2}) + \frac{\partial^2 f}{\partial x_1 \partial x_2} \sigma_1 \sigma_2 \rho_{12}]. \qquad (6.4)$$

Conceptually, this equation implies that the difference between the spatially integrated output, y, and the value of the function evaluated at the mean values for the parameters depends on two factors: (1) the degree of non-linearity of the function with respect to each of the parameters, as expressed in the second derivatives of the function with respect to the parameters, and (2) the magnitude of the variance for each parameter. It is useful to note that, if the variance of the parameters is zero, or if the values of the second derivatives are zero (i.e., the function is linear in those parameters), then the spatially integrated value of the function is equal to the value of the function at the mean values of the parameters.

Prediction of Larger-Scale Values of Derived Products from Variability in Input Parameters at Smaller Scale

In order to test the application of this approach to the spatial scaling of a quantity derived from remote sensing observations, the behavior of the Normalized Difference Vegetation Index (NDVI) was evaluated as a function of spatial scale. Because the NDVI is related to remotely sensed quantities by a fairly simple function, it provides a good example with which to illustrate this approach. One way to compare the value of a quantity derived from remotely sensed data, such as NDVI, at various spatial scales is to compare the estimates of that quantity using data from sensors operating at different spatial scales. However, such a comparison would include not just the effects of surface heterogeneity on spatial scaling of derived quantities, but also instrumental effects such as different bandpasses, different instrument response functions, and instrument calibration.

In order to isolate the effects of surface heterogeneity on differences in NDVI computed with remote sensing data at different spatial resolutions, a window of variable size, encompassing blocks of TM pixels, was applied to the Landsat data in TM Bands 3 and 4 from the August 15, 1987 image to simulate different spatial resolutions. The spatial resolution of interest was varied by varying the size of the window. A conceptual diagram of the window of spatial averaging is shown in Figure 6.1. The window was moved around within the 512 x 512 pixel TM Band 3 and 4 images covering the FIFE experimental site. Each point on the plots (shown later in Figures 6.3 through 6.6) represents the value of the NDVI within the window when the window is placed over different portions of the TM image.

As described in previous chapters, the NDVI computed with TM data is given by:

$$NDVI = f(\rho_{RED}, \rho_{NIR}) = \frac{\rho_{NIR} - \rho_{RED}}{\rho_{NIR} + \rho_{RED}}, \tag{6.5}$$

where ρ_{RED} is the reflectance in TM Band 3, and ρ_{NIR} is the reflectance in TM Band 4.

A conceptual diagram is shown in Figure 6.2 of the difference between the integrated NDVI value computed by taking the mean of the distributed values of NDVI for fine resolution pixels (referred to as $(NDVI)_{MODV}$, shown on the left-hand side of Figure 6.2), and the value of NDVI computed for the same area by using lumped values of reflectances to compute a single value of NDVI (referred to as $(NDVI)_{LUMP}$, shown on the right-hand side of Figure 6.2). The left-hand side of the

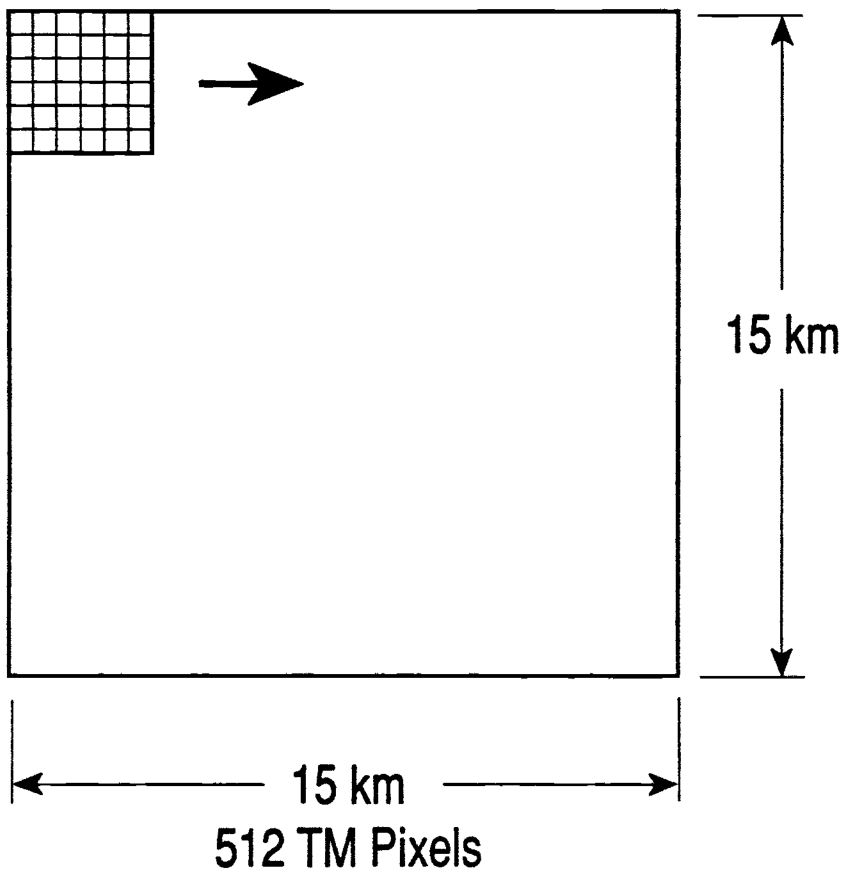

Figure 6.1. Conceptual diagram of the window of spatial averaging, of variable size (n x n 30-meter TM pixels).

$$NDVI = \frac{\rho_{NIR} - \rho_{RED}}{\rho_{NIR} + \rho_{RED}}$$

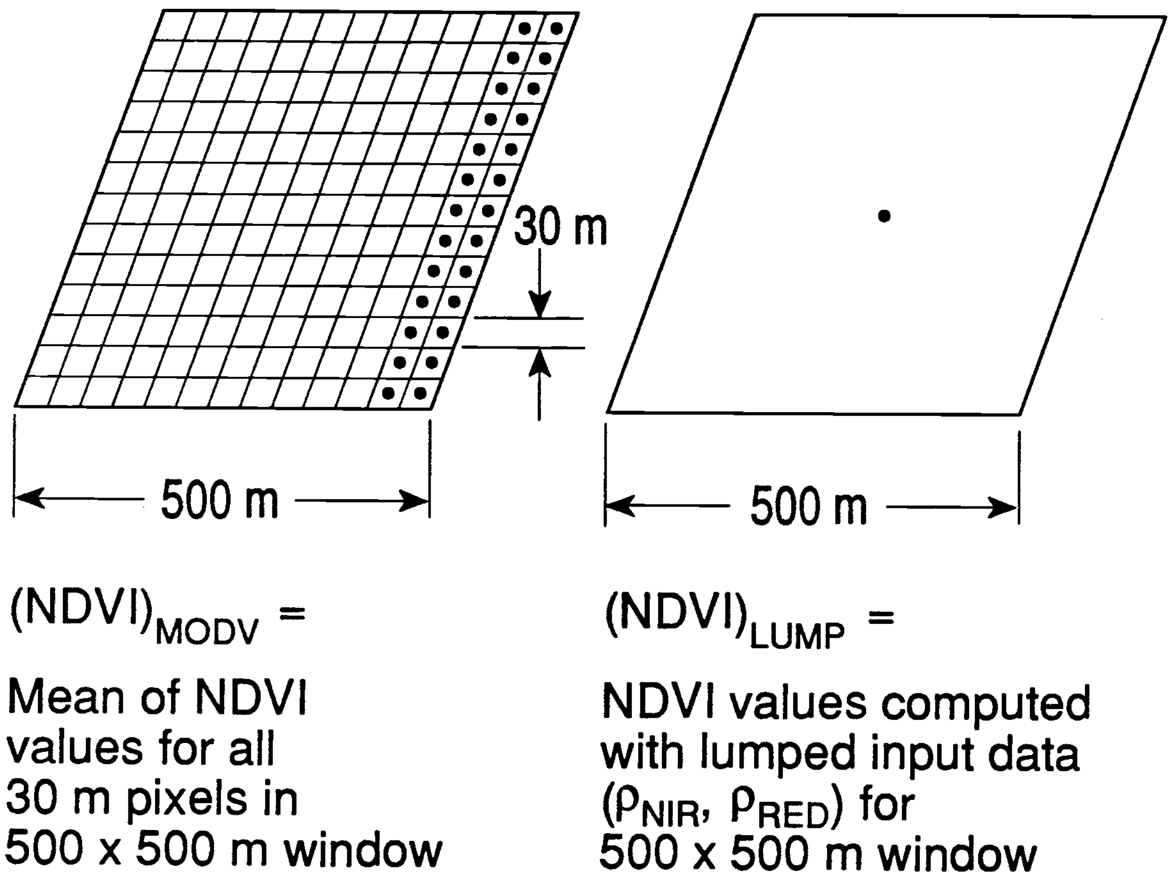

Figure 6.2. Conceptual diagram of the distinction between the $(NDVI)_{MODV}$, computed from the mean of all NDVI values computed each 30-meter pixel in 500 x 500-meter pixel (shown on the left side of the diagram), versus the $(NDVI)_{LUMP}$, computed from average values of red and NIR reflectance over the 500-meter window (shown on the right side of the diagram).

diagram simulates the value of vegetation index which would be computed for a given area using high spatial resolution data; the right-hand side simulates the value which would be computed for the same area using low resolution data (instrumental differences notwithstanding). The purpose of this analysis is to quantify the difference in those values in terms of the variability in the observed quantities (in this case, the variability of the red and near-infrared reflectances) and the non-linearity of the function which relates the quantities to the surface parameter of interest (in this case, the NDVI).

The results shown in Figure 6.3 illustrate the differences between the NDVI computed in 480 x 480 meter windows over the site using mean values of the input observations (red and near-infrared (NIR) reflectances) and the more accurate mean integrated response for each window. When a 480 x 480 meter window (encompassing 16 x 16 TM pixels) is moved around on the Landsat image, there are 1024 non-overlapping positions for the window. This window represents the approximate size of one pixel for the EOS MODIS sensor. The points on the plot represent results from each of those possible non-overlapping positions. The x-axis of the plot in Figure 6.3 represents the value of NDVI computed with the value of red and NIR reflectance averaged over the window. Assuming that the effects of interactions between pixels for this type of surface at these spatial scales is negligible, then the values of red and NIR reflectance averaged over the window would represent the lumped reflectances that would be measured by a sensor with 480 x 480 meter spatial resolution. Thus, the NDVI values computed from the mean red and NIR

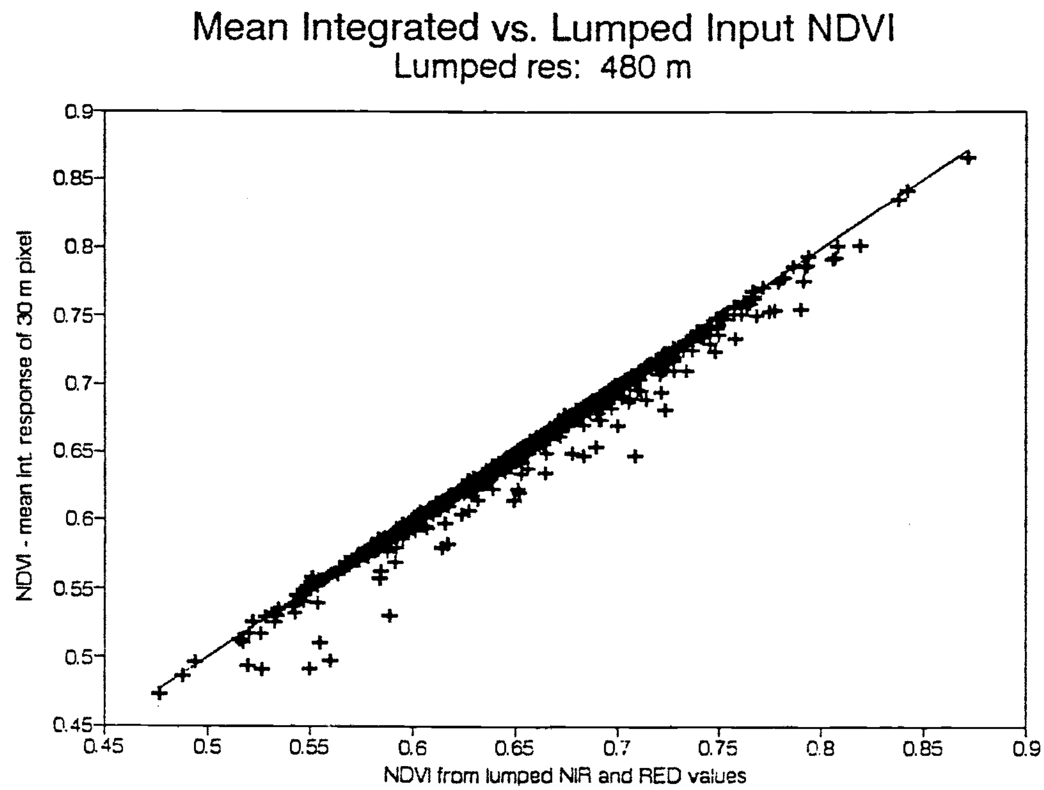

Figure 6.3. Areally integrated average NDVI (computed from individual 30-meter Landsat pixels) plotted against the NDVI computed from the mean values of RED and NIR reflectance for the window. The size of the averaging window was 480 meters, or 16 x 16 TM Band3/4 pixels.

reflectance values would represent the NDVI that would be estimated from a sensor with that spatial resolution. The y-axis of the plot shown in Figure 6.3 represents the mean integrated value of NDVI computed as the mean of the individual values of NDVI computed from the original 30-meter TM pixels. Presumably, this represents a more accurate spatial integration of the NDVI function over the 480 x 480 meter window.

The results shown in Figure 6.3 indicate that there is a small but systematic trend for the larger scale NDVI to overestimate the spatially integrated value of the NDVI function. The fact that the FIFE site is relatively homogeneous and the variability in red and NIR reflectances is fairly small probably accounts for the fact that the deviations from the 1:1 line shown in Figure 6.3 are fairly small. However, the overestimation is systematic, and it is useful to determine whether the amount of the overestimation can be quantified with Equation (6.4).

For the function relating the input red and NIR reflectances to the NDVI, the partial derivatives required for Equation (6.4) are given by:

$$\frac{\partial^2 f}{\partial \rho_{NIR}^2} = \frac{-4\rho_{RED}}{(\rho_{NIR} + \rho_{RED})^3}, \qquad (6.6a)$$

$$\frac{\partial^2 f}{\partial \rho_{RED}^2} = \frac{4\rho_{NIR}}{(\rho_{NIR} + \rho_{RED})^3} \qquad (6.6b)$$

and:

$$\frac{\partial^2 f}{\partial \rho_{NIR}\, \partial \rho_{RED}} = \frac{2(\rho_{NIR} - \rho_{RED})}{(\rho_{NIR} + \rho_{RED})^3}. \tag{6.7}$$

$(NDVI)_{LUMP}$ is defined as:

$$(NDVI)_{LUMP} = f(\bar{\rho}_{NIR}, \bar{\rho}_{RED}). \tag{6.8}$$

Substituting Equations (6.6-6.8) into Equation (6.4), the difference between the mean of the distributed values of NDVI ($(NDVI)_{MODV}$) and the values computed with averaged (lumped) red and NIR reflectances ($(NDVI)_{LUMP}$) is expressed as:

$$(NDVI)_{MODV} - (NDVI)_{LUMP} = \left[1/2 \left(\frac{\partial^2 f}{\partial \rho^2_{NIR}} \sigma^2_{NIR} + \frac{\partial^2 f}{\partial \rho^2_{RED}} \sigma^2_{RED} \right) \right]$$

$$+ \frac{\partial^2 f}{\partial \rho_{NIR} \partial \rho_{RED}} \sigma_{NIR}\, \sigma_{RED}\, \rho_{NIR,RED}. \tag{6.9}$$

The variances of the red and NIR reflectances and the covariance between them were computed for each window.

The values of the differences between $(NDVI)_{MODV}$ and $(NDVI)_{LUMP}$ predicted with Equation (6.9) and those actually observed are shown in Figure 6.4. The solid line in Figure 6.4 is a 1:1 line which represents perfect agreement between the predicted and observed values. The results shown in Figure 6.4 indicate that Equation (6.9) effectively predicts the difference in NDVI computed from mean parameter values and the more accurate spatially integrated NDVI values.

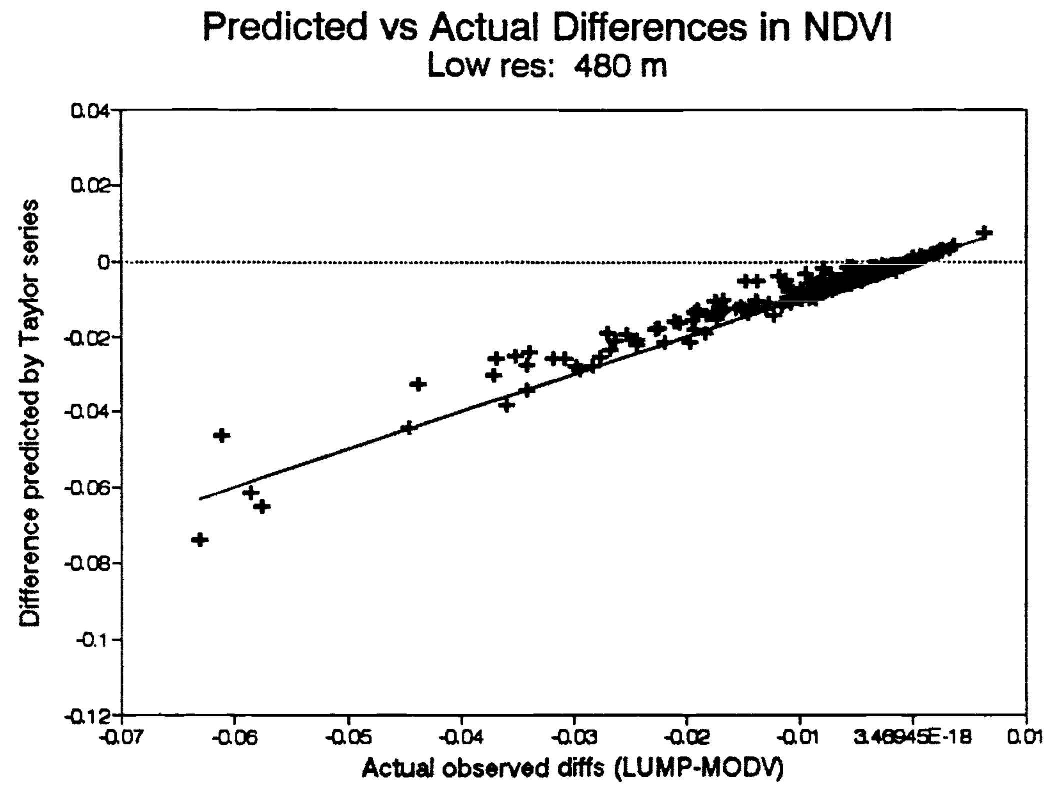

Figure 6.4. The predicted difference between the NDVI values computed from mean RED/NIR values over the window and the areally integrated mean value, calculated from Equation (6.9), versus the observed difference between those two quantities. The size of the averaging window was 480 meters, or 16 x 16 TM Band3/4 pixels.

The quantities plotted in Figure 6.5 are identical to those plotted in Figure 6.3, except that the window size was changed to 960 x 960 meters (32 x 32 TM pixels). This window size simulates an area similar in size to a single AVHRR pixel. There are 256 possible non-overlapping positions for the window in the 512 x 512 TM image and, thus, the results for 256 points are plotted in Figure 6.5. As was the case for the 480 x 480 meter window, the differences in the NDVI that would be estimated from the large-scale sensor and the more accurate spatially integrated mean value are not large, but the data from the larger scale sensor would consistently overestimate the spatially integrated response. It is desirable to see if the differences can be predicted with Equation (6.9).

In Figure 6.6, the differences in NDVI computed for each window predicted by Equation (6.9) are plotted against the actual differences in NDVI observed for each window. The solid line shown in Figure 6.6 is the 1:1 line which represents perfect agreement between the predicted and observed differences in NDVI.

In summary, the analysis described in this section has shown that, for a function which relates spatially variable parameters to a surface characteristic, the spatially integrated value of the function can be quantified in terms of the value of the function evaluated at the mean value for the parameters, plus quantifiable terms which depend on the non-linearity of the function and magnitude of the variance in the input parameters. This approach is embodied in Equation (6.4). The effectiveness of this approach was illustrated by examining, at several spatial scales, the differences in the small-scale spatially integrated value of NDVI and the value of

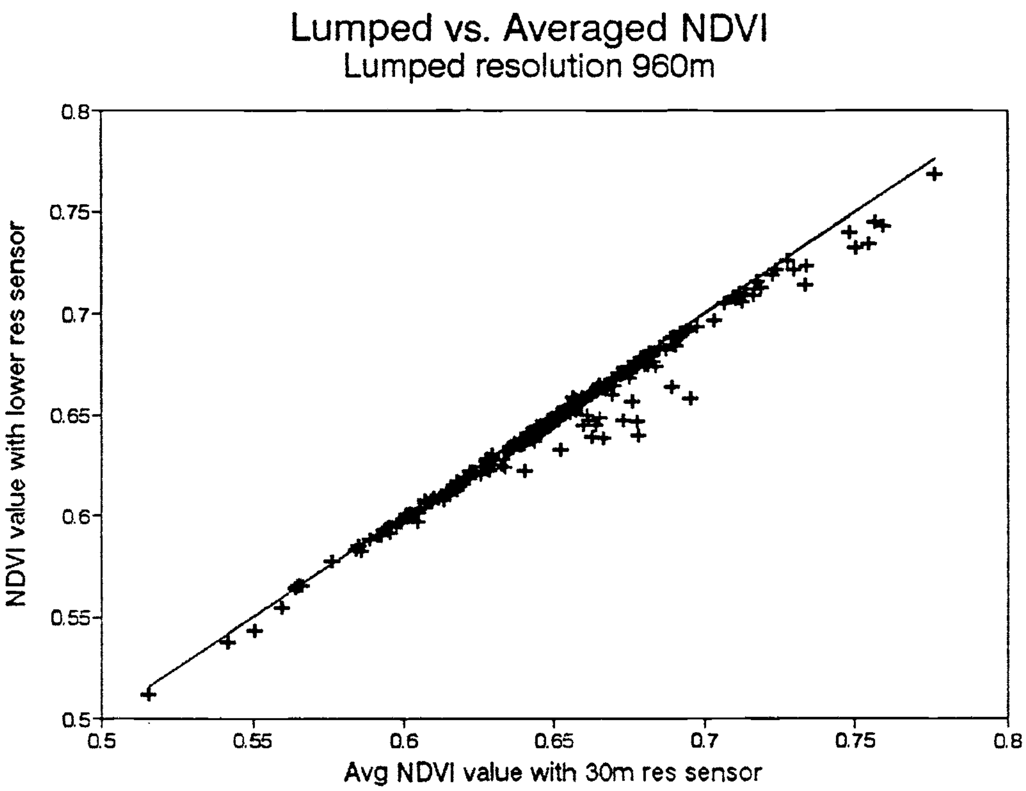

Figure 6.5. Areally integrated average NDVI (computed from individual 30-meter Landsat pixels) plotted against the NDVI computed from the mean values of RED and NIR reflectance for the window. The size of the averaging window was 960 meters, or 32 x 32 TM Band3/4 pixels.

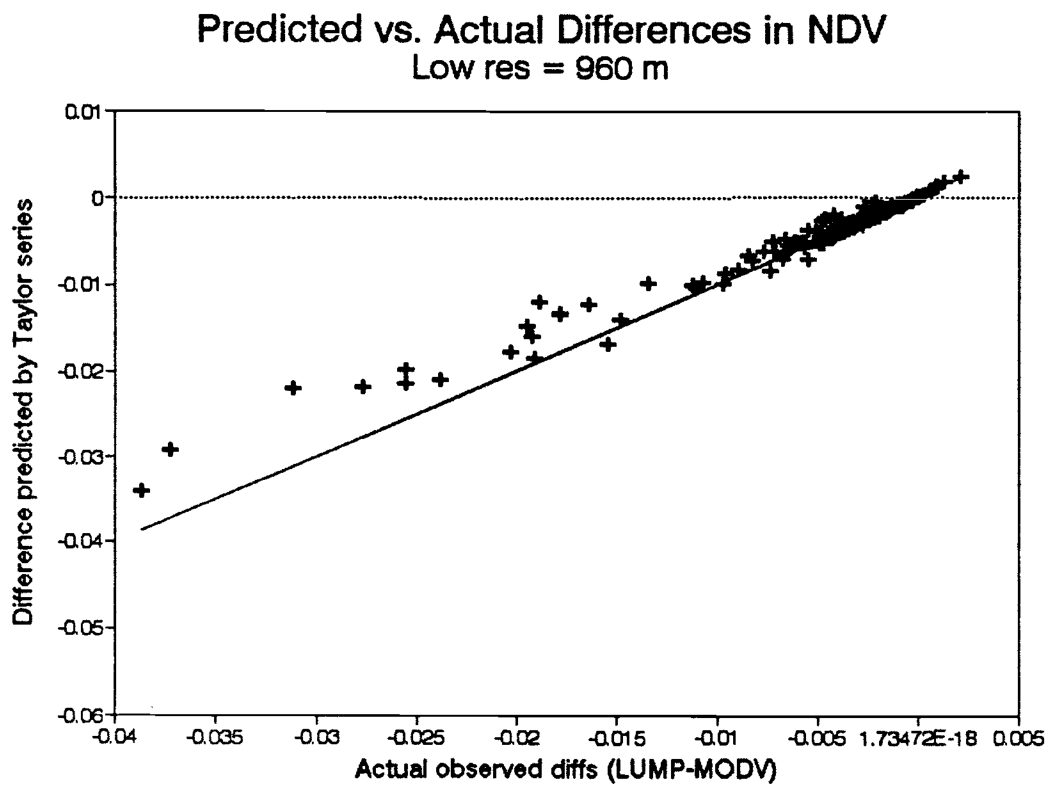

Figure 6.6. The predicted difference between the NDVI values computed from mean RED/NIR values over the window and the areally integrated mean value, calculated from Equation (6.9) versus the observed difference between those two quantities. The size of the averaging window was 960 meters, or 32 x 32 TM Band3/4 pixels.

NDVI computed with mean values of input parameters, such as those measured with larger-scale sensors.

The validity of this approach for relatively simple but non-linear functions which relate spatially variable input parameters to spatially integrated response has important implications for providing a mechanism by which spatially integrated responses at larger scales can be quantified in terms of the variance in the parameters observed at smaller scales. If the spatially variable input parameters and the output response are related through a complicated model or expression which cannot be differentiated analytically, perhaps the second derivative of the function with respect to certain parameters could be evaluated by numerical sensitivity studies.

In considering the applications for this approach, it should also be noted that it could be applied at a variety of scales. For instance, over the spatial scales selected for the NDVI example, the red and NIR reflectances were considered as an "input", and the NDVI value was the function output. At a smaller spatial scale, the red and NIR reflectances could be considered as an output of a complicated soil/canopy reflectance function with spatially variable inputs (such as leaf distribution, density, soil and vegetation transmittance and reflectance, etc.) This same approach could be used to understand how the red and NIR reflectances, treated as a spatially integrated "output" of soil/canopy reflectance models, could be described in terms of the variance of input parameters, the magnitude of the second derivative of output reflectance with respect to those parameters, and the covariances between the parameters, in the manner described by Equation (6.4).

There is one additional implication of this analysis for the specific example shown with NDVI values. This analysis provided an analytical expression which quantifies the difference between NDVI values computed from coarse-resolution remotely sensed data and the value of NDVI computed from fine-resolution data. Usually, the most accurate values of NDVI are desired for an area of interest, but high-resolution data are available over a particular area on occasion (e.g., TM data) Low-resolution data (e.g., AVHRR data) are available more frequently. The expressions derived here provide a methodology by which the occasional high-resolution data could be used to monitor the variability of the reflectances observed in the data with finer resolution. With knowledge of the variance in the reflectances at the smaller scale, then the estimates of NDVI from the larger-scale data could be adjusted by use of Equation (6.9) to obtain more accurate estimates of NDVI for a particular area.

Evaluation of Variance of Parameters Used to Estimate Fluxes

The remotely sensed input data used in combination with ground-based data to estimate the spatially distributed fluxes described in Chapter 5 were evaluated for variability within windows of increasing spatial scale. The purpose of this evaluation was to estimate the approximate size of the variance term for each parameter which would be used in a formulation similar to Equation (6.4) to relate the fluxes computed with larger-scale data to variability in the input parameters at a smaller scale.

Given this intended purpose, the evaluation of the variability of the remotely sensed input data was performed in a manner quite different from the usual procedure for computing a semi-variogram for a two-dimensional grid of data. Although a typical semi-variogram analysis would provide a more comprehensive estimate of the spatial variability of the input data, the method used here was selected because it provides an estimate of the size of the variance terms in Equation (6.4) for windows of various sizes. At a given spatial scale of interest, the variance in a moving window such as that described in the previous analysis was computed for each position of the window. The variances computed for each window position were then averaged to obtain the values of "mean variance" or "mean standard deviation" for a given spatial scale. The number of windows contributing to this mean value of variance and standard deviation varied according to the spatial scale of the window.

Using this procedure, the average value of the standard deviation in all of the windows was computed as a function of window size for the TM Band 3 reflectances, TM Band 4 reflectances, surface temperature, and net solar radiation. The results for the TM Band 3 and 4 reflectances are shown in Figure 6.7. The results show that the variance of the red reflectance is not very significant at any spatial scale for the window size. The size of the variance in the windows for the NIR reflectances is fairly significant and reaches a maximum at a window size of about 1600 meters. These results are consistent with the fact that most of the significant changes in vegetation density over the experimental site, which would give rise to significant changes in NIR reflectance, occur over a spatial scale of about 1600 meters.

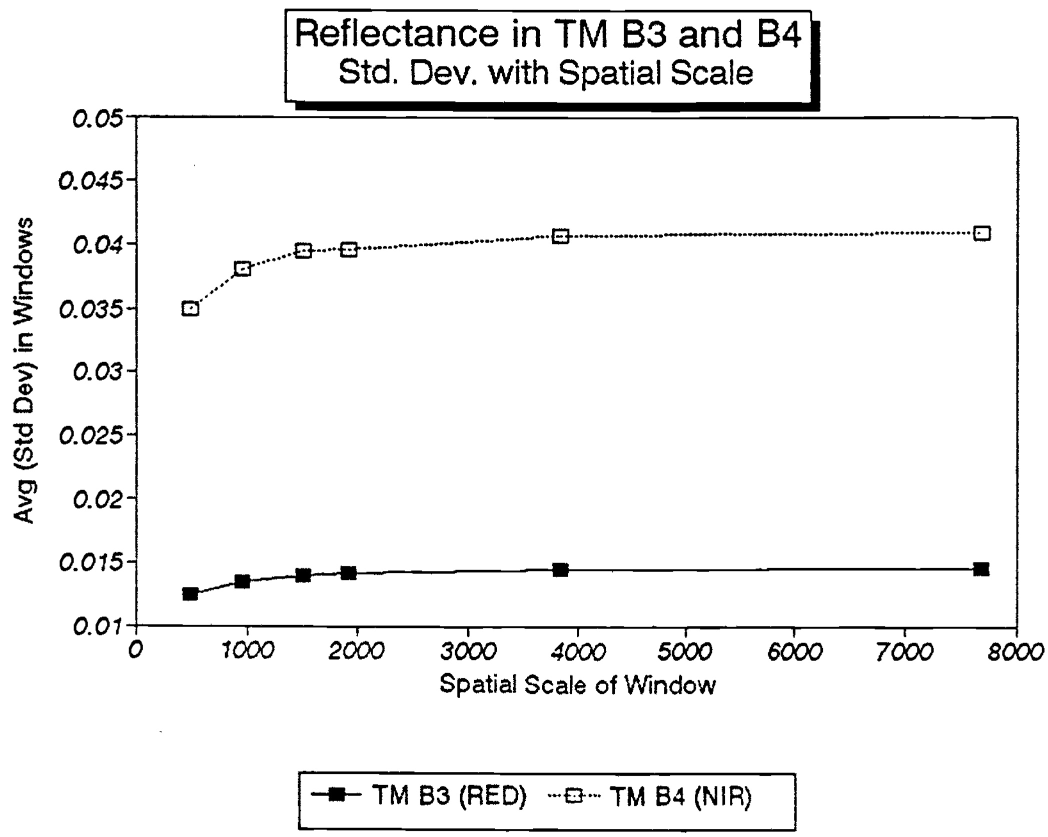

Figure 6.7. The value of standard deviation in surface reflectance observed within an averaging window, averaged over all of the non-overlapping positions of the averaging window, plotted as a function of the spatial scale of the averaging window.

The average values of standard deviation of surface temperature as a function of window size are shown in Figure 6.8. The surface temperature shows increasing variance as the size of the window is increased, with most of the increase in variance occurring within a window up to 2000 meters in scale.

The average values of standard deviation in net solar radiation as a function of window size are shown in Figure 6.9. Because the variations in net solar radiation are driven primarily by slope, most of the variation in net solar radiation occurs within windows less than 500m in spatial scale. This is consistent with the length scales between opposing slopes at the field site.

Spatial Scaling of Fluxes

The approach outlined above, which describes the spatial scaling of an output response in terms of the variability of the input parameters at increasing spatial scales, was evaluated for application to the spatial scaling of the surface fluxes computed with a combination of ground-based and remotely sensed data. While the approach was useful for understanding the spatial scaling of the derived vegetation indices, it is not clear that it is particularly useful to apply it to the formulations for the spatially distributed surface fluxes given in Chapter 5. The applicability of the approach for each of the computed surface fluxes is summarized below.

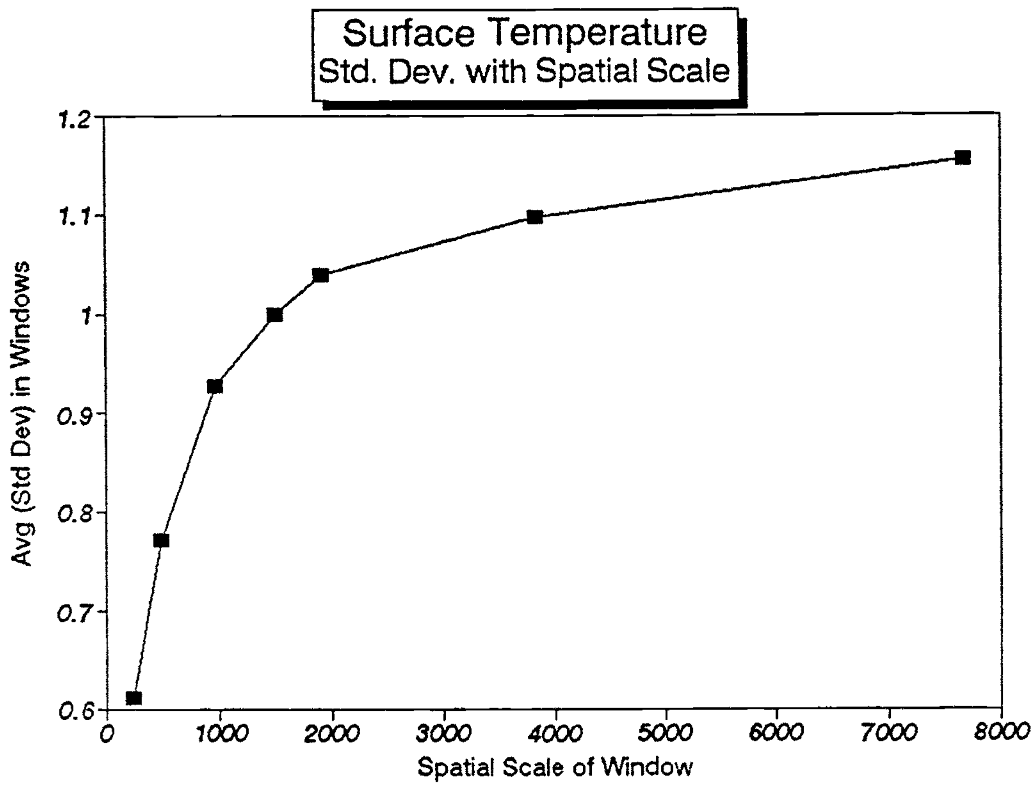

Figure 6.8. The value of standard deviation in surface temperature observed within an averaging window, averaged over all of the non-overlapping positions of the averaging window, plotted as a function of the spatial scale of the averaging window.

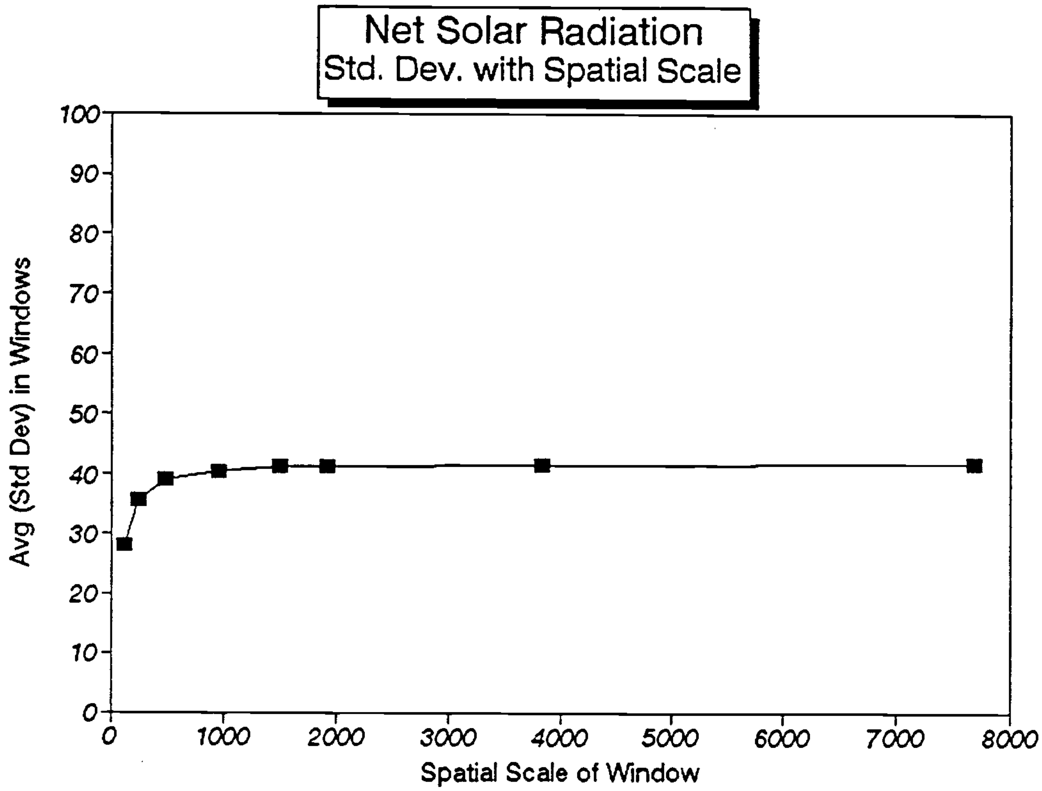

Figure 6.9. The value of standard deviation in net solar radiation observed within an averaging window, averaged over all of the non-overlapping positions of the averaging window, plotted as a function of the spatial scale of the averaging window.

Net Radiation (R_{net})

As described in the previous chapter, the R_{net} was computed by correcting the net solar radiation ($R_{net,solar}$) given by Dubayah et al. (1990) for the effects of incoming and outgoing long-wave radiation. The magnitude of the net long-wave term was, on the average, approximately 100 Wm^{-2}. Because the near-surface air temperature and vapor pressure values were assumed to be constant over the site, the incoming long-wave radiation was constant. The outgoing long-wave radiation is primarily a function of surface temperature, but at the mid-morning overpass time of the TM sensor, the variations in the outgoing long-wave radiation resulting from changes in surface temperature were small compared to the effects of slope on the net solar radiation. Thus, the spatial variations in total net radiation are dominated by the variations in net solar radiation, and the variability of the net total radiation will change with increasing spatial scale in a manner very similar to the net solar radiation evaluated in the previous section.

Soil Heat Flux (G)

The function provided in previous chapters to estimate the soil heat flux for the site expresses the soil heat flux as a linear function of the total net radiation and the NDVI. Hence, the second derivative of the output flux with respect to those derived input quantities is zero. The input quantities are derived from non-linear functions of remotely sensed inputs, but the spatial scaling of those inputs have been previously described above.

Sensible Heat Flux (H)

The expression for the sensible heat flux derived in previous chapters and used to create the map of distributed sensible heat flux for the site is given by:

$$H = \rho C_p \left((1-b)\,(T_s - T_a) - a\right)/r_a, \tag{6.10}$$

where H is the sensible heat flux (Wm^{-2}), ρC_p is heat capacity of air ($Jm^{-3}C^{-1}$), a and b are constants, T_s is the surface temperature (°C), T_a is the air temperature (°C), and r_a is the aerodynamic resistance given by Equations (4.9) and (4.10). This expression for H is linear in surface temperature, except for the dependence of the stability corrections embedded in r_a on (T_s-T_a). Thus, an analysis of the variability of H based on Equation (6.4) would depend strongly on the expressions for estimating the r_a parameter. In the previous chapter, the roughness parameters which dominate the r_a term were identified in Chapter 5 to be a major source of uncertainty in the estimation of H. They were computed fairly reliably for the grassland pixels as a function of the NDVI, the variation of which has been analyzed above. For the remaining pixels in the image over the FIFE experimental site (agricultural, bare soil, and woody vegetation areas), these roughness parameters were set to a constant value, which introduced considerable uncertainty into the estimate of H for the non-grassland pixels. Therefore, an analysis of the variability of H which depended strongly on the somewhat tenuous formulation for r_a would not seem to be productive at this time.

Summary and Conclusions

An approach for quantifying derived outputs of a non-linear function with spatially variable inputs was described and tested. This approach describes the spatially integrated response of a non-linear function in terms of the variance in the input parameters and the non-linearity of the function with respect to those parameters. The approach was found to be very useful in describing the behavior of one product derived from remotely sensed input as a function of increasing spatial scale--the Normalized Difference Vegetation Index (NDVI). However, because of the particular structure of the formulations for the surface fluxes derived in the previous chapters as optimal for estimating the energy fluxes over the FIFE experimental site with remotely sensed data, this approach was not particularly effective for describing the variability of surface fluxes with respect to remotely sensed inputs.

However, although not directly applicable to this particular formulation for fluxes, this approach seems to be a good one for ultimately understanding the response of non-linear functions over areas with spatially variable parameters. The problem of having spatially variable input into a non-linear function to give some spatially integrated mean output is at both "ends" of the hydrology/remote sensing problem. It is interesting to note that this type of approach to a non-linear function with spatially variable input parameters has been mentioned by researchers trying to describe both the hydrologic response (Milly and Eagleson, 1987) and the remote sensing system response (Becker and Raffy, 1987). When utilizing remotely sensed data for hydrologic applications, one is concerned with a spatial distribution of hydrologic parameters as well as a spatial distribution of remote sensing observations. An important improvement in the utilization of remotely sensed data in hydrology may ultimately occur when the distribution of remote sensing observables can be used to solve for a distribution of hydrologic parameters.

CHAPTER 7

SUMMARY

Motivation

The overall topic of the research described in this dissertation was the partitioning of available energy at the Earth's surface into sensible and latent heat flux, with an emphasis on the development of techniques which utilize remotely sensed data. Previous researchers had demonstrated the use of remote sensing data to estimate these fluxes over agricultural surfaces with nearly complete vegetation cover. Hence, the emphasis in this research was to investigate the extension and modification of those techniques to estimate surface fluxes over areas with "natural" vegetation (i.e., non-agricultural vegetation types with variable and incomplete canopy cover).

If techniques can be developed which reliably estimate surface energy fluxes with remotely sensed data over a variety of surface types, then surface energy fluxes can be computed in a spatially distributed manner. Spatially distributed estimates of surface energy fluxes provide a fundamentally new tool in the investigation of regional water and energy balance and for the study of land-surface/atmosphere interactions and feedback processes.

Results and Conclusions

The primary activities and results described in this dissertation can be summarized as follows:

- One of the simplest expressions for estimating the partitioning of available energy into sensible and latent heat flux under non-moisture limiting conditions (the Priestley-Taylor equation) was examined with the intent to quantify the factors controlling the α parameter. An algebraic relationship was derived between the α parameter and the variables introduced in the Penman-Monteith combination equation. Using a range of values for meteorological forcing variables and typical values of surface variables for different surface types (e.g., open water, short grass, and forests), it was shown that the range of α values predicted was consistent with the range of values reported in the literature for different surface types. The significance of this result is that it provides a quantitative basis for some of the empirical observations of the behavior of the α parameter widely reported in the literature (i.e., highly variable values over forests, less variability over short grass and open water, seasonal and diurnal variations over most surfaces).
- In order to pursue the main objective of quantifying the partitioning of available energy for natural ecosystems (i.e., surfaces with non-agricultural vegetation types, variable and incomplete vegetation cover,

and varying moisture supply), the focus was narrowed to the site of the First ISLSCP Field Experiment (FIFE). Ground-based measurements of surface fluxes, vegetation cover, and surface and root-zone soil moisture were used to examine the factors controlling the partitioning of energy at ground stations with contrasting surface characteristics. It was shown that the processes of soil evaporation and vegetation transpiration vary considerably with time after a precipitation event, depending on the soil moisture availability in the root zone and at the surface. Under some conditions, the root-zone soil moisture was quite different from the near-surface (approximately 0-5 cm depth) soil moisture; thus, there was no consistent relationship between vegetation transpiration and near-surface soil moisture. (Only near-surface soil moisture can be estimated directly from remotely sensed data.) The significance of this analysis is that it provided experimental evidence that it is very difficult to quantify (even for a relatively simple surface consisting of bare soil and a single dominant vegetation type) the various physical processes contributing to the total latent heat flux with only the few surface characteristics which can be derived from remotely sensed data.

- A relatively simple surface energy balance approach for estimating latent heat flux was developed and tested using helicopter-based and satellite-based data acquired directly over ground-based flux stations at the FIFE experimental area. Ground-based flux measurements from approximately 12 FIFE ground stations were used to calibrate expressions which related remotely sensed reflectances and temperatures to soil heat flux and sensible heat flux at the local scale (i.e., using 30-100 meter pixels similar in scale to the fetch areas of the ground-based surface flux stations). For the estimation of sensible heat flux (H), a relationship between the surface-aerodynamic temperature difference (T_s-T_o) and the surface-air temperature difference (T_s-T_a) was empirically derived. This relationship was relatively consistent for data sets acquired over various time periods and with different sensors. Further investigation of this technique is required to determine its applicability to other areas.

- The algorithms derived from the analysis of ground-based fluxes and extracts of satellite data over those stations were then applied on a pixel-by-pixel basis to data from a Landsat 5-TM scene from August 15, 1987 to develop a map of "instantaneous", spatially distributed surface energy fluxes over the FIFE experimental area. The spatially distributed net radiation was computed by correcting the net solar radiation map produced by Dubayah et al. (1990) for net long-wave radiation. The soil heat flux and sensible heat flux values were estimated using atmospherically corrected, satellite-based reflectances and temperatures and ground-based estimates of near-surface temperature and windspeed. The latent heat flux was estimated as the residual quantity in the energy-balance equation for each pixel. These results demonstrated the feasibility and utility of estimating spatially distributed surface fluxes with remotely sensed data. For the time period of the TM overpass on August 15, 1987, the latent heat flux was shown to be dependent on the available energy, which was strongly influenced by the topographically induced variations in incoming radiation.

- Last, a preliminary framework was provided for a methodology to quantify the effect of spatial scaling on parameters derived from remotely sensed data. In this approach, the difference between the mean of the distributed response of a non-linear function and the value of the non-linear function computed with spatially aggregated (i.e., "lumped" parameters was quantified. As an example of the utility of this approach, NDVI values for the FIFE experimental area were computed with input data of variable spatial resolution. The differences in the values of NDVI computed at different spatial resolutions were accurately predicted by an equation which quantified those differences in terms of variability in input parameters (i.e., red and near-infrared reflectance) and the degree on non-linearity of the function relating the input variables to the derived parameter (NDVI). The success of this approach suggests that it may be useful for other parameters derived from remotely sensed data or other hydrological modeling applications which involve the scaling of non-linear functions of spatially distributed variables.

Suggestions for Future Research

The use of a combination of ground-based and remotely sensed data to estimate the surface energy-balance components over surfaces with partial vegetation cover is a relatively new topic of research. There are many issues which need to be addressed in more detail, some of which are outlined below. When the research described in this dissertation was first undertaken, the FIFE experiment was one of the only field campaigns designed to address this topic which was carried out over a predominantly non-agricultural field area. In the intervening years, the value of carrying out these types of field experiments over different types of surfaces has become increasing evident. Several other field experiments have been organized with this topic in mind and have included the acquisition of surface flux data, atmospheric boundary layer data, and remotely sensed data. These experiments include the MONSOON '90 field experiment, carried out at the Walnut Gulch Experimental Watershed in southeastern Arizona, several of the MAC (Multi-Aircraft-Campaigns)-Europe campaigns, and the HAPEX-Sahel experiment.

All of the suggested areas of research delineated below would benefit from the application of data from as many different types of surfaces as possible. The investigation of these issues by using data from any of these individual experiments is an important first step on these topics. However, the eventual goal should be to compare and contrast the results from these various campaigns, as well as those carried out over agricultural surfaces. In this way, the physical effects of site-specific characteristics (such as vegetation type and structure, moisture regime, and climate) can be better understood, and the limits of applicability of various techniques can be identified.

(A) Single-layer energy-balance approach

(1) Estimation of sensible heat (H)

(a) Utilize data from other experiments carried out over surfaces with partial vegetation cover, such as the MONSOON '90 or HAPEX-Sahel experiment, to examine the relationship between surface temperature, aerodynamic temperature and aerodynamic resistance; and

(b) Investigate the feasibility of obtaining spatially distributed information relating to aerodynamic roughness parameters from remotely sensed data (e.g., laser altimeter or radar data).

(2) The estimation of soil heat flux from values of net radiation and remotely sensed variables

Most of the previous work on this topic has been done over agricultural-type canopies with significantly different structural and optical properties than those in non-agricultural areas. Using data acquired over various non-agricultural surfaces from the field campaigns described above, the following topics should be investigated:

(a) Relationships between the ratio of G/R_{net} and vegetation indices for various vegetation types and under various observational conditions (i.e., solar angles and sensor view angles); and

(b) The effects of physical factors which would be expected to influence the soil heat flux, such as the diurnal heating cycle and soil moisture. If these factors are significant, can they be modeled or estimated with remotely sensed observations?

(3) The relationship between the instantaneous flux estimates derived from remotely sensed observations and daily values for energy-balance components.

(a) This investigation should be extended from the agricultural, clear sky conditions of previous work to the non-agricultural, naturally variable conditions observed in many of the field campaigns mentioned above.

(B) Multi-layer modeling approaches to the estimation of surface energy fluxes with remotely sensed data

(1) New and existing models which quantify the soil and vegetation components of the surface energy-balance separately could be investigated with data from the FIFE Experiment as well as the other field campaigns mentioned above. An important objective in the development and modification of these models should be to keep the number of controlling parameters and variables to the minimum number necessary to describe the dominant processes.

(2) The utility of combining different remotely sensed data types (e.g., microwave estimates of soil moisture, thermal band measurements of surface temperature, and vegetation cover estimates from visible/NIR remotely sensed data) in multi-layer modeling should be specifically investigated with data from multiple field campaigns.

(C) Quantify the spatial resolution of surface fluxes useful to the study of land-surface/atmosphere interactions

(1) An important motivation for this research was to develop techniques to estimate spatially distributed surface fluxes that could be used as improved boundary conditions for models which describe atmospheric boundary layer processes or in truly coupled models of land-surface/atmosphere processes. Simulation studies should be carried out with mesoscale atmospheric models, using various distributed surface flux boundary conditions typical of those observed with remotely sensed data over natural ecosystems. These studies would provide a better quantitative understanding of the integrating effects of the ABL and would help to quantify the surface resolution required in the estimation of spatially distributed surface fluxes with remotely sensed data.

REFERENCES

Arya, S.P., 1988, Introduction to Micrometeorology, Academic Press, Inc., San Diego, California.

Asrar, G., M. Fuchs, E.T. Kanemasu, and J.L. Hatfield, 1984, Estimating absorbed photosynthetic radiation and leaf area index from spectral reflectance in wheat, *Journal of Agronomy*, 76:300-306.

Barton, I.J., 1979, A parameterization of the evaporation from nonsaturated surface, *Journal of Applied Meteorology*, 18:43-47.

Becker, F. and M. Raffy, 1987, Problems related to the determination of land surface parameters and pluxes over heterogeneous media from satellite data, *Advances in Space Research*.

Black, T.A., 1979, Evapotranspiration from Douglas fir stands exposed to soil water deficits, *Water Resources Research*, 15(1):164-170.

Bouchet, R.J., 1963, Evapotranspiration reelle et potentielle, signification climatique, Publ. 62, pp. 134-142, Int. Assoc. Sci. Hydrol., Gentbrugge, Belgium.

Bowen, I.S., 1926, The ratio of heat losses by conduction and by evaporation from any water surface, *Physics Review*, 27, 779-787.

Brutsaert, W.H., 1975, On a derivable formula for long-wave radiation from clear skies, *Water Resources Research*, 11, 742-744.

Brutsaert, W.H., 1982, Evaporation Into the Atmosphere, D. Reidel Publ. Co., London, England, 299 p.

Brutsaert, W.H., 1986, Catchment-scale evaporation and the atmospheric boundary layer, *Water Resources Research*, 22:9, 39S-45S.

Brutsaert, W.H. and H. Stricker, 1979, An advection-aridity approach to estimate actual regional evapotranspiration, *Water Resources Research*, 15:2, 443-450.

Camillo, P.J., R.J. Gurney, and T.J. Schmugge, 1983, A soil and atmospheric boundary layer model for evapotranspiration and soil moisture studies, *Water Resources Research*, 19(2), 371-380.

Carlson, T.N., J.K. Dodd, S.G. Benjamin, and J.N. Cooper, 1981, Satellite estimation of the surface energy balance, moisture availability and thermal inertia, *Journal of Applied Meteorology*, 20:67-87.

Carlson, T.N. and F.E. Boland, 1978, Analysis of urban-rural canopy using a surface heat flux/temperature model, *Journal of Applied Meteorology*, 17:998-1013.

Charney, J.G., W.J. Quirk, S.H. Chow, and J. Kornfield, 1977, A comparative study of the effects of albedo change on drought in semi-arid regions, *Journal of Atmospheric Science*, 34:1366-85.

Choudhury, B.J. and S.B. Idso, 1985, An empirical model for stomatal resistance of field-grown wheat, *Agricultural and Forest Meteorology*, 36:65-82.

Choudhury, B.J. and J.L. Monteith, 1988, A four-layer model for the heat budget of homogeneous land surfaces, *Quarterly Journal of the Royal Meteorological Society*, 114: 373-398.

Choudhury, B.J., R.J. Reginato, and S.B. Idso, 1986, An analysis of infrared temperature observations over wheat and calculation of latent heat flux, *Agricultural and Forest Meteorology*, 37:75-88.

Choudhury, B.J. and J.L. Monteith, 1986, Implications of stomatal response to saturation deficit for the heat balance of vegetation, *Agricultural and Forest Meteorology*, 36:215-225.

Clothier, B.E., K.L. Clawson, P.J. Pinter, Jr., M.S. Moran, R.J. Reginato, and R.D. Jackson, 1986, Estimation of soil heat flux from net radiation during the growth of alfalfa, *Agricultural and Forest Meteorology*, 37:319-329.

Davies, J.A. and C.D. Allen, 1973, Equilibrium, potential and actual evaporation from cropped surfaces in southern Ontario, *Journal of Applied Meteorology*, 12:649-657.

Davis, F.W., J. Michaelson, R. Dubayah, and J. Dozier, 1990, Proceedings of the American Meteorological Society Symposium on the First ISLSCP Field Experiment, Anaheim, California.

Deardorff, J.W., 1978, Efficient predictions of ground surface temperature and moisture, with inclusion of a layer of vegetation, *Journal of Geophysical Research*, 83(C4):1889-1903.

de Bruin, H.A.R., 1983, A model for the Priestley-Taylor, *Journal of Applied Meteorology*, 22:572-578.

de Bruin, H.A.R. and J.Q. Keijman, 1979, The Priestley-Taylor evaporation model applied to a large shallow lake in the Netherlands, *Journal of Applied Meteorology*, 18: 898-903.

Dickinson, R.E., A. Henderson-Sellers, P.J. Kennedy, and M.F. Wilson, 1986, Biosphere-atmosphere transfer scheme (BATS) for the NCAR Community Climate Model, National Center for Atmospheric Research, Tech. Note, TN275.

Dubayah, R., J. Dozier, and F.W. Davis, 1990, Topographic distribution of clear-sky radiation over the Konza Prairie, Kansas, *Water Resources Research*, 26:679-690.

Eagleson, P.S., 1982, Hydrology and climate, in Scientific Basis of Water Resource Management, 127 p., National Academy Press, Washington, D.C.

Eagleson, P.S., 1986, The emergence of global-scale hydrology, *Water Resources Research*, 22(9):6S-14S.

Flint, A.L. and S.W. Childs, 1991, Use of the Priestley-Taylor evaporation equation for soil water limited conditions in a small forest clearcut, *Agricultural and Forest Meteorology*, 56:247-260.

Fortin, J.P. and B. Seguin, 1975, Estimation de l'ETR regionale a partir de l'ETP locale: utilisation de la relation de Bouchet a differentes echelles de temps, *An. Agron*. 26:537-554.

Fraser, R.S., Y. Kaufam, R. Ferrare, S. Mattoo, 1989, Algorithm for atmospheric correction of aircraft and satellite imagery, NASA Technical Memorandum Number 100751.

Fritchen, L.J. and P. Qian, 1990, Energy blance components from six sites in a native prairie, Proceedings of the American Meteorological Society Symposium on the First ISLSCP Field Experiment, Anaheim, California.

Fuchs, M. and C.B. Tanner, 1966, Infrared thermometry of vegetation, *Agronomy Journal*, 58:597-601.

Fuchs, M. and C.B. Tanner, 1970, Error analysis of Bowen ratios measured by differential psychrometry, *Agricultural and Forest Meteorology*, 7:329-334.

Garratt, J.R., 1980, Surface influence upon vertical profiles in the atmospheric near-surface layer, *Quarterly Journal of the Royal Meteorology Society*, 106:803-819.

Goudriaan, J., 1977, Crop Micrometeorology: A Simulation Study, Center for Agricultural Publishing and Documentation, Wageningen, The Netherlands.

Ham, J.M., J.L. Heilman, and R.J. Lascano, 1990, Determination of soil water evaporation and transpiration from energy balance and stem flow measurements, *Agricultural and Forest Meteorology*, 52:287-301.

Ham, J.M., J.L. Heilman, and R.J. Lascano, 1991, Soil and canopy energy balances of a row crop at partial cover, *Agronomy Journal*, 83:744-753.

Hatfield, J.L., 1989, Aerodynamic properties of partial canopies, *Agricultural and Forest Meteorology*, 46:15-22.

Henderson-Sellers, A. and H. Gornitz, 1985, Possible climatic impacts of land-cover transformations with particular emphasis on tropical deforestation, *Climate Change*, 6:231-257.

Holm, R.G., M.S. Moran, R.D. Jackson, P.N. Slater, B. Yuan, and S.F. Biggar, 1989, Surface reflectance factor retrieval from Thematic Mapper data, *Remote Sensing of Environment*, 27:47-57.

Huband, N.D.S. and J.L. Monteith, 1986a, Radiative surface temperature and energy balance of a wheat canopy: I. Comparison of radiative and aerodynamic canopy temperature. *Boundary-Layer Meteorology*, 36:1-17.

Huband, N.D.S. and J.L. Monteith, 1986b, Radiative surface temperature and energy balance of a wheat canopy: II. Estimating fluxes of sensible and latent heat, *Boundary-Layer Meteorology*, 36:107-116.

Huete, A.R., 1988, A soil adjusted spectral vegetation index (SAVI), *Remote Sensing of Environment*, 25:295-309.

Humes, K.S., W.P. Kustas, and M.S. Moran, 1991, Composite surface temperature, soil and vegetation component temperature, and estimation of component contributions to sensible heat flux for a semi-arid shrub-dominated site, Proceedings of the American Meteorological Society, Tenth Conference on Biometeorology and Aerobiology, Salt Lake City, Utah.

Jackson, R.D., S.B. Idso, and R.J. Reginato, 1976, Calculation of evaporation rates during the transition from energy-limiting to soil-limiting phases using albedo data, *Water Resources Research*, 12(1):23-26.

Jackson, R.D., R.J. Reginato, and S.B. Idso, 1977, Wheat canopy temperatures: a practical tool for evaluating water requirements, *Water Resources Research*, 13:651-656.

Jackson, R.D., 1982, Canopy temperature and crop water stress, in Advances in Irrigation, D.I. Hillel (ed.), Academic Press, pp. 43-85.

Jackson, R.D., 1984, Total reflected solar radiation calculated from multiband sensor data, *Agricultural and Forest Meteorology*, 33:162-174.

Jackson, R.D., 1985, Evaluating evapotranspiration at local and regional scales, *Proc. of the IEEE, Trans. Geoscience and Remote Sensing*, 73:1086-1096.

Jackson, R.D., M.S. Moran, L.W. Gay, and L.H. Raymond, 1987, Evaluating evaporation from field crops using airborne radiometry and ground-based meteorological data, *Irrigation Science*, 8:81-90.

Jury, W.A. and C.B. Tanner, 1975, Advection modification of the Priestley and Taylor evapotranspiration formula, *Agronomy Journal*, 67:840-842.

Kustas, W.P., B.J. Choudhury, M.S. Moran, R.J. Reginato, R.D. Jackson, and L.W. Gay, 1987, Problems in estimation of sensible heat flux over incomplete canopy cover with thermal infrared data, Proc. of 18th Conference on Agricultural and Forest Meteorology, 15-18 Sept., West Lafayette, Indiana, pp. 87-90.

Kustas, W.P., B.J.Choudhury, M.S. Moran, R.J. Reginato, R.D. Jackson, L.W. Gay, and H.L. Weaver, 1989a, Determination of sensible heat flux over sparse canopy using thermal infrared data, *Agricultural and Forest Meteorology*, 44:197-216.

Kustas, W.P., B.J. Choudhury, K.E. Kunkel, and L.W. Gay, 1989b, Estimate of the aerodynamic roughness parameters over an incomplete canopy cover of cotton, *Agricultural and Forest Meteorology*, 46:91-105.

Kustas, W.P. and C.S.T. Daughtry, 1990, Estimation of the soil heat flux/net radiation ratio from multispectral data, *Agricultural and Forest Meteorology*, 49:205-223.

Kustas, W.P., B.J. Choudhury, Y. Inoue, P.J. Pinter, Jr., M.S. Moran, R.D. Jackson, and R.J. Reginato, 1990, Ground and aircraft infrared observations over a partially vegetated area, *International Journal of Remote Sensing*, 11:409-427.

Laval, K., 1986, General circulation model experiment with surface albedo changes, *Climate Change*, 9:91-102.

Lettau, H., K. Lettau, and L.C.B. Molion, Amazonia's hydrologic cycle and the role of atmospheric recycling in assessing deforestation effect, *Monthly Weather Review*, 107:227-237.

Mahrt, L. and M. Ek, 1984, The influence of atmospheric stability on potential evaporation, *Journal of Climate and Applied Meteorology*, 23:222-234.

Markham, B.L. and J.L. Barker, 1986, Landsat MSS and TM post-calibration dynamic ranges, exoatmospheric reflectances and at-satellite temperatures, EOSAT Landsat Technical Notes, pp. 2-8.

Markham, B.L., F.M. Wood, Jr., and S.P. Ahmad, 1988, Radiometric calibration of the reflective bands of NS001 Thematic Mapper Simulator and Modular Multispectral Radiometers, Proceedings of the SPIE, 924:96-108.

McNaughton, K.G. and T.A. Black, 1973, A study of evapotranpiration from a Douglas-fir forest using the energy balance approach, *Water Resources Research*, 9:1579-1590.

McNaughton, K.G. and T.W. Spriggs, 1986, A mixed-layer model for regional evaporation, *Boundary-Layer Meteorology*, 34:243-263.

McNaughton, K.G. and T.W. Spriggs, 1989, An evaluation of the Priestley and Taylor equation and the complementary relationship using results from a mixed-layer model of the convective boundary layer, in Estimation of Areal Evapotranspiration, IAHS Publ. No. 177, Wallingford, OX10 8BB, United Kingdom.

Milly, P.C.D. and P.S. Eagleson, 1987, Effects of spatial variability on annual average water balance, *Water Resources Research*, 23, 11:2135-2143.

Mintz, Y., 1984, The sensitivity of numerically simulated climates to land-surface boundary conditions, in The Global Climate, Edited by J.T. Houghton.

Monteith, J.L., 1973, Principles of Environmental Physics, Elsevier Press, New York, 241 p.

Monteith, J.L., 1981, Evaporation and surface temperature, *Quarterly Journal of the Royal Meteorological Society*, 107:1-27.

Moran, M.S., 1990, R.D. Jackson, L.H. Raymond, L.W. Gay, and P.N. Slater, Mapping surface energy balance components by combining Landsat Thematic mapper and ground-based meteorological data, *Remote Sensing of Environment*, 30:77-87.

Moran, M.S., 1990, A satellite-based approach for evaluation of the spatial distribution of evapotranspiration from agricultural lands, Ph.D. Dissertation, The University of Arizona, Tucson, Arizona, 205 p.

Morton, F.I., 1970, Estimating evaporation and transpiration from climatological observations, *Journal of Applied Meteorology*, 14:488-497.

Mukammal, E.I. and H.H. Neumann, 1977, Application of the Priestley-Taylor evaporation model to assess the influence of soil moisture on the evaporation from a large weighing lysimeter and class A pan, *Boundary-Layer Meteorology*, 12:243-256.

Nicholson, S.E., 1988, Land surface-atmosphere interaction: physical processes and surface changes and their impact, in *Progress in Physical Geography*, 12, 36-65.

Nie, D. and E. Kanemasu, 1990, Effect of topography on energy balance in a tallgrass prairie, Proceedings of the American Meteorological Society Symposium on the First ISLSCP Field Experiment, Anaheim, California.

Penman, H.L., 1948, Natural evaporation from open water, bare soil, and grass, *Proceedings of the Royal Society*, Ser. A. 193, 120-146.

Penman, H.L., 1963, Vegetation and Hydrology, Tech. Communication 53, Commonwealth Bureau of Soils, Harpenden, United Kingdom.

Price, J.C., 1980, The potential of remotely sensed thermal infrared data to infer surface soil moisture and evaporation, *Water Resources Research*, 16:787-795.

Price, J.C., 1982, Estimation of regional scale evapotranspiration through analysis of satellite thermal-infrared data, *IEEE Trans. Geoscience and Remote Sensing*, 20:286-292.

Priestley, C.H.B., 1959, Turbulent Transfer in the Lower Atmosphere, University of Chicago Press, Chicago, Illinois, 130 p.

Priestley, C.H.B. and R.J. Taylor, 1972, On the assessment of surface heat flux and evaporation using large-scale parameters, *Monthly Weather Review*, 100 (2):81-92.

Reginato, R.J., R.D. Jackson, and P.J. Pinter, 1985, Evaporation calculated from remote multispectral and ground station meteorological data, *Remote Sensing of Environment*, 19:75-89.

Rosema, A., J.H. Bijleveld, P. Reiniger, G. Tassone, K. Blyth, and R.J. Gurney, 1978, TELL-US, a combined surface temperature, soil moisutre and evaporation mapping approach, Proceedings of the 12th International Symposium on Remote Sensing of Environment, Ann Arbor, Michigan, pp. 2267-2276.

Rowntree, P.R. and J.A. Bolton, 1983, Simulation of the atmopheric response to soil moisture anomalies over Europe, *Quarterly Journal of the Royal Meteorology Society*, 109:501-526.

Salati, E. and P. Vose, 1984, The Amazon basin: a system in equilibrium, *Science*, 225:129-138.

Seguin, B. and B. Itier, 1983, Using midday surface temperature to estimate daily evaporation from satellite thermal IR data, *International Journal of Remote Sensing*, 4:371-383.

Sellers, P.J., Y. Mintz, Y.C. Sud, and A. Dalcher, 1986, A simple biosphere model (SiB) for use within general circulation models, *Journal of Atmospheric Science*, 43:505-531.

Sellers, P.J. and F.G. Hall, 1987, FIFE Experiment Plan, NASA Internal Document, 623 NASA/GSFC, Greenbelt, Maryland 20771, 141 p.

Sellers, P.J., F.G. Hall, G. Asrar, D.E. Strebel, and R.E. Murphy, 1988, *Bulletin of the American Meteorological Society*, 69(1):22-27.

Sellers, P.J., F.G. Hall, D.E. Strebel, R.D. Kelly, S.B. Verma, B.L. Markham, B.L. Blad, D.S. Schimel, J.R. Wang, and E. Kanemasu, 1990, 'FIFE Interim Report', NASA Internal Document, 623 NASA/GSFC, Greenbelt, Maryland 20771.

Sellers, W.D., 1965, Physical Climatology, University of Chicago Press, Chicago, Illinois, 272 p.

Shukla, J. and Y. Mintz, 1982, Influence of land-surface evapotranspiration on the earth's climate, *Science*, 215:1498-1501.

Shuttleworth, W.J., 1988a, Macrohydrology--the new challenge for process hydrology, *Journal of Hydrology*, 100:31-56.

Shuttleworth, W.J., 1988b, Evaporation from Amazonian rainforest, *Proceedings of the Royal Society of London*, Ser. B, 233:321-346.

Shuttleworth, W.J. and I.R. Calder, 1979, Has the Priestley-Taylor equation any relevance to forest evaporation?, *Journal of Applied Meteorology*, 18:639-646.

Shuttleworth, W.J. and J.S. Wallace, 1985, Evaporation from sparse crops--an energy combination theory, *Quarterly Journal of the Royal Meteorological Society*, 111:839-855.

Shuttleworth, W.J., R.J. Gurney, A.Y. Hsu, and J.P. Ormsby, 1989, FIFE: The variation in energy partition at surface flux sites, Remote Sensing and Large-Scale Global Processing, IAHS Publ. No. 186, Proceedings of the IAHS Third International Assembly, Baltimore, Maryland, May 1989.

Sinclair, T.R., L.H. Allen, and E.R. Lemon, 1975, An analysis of errors in the calculation of energy flux densities above vegetation by a Bowen-ratio profile method, *Boundary-Layer Meteorology*, 8:129-139.

Slater, P.N., 1980, Remote Sensing--Optics and Optical Systems, Addison-Wesley Publishing Company, Reading, Massachusetts, 575 p.

Slater, P.N., S.F. Biggar, R.G. Holm, R.D. Jackson, Y. Mao, M.S. Moran, J.M. Palmer, and B. Yuan, 1986, Absolute radiometric calibration of the Thematic Mapper, Proc. of SPIE-Earth Remote Sensing Using the Landsat TM and SPOT Sensor Systems, 660:2-8.

Slatyer, R.O. and I.C. McIlroy, 1961, Practical Microclimatology, 310 p., CSIRO, Melbourne, Australia.

Soer, G.J.R., 1980, Estimation of regional evapotranspiration and soil moisture conditions using remotely-sensed cropy surface temperatures, *Remote Sensing of Environment*, 9:27-45.

Stewart, R.B. and W.R. Rouse, 1977, Substantiation of the Priestley and Taylor parameter alpha = 1.26 for potential evaporation in high latitudes, *Journal of Applied Meteorology*, 16:649-650.

Stewart, J.B., W.J. Shuttleworth, K. Blyth, and C.R. Lloyd, 1989, FIFE: A Comparison between aerodynamic surface temperature and radiometric surface temperature over sparse prairie grass, Proc. 19th Agric. and For. Meteor. and 9th Conf. Biometeor. and Aerobiology, March 7-10 1989, Charleston, South Carolina, Pub. Amer. Meteor. Soc., 144-146.

Taconet, O., R. Bernard, and D. Vidal-Madjar, 1986, Evapotranspiration over an agricultural region using a surface flux/temperature model based on NOAA-AVHRR data, *Journal of Climate and Applied Meteorology*, 25:284-307.

Tanner, C.B. and W.A. Jury, 1976, Estimating evaporation and tranpiration from a row crop during incomplete cover, *Agronomy Journal*, 68:239-243.

Thom, A.S. and H.R. Oliver, 1977, On Penman's equation for estimating regional evaporation, *Quarterly Journal of the Royal Meteorological Society*, 103:345-357.

Thornthwaite, C.W., 1948, An approach toward a rational classification of climate, *Geographic Review*, 38:55-94.

van Bavel, C.H.M., 1961, Lysimetric measurements of evapotranspiration rates in the eastern United States, *Proceedings of the Soil Science Society of America*, 25:138-141.

van de Griend, A.A. and J.H. van Boxel, Water and surface energy balance model with a multilayer canopy representation for remote sensing purposes, *Water Resources Research*, 25(5):949-971.

Verma, S.B. and B.J. Barfield, 1979, Aerial and crop resistances affecting energy transport, in Modification of the Aerial Environment of Crops, B.J. Barfield and J.F. Gerber (Eds.), American Society of Agricultural Engineering, St. Joseph, Michigan, pp. 230-248.